

Physik Department
der Technischen Universität München
Lehrstuhl für Biophysik E22

Mechanical Properties of Complex Cytoskeleton Networks

Rainer Tharmann

Vollständiger Abdruck der von der Fakultät für Physik der Technischen Universität München zur Erlangung des akademischen Grades eines

Doktors der Naturwissenschaften (Dr. rer. nat.)

genehmigten Dissertation.

Vorsitzender: Univ.-Prof. Dr. Manfred Kleber

Prüfer der Dissertation: 1. Univ.-Prof. Dr. Andreas Bausch
2. Univ.-Prof. Dr. Erwin Frey,
Ludwig-Maximilians-Universität München

Die Dissertation wurde am 07.02.2006 bei der Technischen Universität München eingereicht und durch die Fakultät für Physik am 08.03.2006 angenommen.

Für meine Frau Katrin

und meine Kinder

Louisa und Yannick

Contents

SUMMARY

1. INTRODUCTION

I. MATERIALS AND METHODS

2. PROTEINS AND ADDITIVES.....	12
2.1. ACTIN	12
2.2. GELSOLIN	16
2.3. PHALLOIDIN.....	17
2.4. MYOSIN	17
2.4.1. Structure of Myosin II and Myosin II Fragments.....	19
2.4.2. Motor-Activity of Myosin.....	21
2.5. POLYETHYLENE GLYCOL (PEG).....	24
3. THEORETICAL DESCRIPTION OF SEMIFLEXIBLE POLYMER NETWORKS	25
3.1. THEORY OF LINEAR VISCOELASTICITY	25
3.2. GENERAL PROPERTIES IN THE TUBE PICTURE	29
3.3. PLATEAU MODULUS OF HOMOGENEOUS ENTANGLED ACTIN NETWORKS	32
3.3.1. Picture of an Affine Linear Deformation of the Tube	33
3.3.2. The Affine Model of Stretching and Compressing Filaments.....	34
4. EXPERIMENTAL METHODS	36
4.1. EXPERIMENTAL DETERMINATION OF THE VISCOELASTIC PROPERTIES	36
4.1.1. Microrheology.....	36
4.1.2. Macrorheology	43
4.2. EXPERIMENTAL DETERMINATION OF THE NETWORK STRUCTURE	47
4.2.1. Fluorescence Microscopy.....	48
4.2.2. Electron Microscopy	48
4.2.3. Cryo Electron Microscopy	49

II. RESULTS AND DISCUSSION

5. MECHANICAL PROPERTIES OF ACTIN NETWORKS EFFECTIVELY CROSSLINKED BY DEPLETION FORCES	53
5.1. THE ORIGIN OF ATTRACTIVE FORCES CAUSED BY ENTROPY.....	54
5.1.1. Depletion Force in Binary Colloid/Non-ionic Polymer Mixtures	55

5.1.2.	Depletion Force in Mixtures of Actin and Non-ionic Polymeres	56
5.2.	STRUCTURE OF COMPOSITE F-ACTIN/PEG6K NETWORKS.....	57
5.3.	RHEOLOGY OF COMPOSITE F-ACTIN/PEG6K NETWORKS	59
5.3.1.	Linear Response.....	59
5.3.2.	Nonlinear Response	64
5.3.3.	Discussion.....	69
6.	ACTIVE- AND RIGOR-STATE IN ACTIN-MYOSIN NETWORKS	71
7.	RIGOR-HMM/ACTIN NETWORK (RIGOR STATE)	76
7.1.	STRUCTURE OF RIGOR-HMM/ACTIN NETWORKS	76
7.2.	RHEOLOGY OF RIGOR-HMM/ACTIN NETWORKS	80
7.2.1.	Linear Response.....	80
7.2.2.	Nonlinear Response	83
7.2.3.	Discussion.....	84
8.	ACTIVE-HMM/ACTIN NETWORKS (ACTIVE STATE).....	94
8.1.	STRUCTURE OF ACTIVE-HMM/ACTIN NETWORKS.....	94
8.2.	RHEOLOGY OF ACTIVE-HMM/ACTIN NETWORKS.....	95
9.	CONCLUSION.....	103
10.	OUTLOOK.....	106
 III. APPENDIX		
A.	PHYSICAL PRINCIPLES OF THE EXPERIMENTAL-SETUPS	112
B.	RHEOLOGY OF BIOFILMS.....	120
C.	BUFFERS.....	127
D.	BIBLIOGRAPHY	128
E.	ACKNOWLEDGMENTS.....	141
F.	PUBLICATIONS	143
G.	CURRICULUM VITAE	144

Summary

The structure and mechanical response of all eukaryotic cells is essentially determined by cytoskeletal actin networks which are regulated by actin binding proteins (ABPs). The major biological relevance of understanding the mechanisms cells are using to control cytoskeleton is the reason for the huge interest to characterize the mechanical response of these composite network structures. Here, we show a study of the elasticity and microstructure of complex composite filamentous actin networks, using bulk rheology, microrheology, and imaging techniques.

Molecular motors such as myosins are jointly responsible for the force-generating apparatus that moves cells from one place to another or divide cells. In our studies we used HMM (Heavy meromyosin) a subfragment of myosin II that shows full motor activity. Moreover the better solubility of HMM compared to the full construct of myosin II simplifies on the one hand the experimental design and on the other hand the subsequent interpretation of data. Under ATP-rich (Adenosin-tri-Phosphat) conditions the molecular motor HMM is active and able to produce force through a mechanical “power stroke” during which the lever-arm domain of the molecular motor rotates parallel to the filament axis. In the ATP depleted regime the two-headed motor acts as cross-linker (rigor mortis).

A study of *in vitro* active-HMM/actin networks is presented in chapter 8. At high HMM concentrations ($r_{actin/HMM} < 40$) the overall shape of the frequency dependence of the viscoelastic moduli G' and G'' changes and with increasing HMM concentration G' and G'' are also drastically decreasing. Active HMM molecules are able to reduce the plateau modulus G_0 to around 70% of the value found for pure entangled actin. This intriguing effect is discussed with respect to recent theoretical predictions, which take into account that the activity of molecular motors increases the internal temperature. Additionally, another possible explanation is suggested: By means of the Euler buckling instability it is shown that active motors are able to suppress long transverse wave modes of fluctuating filaments when executing the powerstroke. As a result the resistance to thermal bending, which is described by the persistence length L_p , behaves stiffer. Therefore, the effective L_p is increased in active-HMM/actin networks and as a result the elastic response decreases.

When ATP is completely consumed, all motor heads are strongly bound to actin and HMM molecules can act as crosslinks between actin filaments. Thus the network is in rigor state. This sol-gel transition is characterized in chapter 6.

In chapter 7 we study rigor-HMM/actin networks which were found to form an isotropic, homogenous crosslinked network. The linear mechanical response of rigor-HMM/actin networks is described with a model that predicts an entropic origin of the network elasticity. Using this model it is implicitly assumed that an externally applied stress is transmitted in an affine way throughout the whole sample volume. This means that macroscopic elasticity can be ascribed to single filament properties. It is found that the plateau modulus G_0 scales with the crosslinker density as $G_0 \sim r_{actin/HMM}^{-1.2}$ for every actin concentration measured. The onset of the nonlinear response is characterized by the significant network parameter γ_{crit} . Using the measured values for γ_{crit} and assuming a minimal crosslinker distance of the order of the intersection point of the filaments the absolute crosslinker distance L_c as a function of c_{HMM} is calculated for the first time.

Besides these specific interactions, in cells where about 20%-40% of the volume consists of globular proteins depletion forces will be strong enough to severely alter the cytoskeletal structure and mechanics. In chapter 5 it is demonstrated that the addition of polyethylene glycol as a depletion agent results not only in severe structural changes, but also in alterations of mechanical properties of actin solutions. In the plateau of the elastic modulus two regimes can be distinguished by micro and macro-rheological methods. In the first, the elastic modulus increases only slightly with increasing depletion agent, whereas above a critical concentration c^* , a strong increase of $c_{PEG6k}^{3.5}$ is observed in a distinct second regime. Microrheological data and electron microscopy images show a homogenous network of actin filaments in the first regime, while at higher PEG concentrations a network of actin bundles is observed. The concentration dependence of the plateau modulus G_0 , the shift in entanglement time τ_e and the nonlinear response indicate that below c^* the network becomes effectively crosslinked, whereas above c^* $G_0(c_{PEG6k})$ is primarily determined by the network of bundles that exhibits a linearly increasing bundle thickness.

The results presented in this thesis show that on the one hand Peg6K/actin networks form a pure bundle network phase and on the other hand rigor-HMM/actin networks display a homogenous, isotropic crosslinked actin network. Both unambiguous datasets can be consulted to obtain a better understanding for the more complex case of composite bundle and crosslinked networks. Moreover, they can help to get better insight into the strong influence of crosslinker geometry to the network structure and mechanical response.

1. Introduction

“Every cell in your body contains it – every muscle you’re currently using needs it. Without it, life would not exist in the way like it is!”

Actin – a globular protein (G-actin) that is able to polymerize into filamentous biopolymers (F-actin) has several functions in life:

In muscle cells (muscle fibers), that have a very unusual cylindrical structure of around 100 mm length and 10 to 100 μm thickness, thin actin filaments are one of the basic elements (Figure 1-1). In a matchless teamwork actin filaments are sliding along thick myosin II filaments resulting in a decrease in length of the entire muscle. This contractile machinery of muscle tissue is responsible for every movement you are currently executing.

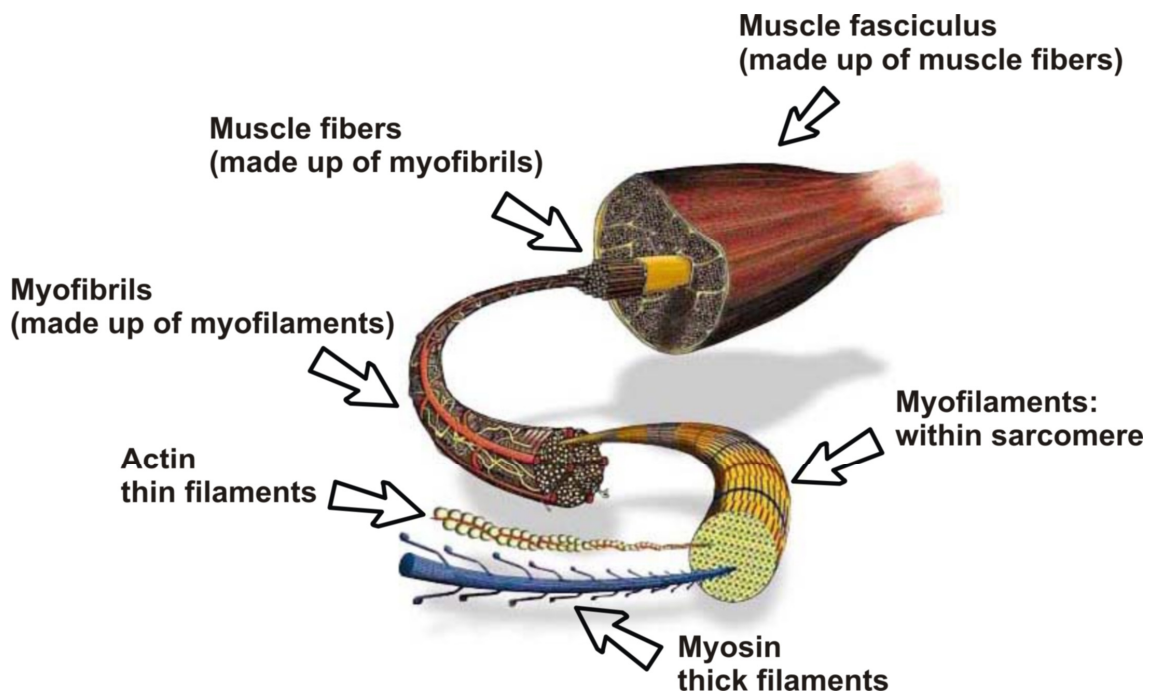


Figure 1-1 Simplified picture of the setup of muscle tissue. Basic elements are the actin and the thick myosin filaments. Together they are responsible for muscle contraction.
(Source: <http://www.artwiredmedia.com/elements/muscle.htm>)

Beside a series of other important proteins involved, myosin II a molecular motor protein and member of the myosin family is the other basic filamentous structure in muscles. By hydrolysis of ATP (Adenosin-tri-Phosphate) myosin II is able to convert chemical energy in mechanical work onto the actin filaments. This causes the sliding of the actin filaments along the thick myosin filaments and together with the sophisticated structure of the sarcomere (an ensemble of several actin- and myosin II filaments), muscle contraction is possible.

In nonmuscle cells, actin appearance is much more complex and dynamically adjusted to the diversified tasks. Here, actin is an integral part of the cytoskeleton and functions as a dynamic scaffold providing structural support that determines the shape of cells and resists forces. Furthermore, actin builds up networks which enable directed movement of materials and organelles within cells and is responsible for the force-generating apparatus that moves cells from one place to another or divides cells.

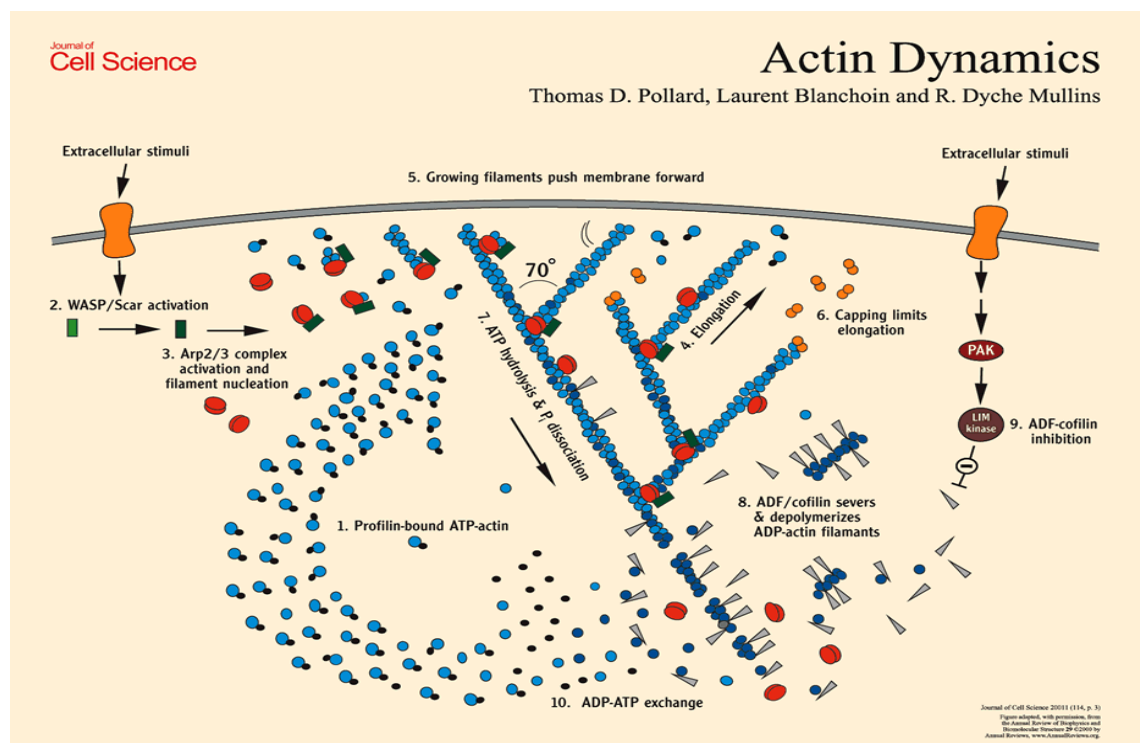


Figure 1-2 The figure shows the dendritic nucleation hypothesis for the assembly of actin filament networks at the leading edge of motile cells (Pollard et al. 2000; Pollard et al. 2003).

When cells are crawling over the surface of a solid substratum a complex and extremely dynamic signal cascade using several proteins is at work. Recently, several pieces of the puzzle “actin dynamics in cells” were assembled and a model to explain cell movement was suggested, depicted in Figure 1-2..

By a controlled growth the actin filaments push the cell membrane forward and spawn at the leading edge lamellipodia which generate focal adhesion points that stick onto the surface. Contractile actin-myosin II bundles in the back of the cell (Figure 1-3, right hand) pull the bulk of the cell forward. The cell breaks its rear contacts with the substratum. During this process actin filaments depolymerize towards the rear end of the lamellipodia.

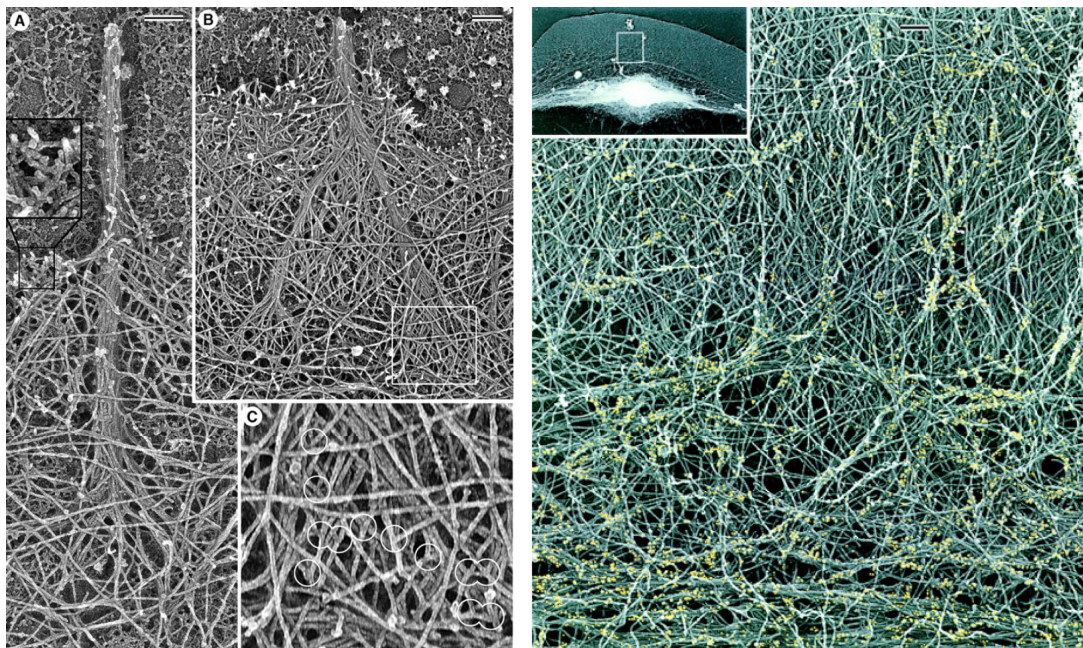


Figure 1-3 left picture shows “ filopodial filaments originate from the surrounding dendritic network. (A) Filopodium contains a tight bundle of actin filaments that splays apart at its root and becomes an integral part of the surrounding network. Filaments in the roots are long compared with the branching network of the adjacent lamellipodium (inset). (B) Recently fused filopodium consists of two sub-bundles, each of which has a splayed root; the boxed region at the root of the right sub-bundle is enlarged in C and shows many branches (encircled) at which filopodial filaments originate.” (Svitkina et al. 2003). right picture shows “ the relative distribution of actin and myosin II filaments in the keratocyte lamellipodia-cell body transition zone. EM of a detergent-extracted cell (overview in inset) after myosin immunogold labeling shows myosin filament clusters and the boundary bundle (bottom) within an actin filament network. Actin filaments forming small bundles and changing their course can be seen at sites of myosin localization. For better visualization, gold particles are digitally colorized in yellow“ (Svitkina et al. 1997). Bars, 0.2 μ m.

Beside this the tip of an elongating axon shows highly stretched out filopodia. These filopodia are filled with actin bundles (Figure 1-3, left hand) and act as a kind of stiffness sensor.

The introduced examples show several structures in which actin and actin networks appear which differ in their mechanical function. Since there is a major biological relevance understanding the mechanism cells are using to control cytoskeleton like composite actin networks, there is a huge interest to characterize the mechanical response of these composite network structures.

Pure *in vitro* polymerized actin already forms a complex system of entangled, semiflexible filaments which behave time dependent viscoelastic. Since mechanical properties of pure actin networks were in focus of research in the last ten years several rheological techniques have been developed (e.g. passive microrheology, active microrheology (magnetic Tweezer or optical tweezers) and macrorheology) and a basic understanding of the linear viscoelastic response of actin networks already exists. Now it is time to go one step ahead and to investigate the nonlinear behavior and the underlying mechanism as well as to study more complex composite actin systems.

The aim of this thesis work was to build up such complex environments of composite actin networks like in cells by simplifying the system using *in vitro* polymerized actin. By the use of several micro- and macrorheological techniques the linear and nonlinear mechanical response of composite actin networks was probed and the structure was determined by a variety of microscopic techniques. The unambiguous experimental results of this present study are explained in context to up coming theoretical models resulting in an additionally basic understanding how cells regulate the dynamic scaffold of actin.

I. Materials and Methods

2. Proteins and Additives

2.1. Actin

Actin is found in all eukaryotic cells examined so far; but does not appear in prokaryotes. Globular actin monomers (G-actin) have a molecular weight of 42 kDa and a dimension of $3 \times 5 \times 6 \text{ nm}^3$ (Holmes et al. 1990) (Figure 2-1 (a)). The monomers assemble to semiflexible polymers called F-actin (filamentous actin) which has a double helical structure with a diameter of 7 nm. The double helices are formed by two single F-actin strands and have a twist repeating every 37 nm. After 74 nm an individual actin strand is again in its initial position (Bullitt et al. 1988) (Figure 2-1 (b)). In vitro polymerization yields a mean filament length of 21 μm , whereas single filaments can reach length up to 100 μm (Figure 2-1 (c)). In cells the filament lengths is controlled by actin binding proteins to some micrometers. In most nonmuscle vertebrate cells, 50% of the actin is present as monomers; the other 50% have the functional filamentous form. Filaments are composed of asymmetric monomers therefore they have a polar appearance. This polarity is responsible for different polymerization properties at both ends and of great importance for muscle contraction, where molecular motors are able to generate directed forces.

The polymerization is a highly dynamic process of assembling and disassembling actin monomers. In vitro G-actin assembles spontaneously under physiological conditions (in cells: 50-100mM KCl, 1mM free Mg^{2+} , pH 7.0-7.1). The initial stage in filament formation is slow depending on the exchange of Ca^{2+} by Mg^{2+} in the free actin monomers. A nucleus of three or more Mg.ATP-actin monomers (Mg^{2+} and ATP bound to the actin monomer) starts polymerization and assembly reaches a maximum rate (growth phase).

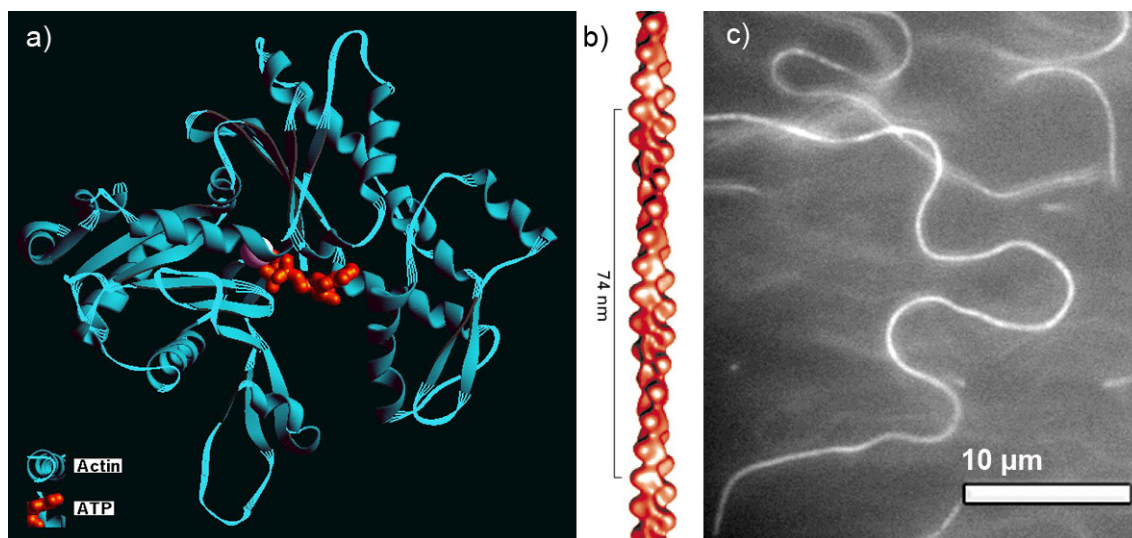


Figure 2-1 a) Structure of an actin monomer containing ATP in the nucleotide binding pocket (Holmes et al. 1990). b) Three dimensional reconstruction from cryo-electron micrographs, showing the filamentous form of actin. After 74 nm a individual actin strand is again in its initial position (Alberts et al. 2002). c) Fluorescence image of high quality actin filaments. The fluorescently marked reporter filaments are embedded in a $9.5 \mu\text{M}$ actin network with a ratio of labeled actin/unlabeled actin = 1:500.

Actin assembly is accompanied by the hydrolysis of ATP (Adenosin-tri-Phosphate). The incorporation of an Mg.ATP-actin monomer within the filament catalyses the hydrolysis of one molecule of ATP in each monomer exchange cycle (Figure 2-2). It is important to mention, that free ATP is also slowly hydrolyzed without catalysation. This stability is a requirement for their biological function: enzymes such as actin and myosin are able to regulate the generation of energy due to ATP hydrolyzation. After Mg.ATP-actin is hydrolyzed to ADP.P_i-actin¹ (Adenosin-di-Phosphat, actin monomer carrying ADP and phosphate P_i) (Pollard et al. 1984) the release of phosphate leads to an unstable state of ADP-actin² (Carrier 1987) (actin monomer carrying ADP). *In vitro* polymerization is not controlled and as long as the concentration of Mg.ATP-actin monomers remains high, subunits will continue to be added at both ends of the filament. During growth the free monomer concentration drops to a minimal concentration where the net addition of monomers continues at the plus end and is reduced at the slow

¹ The probability of hydrolyzation is 1 ATP per second and 50 monomers.

² The dissociation constant of P_i is about $0,006 \text{ sec}^{-1}$.

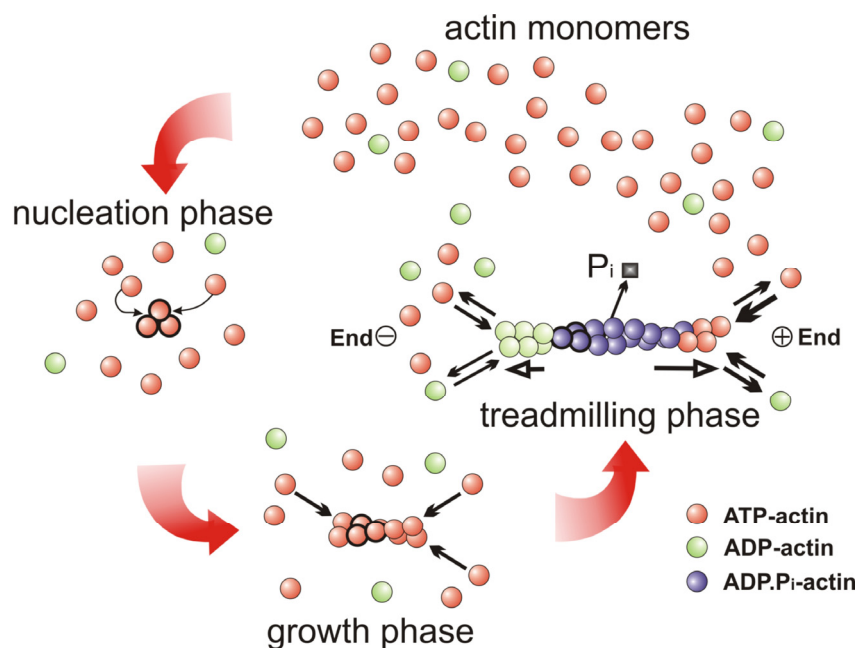


Figure 2-2 Different phases during actin polymerization: The nucleation phase is followed by a phase of fast filament growth. In equilibrium (treadmilling phase) the length of the filaments and the free monomer concentration remain constant.

growing end (minus- or pointed end). As filament elongation continues, the free monomer concentration drops further. At this point, a net disassembly at the minus end dominates till both the length of the filaments and the free monomer concentration remain constant and polymerization is in equilibrium (treadmilling phase (Wegner 1976)). The free monomer concentration in steady state is called the critical concentration and is approximately $c_c=0.1 \mu\text{M}$.

The monomer exchange rate at the plus end is about 20 times higher than at the minus end where a higher probability of hydrolysis leads to an ADP-actin monomer with low binding affinity. The opposite case holds at the plus end. The exchange rates can be modulated by additional proteins like profilin (rapid plus end growth) and thymosin (preventing monomer binding at the plus end).

To visualize the degree of actin polymerization, two measurement techniques are used. The first method is based on the increase in fluorescence when monomers labeled by NBD (4-Chloro-7-nitrobenzo-2-oxa-1,3-diazol) are incorporated into actin filaments (Detmers et al. 1981). Thus the increasing luminous efficiency is a direct measure for the degree of polymerization, as shown in Figure 2-3.

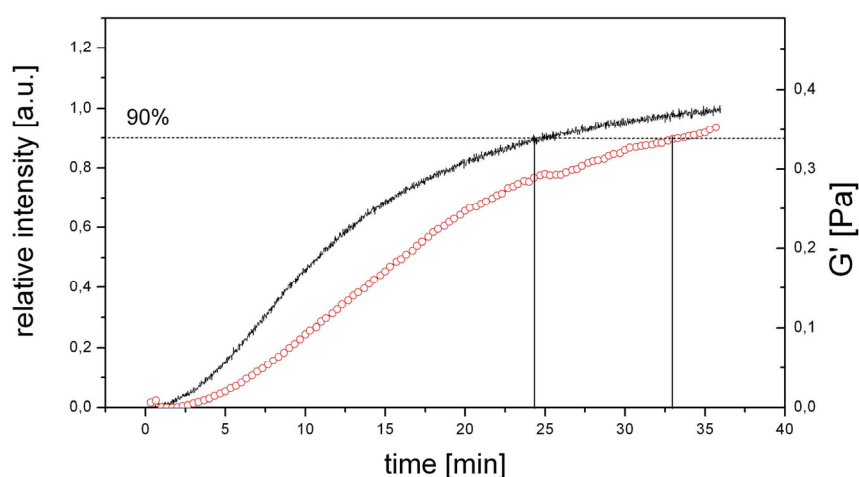


Figure 2-3 The graph depicts two methods to follow the polymerization process. Black curve: Due to the assembly of NBD-labeled actin monomers the fluorescence intensity increases. Red circles: The increase in elasticity upon network formation is followed using bulk rheology.

The second technique makes use of the fact that single polymers are not able to move freely in solutions. F-actin forms isotropic, entangled networks which behave viscoelastic due to sterical hindrance. The increasing elasticity G' during polymerization can be followed by rheological methods as shown in Figure 2-3. Both methods confirm that after 30 minutes more than 90% of all actin is present in filamentous form.

Actin was prepared from rabbit skeletal muscle according to Spudich and Watt (Spudich et al. 1971) and stored in lyophilized form at -21°C . For measurements the lyophilized actin was dissolved in water and dialyzed against fresh G-Buffer (see Appendix C) at 4°C . The G-actin solution was centrifuged at 48.000 rpm and sterile filtrated to minimize the fraction of residual actin binding proteins. The monomeric actin was kept at 4°C for a maximum of 10 days. Polymerization was initiated by adding 1/10 of the sample volume of 10-fold concentrated F-buffer (see Appendix C).

Gelsolin

Gelsolin has a molecular weight of approximately ~90 kDa. It is a Ca^{2+} regulated actin filament severing and capping protein. The protein complex contains six repeat segments each having a molecular mass of about 15 kDa and different functionality (Hartwig et al. 1991; Pope et al. 1991). It has three main effects on actin:

- (a) it severs Ca^{2+} dependent actin filaments³
- (b) it caps the plus end of the actin filament and
- (c) it nucleates actin filament assembly before polymerization (Figure 2-4).

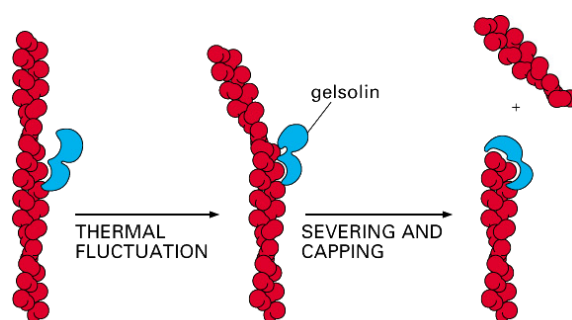


Figure 2-4 Gelsolin has two actin binding sites which allow to bind both along the side and at the end of an actin filament (Alberts et al. 2002).

Gelsolin can be used to adjust the mean length. Due to the capping and nucleating properties of gelsolin the mean length of the filaments $\langle L \rangle$ can be adjusted. The amount of filaments is given by the gelsolin concentration whereas the length is adjusted by the ratio $r_{\text{actin/gelsolin}}$ of actin to gelsolin using following experimental determined formula (Hanson et al. 1963):

$$\langle L \rangle = \frac{1}{370} \cdot r_{\text{actin/gelsolin}} \mu\text{m} \quad (\text{Eq. 2.1})$$

Gelsolin was prepared from bovine plasma serum (Cooper et al. 1987) and stored dissolved in G-buffer at $-80\text{ }^{\circ}\text{C}$. For all measurements in this study the actin filament length was adjusted to $21\text{ }\mu\text{m}$, if else it is explicitly mentioned.

³ The name gelsolin already describes this severing function (Gel–Sol transition).

2.2. Phalloidin

Phalloidin (PHD) was used to mark actin filaments with the fluorochrome Tetramethylrhodamine (TRITC) that is tagged to former. This phalloxin is isolated from the poisonous mushroom *Amanita phalloides* (death cap) and binds to F-actin at a stoichiometry of one to two molecules of actin. It has a molecular weight of 789 Da and as all phalloxins a cyclic peptide structure (molecular formula $C_{35}H_{48}N_8O_{11}S$) (Steinmetz et al. 1998).

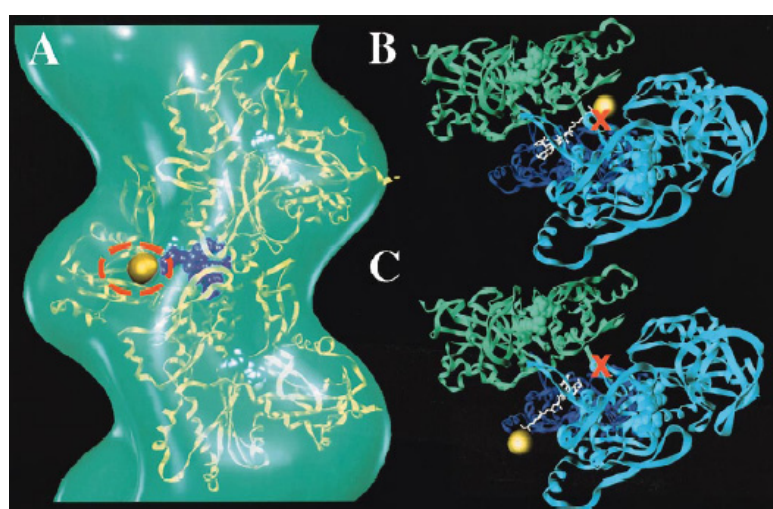


Figure 2-5 Orientation of gold labeled Phalloidin (PHD) within its F-actin binding site. (A) Alignment and overlay of an atomic PHD:F-actin trimer (B) and (C) different oriented views of the atomic Au_{111} -PHD:F-actin trimer complex (Steinmetz et al. 1998).

PHD has no affinity to actin monomers but can bridge two or more actin monomers in the filament configuration (Figure 2-5). Therefore actin filaments are stabilized by phalloidin and can not be severed anymore by gelsolin. Also disassembling of actin monomers during treadmilling phase is stopped.

2.3. Myosin

A fascinating phenomenon in life is the matchless teamwork of actin with molecular motors of the superfamily myosin. These motors are divided into two broad groups, the conventional (type II) myosins, which were first identified in muscle, and unconventional myosins expressed from non muscle cells. Myosins can be further

the opposite direction. Roughly all members of the myosin family contain between one and six calmodulin light chains which stabilize the neck domains (leverarm) that are responsible for the energy conversion due to a conformational change (Figure 6-1). Most of the motors are homodimers which assemble through coiled coil interactions in the elongated rod domain and some are further able to self assemble into higher order structures. Best known are the skeletal myosin II which was used almost exclusively together with the functional sub fragments (explained below) in this study.

2.3.1. Structure of Myosin II and Myosin II Fragments

Myosin II is one of the most studied molecular motor due to the intriguing action in muscle (Figure 1-1), where force is generated by thick bipolar myosin filaments pulling actin filaments towards the center. Myosin II can be easily prepared from muscles in high quantities enabling extensive studies. In absence of ATP the molecular motor binds strongly to an actin filament. This strong binding is called the “rigor state”, coming from the medical term “rigor mortis” where the thick myosin filaments in the muscle are tight bound to actin after death. Myosin II is found in all non muscle cells where it appears to play a crucial role in several processes e.g. transport of vesicles, producing forces in microvilli, maintaining the cell shape or producing stressfibers. Myosin II is also made responsible for the mechanics during cell division.

Myosin II has a molecular weight of 470 kDa and is one of the largest proteins found in cells (Voet et al. 1995). Like all myosins it has three functional domains: a head, neck, and tail (Figure 2-7). The globular head domain is formed by the amino-terminal sequence of the heavy chains. It contains the actin – and the ATP-binding sites and therefore the whole machinery required for motor activity. The moiety of the α -helical twisted heavy chains forms the neck domain containing the binding sites for the essential and the regulatory type light chains (ELC, RLC) which stabilize the neck during the conformational step (Howard 2001) (Figure 2-7). This 8 nm long neck domain is also called molecular lever arm and is responsible for amplifying the smaller motions of the head. To form homodimers the carboxyl-terminal domain of the heavy chains assembles through twisted α -helices to the highly elongated coiled-coil structured tail. Within this dimer structure the two heads of myosin II operate independently. Under physiological conditions the tail region is able to oligomerize

with other myosin II tails to thick bipolar microfilaments resulting in an array of heads which is able to produce high forces in muscles (Huxley 1963).

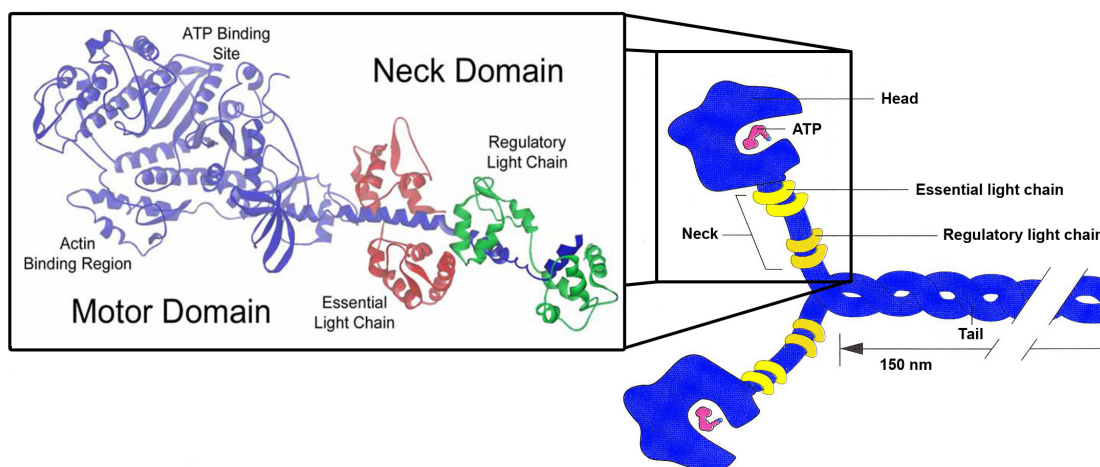


Figure 2-7 Drawing of the molecular motor Myosin II. The enlarged motor domain together with the neck domain has a structural size of 5.5 nm x 20 nm. The size of the coiled-coil tail is around 150 nm (Karp 2005).

Myosin II can be enzymatically cleaved into separable, functional fragments. The treatment with the enzyme Chymotrypsin produces two fragments, heavy meromyosin (HMM) and light meromyosin (LMM) (Figure 2-8). Both can be separated by dialysis to low ionic strength. HMM which is soluble under these conditions, contains enough of the coiled-coil structure for the heavy chains to dimerize and, thus is two headed. HMM conserves its full motor activity. LMM retains the solubility characteristics of the intact myosin and assembles under low ionic strength to filaments of μm length.

Further treatment with the enzyme Papain divides the heavy chains and produces subfragment-1 (S-1) and subfragment-2 (S-2). Both subfragments are soluble. The single headed S-1 has still enzymatic activities and provides full motor activity. S-2 remains in the coiled-coil structure. Intact myosin II can be also cleaved directly at the S-1/S-2 junction, forming S-1 and a filament like rod fragment. Due to the solubility of HMM and S-1, both are used extensively in kinetic and actin binding experiments. Their solubility simplifies on the one hand the experimental design and on the other hand the subsequent interpretation of data.

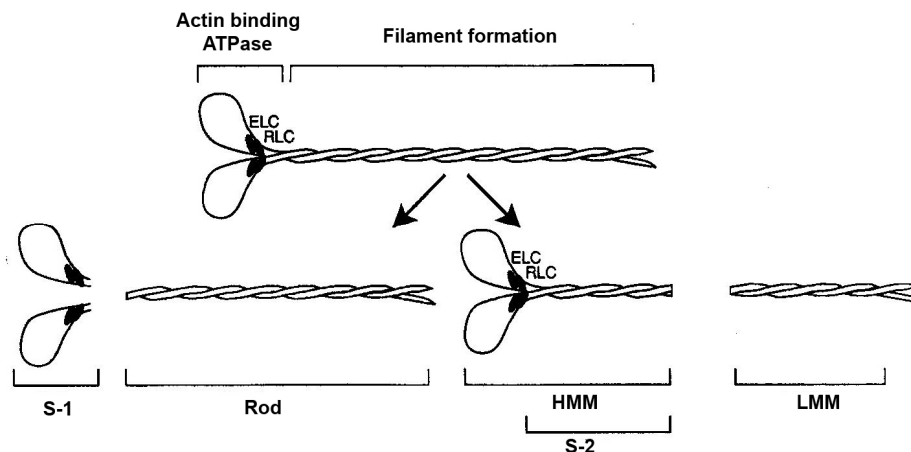


Figure 2-8 By the enzyme chymotrypsin Myosin II can be cleaved into LMM (light meromyosin) and HMM (heavy meromyosin). Further treatment with the enzyme Papain divides the heavy chains and produces subfragment-1 (S-1) and subfragment-2 (S-2) (Sellers 1999).

2.3.2. Motor-Activity of Myosin

ATP appears as universal energy supply in biological systems and drives approximately all molecular motors. As already mentioned, ATP is hydrolyzed slowly without being catalyzed. Myosin II is an enzyme like actin that catalysis the hydrolysis of ATP. This chemical reaction provides the energy that is needed for mechanical action (Stryer 1991).



Since muscle contraction is an interplay between actin and myosin (actomyosin) it is important to understand this scenario on a molecular level. In 1958 H.E. Huxley (Huxley 1958) introduced the rotating crossbridge model within which the structural, biochemical, and mechanical properties of actomyosin coupling becomes understandable. This model is proven to be applicable also to other molecular motors such as dynein (Johnson 1985) and kinesin (Howard 1996; Howard 1997).

The force generation by myosin is driven over a nucleotide dependent conformational change within the crossbridge⁴. It is important to mention both that the release of the phosphate is catalyzed by the binding to the actin filament and the release of myosin

from actin filament is catalyzed by the binding of ATP. The model explains the myosin hydrolysis cycle step by step (Figure 2-9):

- a) The myosin is nucleotide free and tightly bound to actin; AM state (Myosin bound to actin). This state is also called the “rigor state”.
- b) The release of myosin from actin filament is catalyzed by the binding of ATP (AMT) leading to the detached state MT (Myosin with bound ATP).
- c) The bound ATP is hydrolyzed to ADP and Phosphate P_i and the myosin head makes the recovery stroke to its initial position; MDP state (Myosin with bound ADP and P_i).
- d) The rebinding to the actin filament (AMDP state) catalysis the release of the phosphate and exhibit a highly strained state AMD* (transition between (d) and (e)).
- e) The relaxation of this strained state to an unstrained state (AMD) corresponds to the working stroke (powerstroke).
- f) After ADP is released the actomyosin complex is again in the rigor state.

The rate limiting step in this hydrolysis cycle is the transition $MDP \rightarrow AMDP \rightarrow AMD$, that leads to an all over rate of $k_{cat} = 20 \text{ s}^{-1}/\text{head}$. The presence of actin accelerates myosin's ATPase rate 200-fold (without actin $0.1 \text{ s}^{-1}/\text{head}$) (Howard 2001).

⁴ The binding of myosin to actin in muscle looks like a crossbridge.

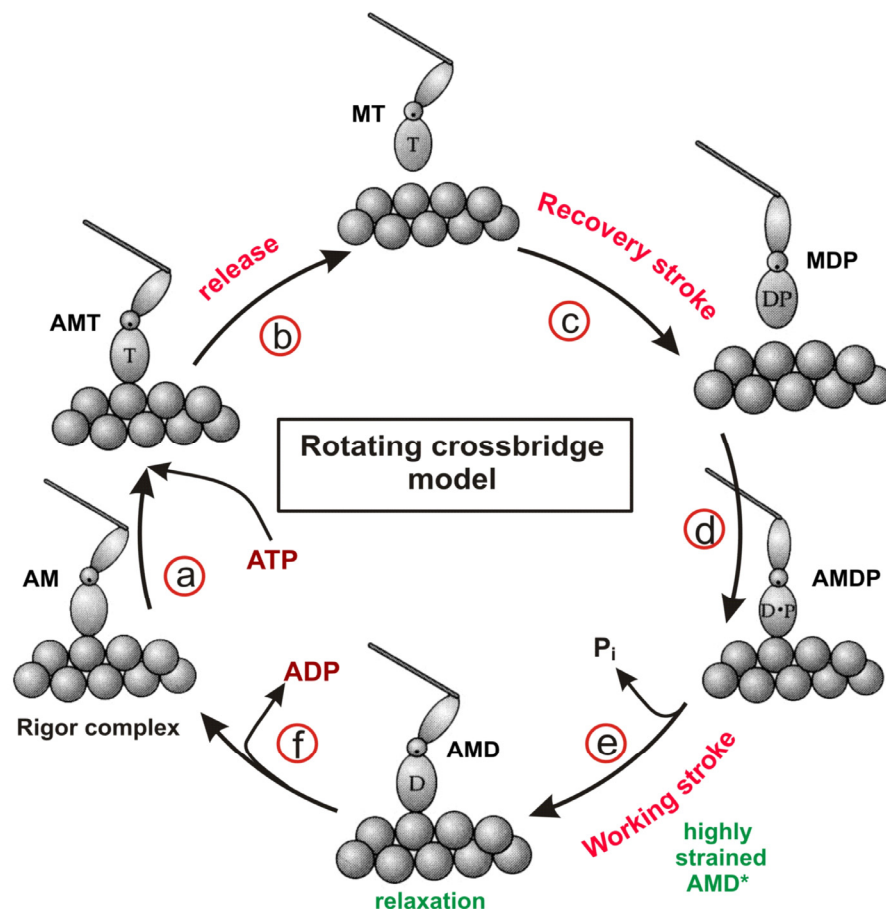


Figure 2-9 Illustration of the Rotating crossbridge model: (a) The myosin is nucleotide free and tightly bound to actin; AM state (Myosin bound to actin). This state is also called the “rigor state”. (b) The release of myosin from actin filament is catalyzed by the binding of ATP (AMT) leading to the detached state MT (Myosin with bound ATP). (c) The bound ATP is hydrolyzed to ADP and Phosphate P_i , and the myosin head makes the recovery stroke to its initial position; MDP state (Myosin with bound ADP and P_i). (d) The rebinding to the actin filament (AMDP state) catalysis the release of the phosphate and exhibit a highly strained state AMD* (transition between (d) and (e)). (e) The relaxation of this strained state to an unstrained state (AMD) corresponds to the working stroke (powerstroke). (f) After ADP is released the actomyosin complex is again in the rigor state.

2.4. Polyethylene Glycol (PEG)

Polyethylene glycol ($\text{H}(\text{OCH}_2\text{CH}_2)_n\text{OH}$) is a stable non-reactive and non-toxic flexible polymer frequently used in food and pharmaceutical products. Therefore it does not harm proteins or cells and is commercially available in a wide range of molecular weights. Molecular weights above 1000 Da have a wax like, white appearance at room temperature. At Molecular weights less than 1000 Da, PEGs are viscous, colorless, liquids. Polyethylene glycol with a molecular weight of 6000 Da (PEG6k) and an approximate radius of gyration of 2 nm (Merck, Germany) was diluted in millipore water (40% w/w) and added prior to the polymerization.

3. Theoretical Description of Semiflexible Polymer Networks

3.1. Theory of Linear Viscoelasticity

Rheology describes the deformation of a body under external forces. Ideal solids behave purely elastic as described by Hook's law. The energy stored in the solid is fully recovered after the force is released. In contrast, an ideal fluid is irreversibly deformed under an external stress and the deformation energy is lost due to friction. This can be understood in terms of Newton's law of viscosity. Real solids and real fluids reveal both viscous and elastic behavior, therefore they are viscoelastic. Whether the viscous or elastic response dominates is a matter of time and applied force.

How the viscoelastic behavior can be accessed experimentally is shown in Figure 3-1, where the material is sheared between two flat rigid surfaces. This picture is of course simplified. It is assumed that the normal force is zero and the material is sheared only in one direction by a small deformation.

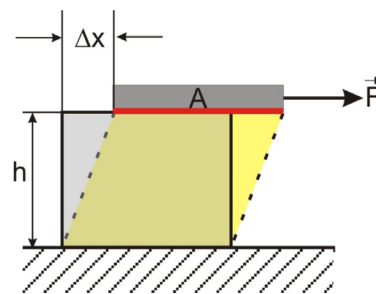


Figure 3-1 Deformation of a solid by a force F (area of contact A , deflection Δx and sample height h).

The shear stress σ in this simple shear is defined as the quotient of the applied force F and the area of contact A ,

$$\sigma = \frac{F}{A}. \quad (\text{Eq.3.1})$$

The shear strain γ is obtained by the ratio of the deflection of the top plate Δx and the thickness of the sample h ,

$$\gamma = \frac{\Delta x}{h}. \quad (\text{Eq.3.2})$$

By this definition the applied strain field is homogeneous, if the material shears uniformly. The theory of linear viscoelasticity is limited to small deformations of the sample where the applied stress is linear to the strain. Generally the ratio of stress and strain (Hook's law)

$$G = \sigma/\gamma, \quad (\text{Eq.3.3})$$

is called "Young modulus". In the case of an elastic solid G is constant.

In ideal fluids σ reacts linearly with the applied shear rate $\dot{\gamma}$, with the constant of proportionality defining the viscosity of the fluid η . This is Newton's law of fluid friction

$$\eta = \frac{\sigma}{\dot{\gamma}}. \quad (\text{Eq.3.4})$$

For viscoelastic materials the reaction to stress and strain can have some time dependence thus the modulus $G(t)$ is also time dependent and defines the material properties at different timescales. Accounting for this time dependence, the stress resulting from any combination of infinitesimal small strains $\delta\gamma$ at timeframes δt can be written as

$$\sigma(t) = \int_{-\infty}^t G(t-t')\dot{\gamma}(t')dt'. \quad (\text{Eq.3.5})$$

In the framework of this PhD-thesis only dynamic measurements were performed; the deformation of the material is periodic in time $\gamma(t) = \gamma_0 \sin \omega t$. Inserting $\gamma(t)$ in Eq.3.3 and Eq.3.4 leads to the following result

$$\sigma(t) = G\gamma(t) = G\gamma_0 \sin(\omega t) \text{ (Hookean solid)}, \quad (\text{Eq.3.6})$$

$$\sigma(t) = \eta\dot{\gamma}(t) = \eta\gamma_0\omega \cos(\omega t) = \eta\gamma_0\omega \sin(\omega t + \delta) \text{ (Newtonian liquid)}. \quad (\text{Eq.3.7})$$

In the case of a purely elastic material stress and strain are perfectly in phase. In contrast in purely viscous liquids the phase δ of the strain is shifted by $\pi/2$. As real solids and real fluids have both viscous and elastic properties stress and strain is out of phase $\sigma(t) = \sigma_0 \sin(\omega t + \delta)$, $0 < \delta < \pi/2$. The combination of Eq.3.6 and Eq.3.7 and the use of the addition theorem results in

$$\begin{aligned} \sigma(t) &= \sigma_0 (\cos \delta \sin \omega t + \sin \delta \cos \omega t) = \gamma_0 (G \sin \omega t + \eta \omega \cos \omega t) \\ &= \gamma_0 [G'(\omega) \sin \omega t + G''(\omega) \cos \omega t]. \end{aligned} \quad (\text{Eq.3.8})$$

Eq.3.8 defines the storage modulus $G'(\omega)$ which is a measure for the elasticity and the loss modulus $G''(\omega)$ that is a measure for energy loss due to friction. By comparison of the left and right side in Eq.3.8 we obtain

$$G'(\omega) = G = \frac{\sigma_0}{\gamma_0} \cos \delta, \quad (\text{Eq.3.9})$$

$$G''(\omega) = \eta \omega = \frac{\sigma_0}{\gamma_0} \sin \delta. \quad (\text{Eq.3.10})$$

A list of various experimental methods to probe the linear viscoelasticity and to obtain the material properties is presented in Table 1 Experimental procedures to determine viscoelastic properties in the regime of linear viscoelastic response. Yellow color indicates transient measurements, while the green ones are dynamically (periodic in time) measurements (Rubinstein et al. 2003).

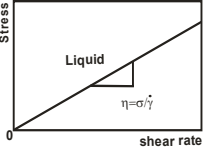
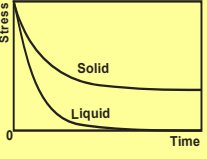
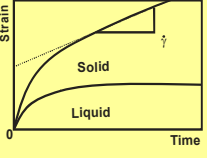
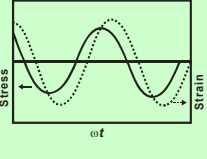
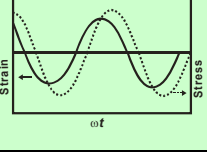
Technique	Apply	Measure	Determine	Graph
Steady shear	Constant shear rate $\dot{\gamma}$	Steady stress σ	Viscosity $\eta = \sigma/\dot{\gamma}$	
Step strain	Constant strain γ	Stress $\sigma(t)$	Relaxation modulus $G(t) = \sigma(t)/\gamma$	
Step stress	Constant stress σ	Strain $\gamma(t)$	Compliance $J(t) = \gamma(t)/\sigma$	
Oscillatory strain	$\gamma(t) = \gamma_0 \sin \omega t$	$\sigma(t) = \sigma_0 \sin(\omega t + \delta)$	$G'(\omega) = (\sigma_0/\gamma_0) \cos \delta$ $G''(\omega) = (\sigma_0/\gamma_0) \sin \delta$	
Oscillatory stress	$\sigma(t) = \sigma_0 \sin \omega t$	$\gamma(t) = \gamma_0 \sin(\omega t + \delta)$	$G'(\omega) = (\sigma_0/\gamma_0) \cos \delta$ $G''(\omega) = (\sigma_0/\gamma_0) \sin \delta$	

Table 1 Experimental procedures to determine viscoelastic properties in the regime of linear viscoelastic response. Yellow color indicates transient measurements, while the green ones are dynamically (periodic in time) measurements (Rubinstein et al. 2003).

3.2. General Properties in the Tube Picture

Polymers can be divided into flexible, semiflexible and rigid filaments, according to the characteristic length scale, their persistence length L_p (Figure 3-1).


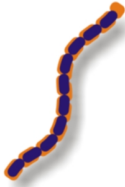

polymer class	<i>flexible</i>	<i>semi flexible</i>	<i>rigid rods</i>
persistence length L_p contour length L	$L_p \ll L$	$L_p \cong L$	$L_p \gg L$
example			

Figure 3-2 Polymers can be divided into three different classes depending on their bending stiffness.

From a physical point of view, polymerized actin is a prototype of a semiflexible polymer. F-actin forms *in vitro* random (orthogonal) networks with a well-defined mesh size ζ (the average shortest distance between filaments).

Three length scales characterize the static structure and elasticity of the network: The filament contour length L , the mesh size of the network ζ and the persistence length L_p of the filaments. L_p is defined as the decay length that characterizes the correlation between the orientations of the tangents \vec{t} to the filament at two positions s and s' of the filament. $|s - s'|$ is the distance between the two positions along the contour of the filament (Figure 3-3). The persistence length is related to the filament bending modulus κ_0 according to

$$\kappa_0 = k_B T \cdot L_p. \quad (\text{Eq.3.11})$$

Here k_B is the Boltzmann factor and T the temperature. The most important property of the actin cortex for its role as a dynamic machine that controls cell shape changes is its viscoelasticity in the slow time regime ($10^{-2} - 10^4$ s). The frequency dependent viscoelastic impedance $G^*(f) = G'(f) + iG''(f)$ has been extensively studied by torsional macrorheometry (Hinner et al. 1998) and magnetic tweezers (Keller et al. 2001) or

colloidal probes (Crocker et al. 2000) microrheometry. Typical schematic frequency spectra of $G'(f)$ and $G''(f)$ of a semiflexible polymer network are shown in Figure 3-4.

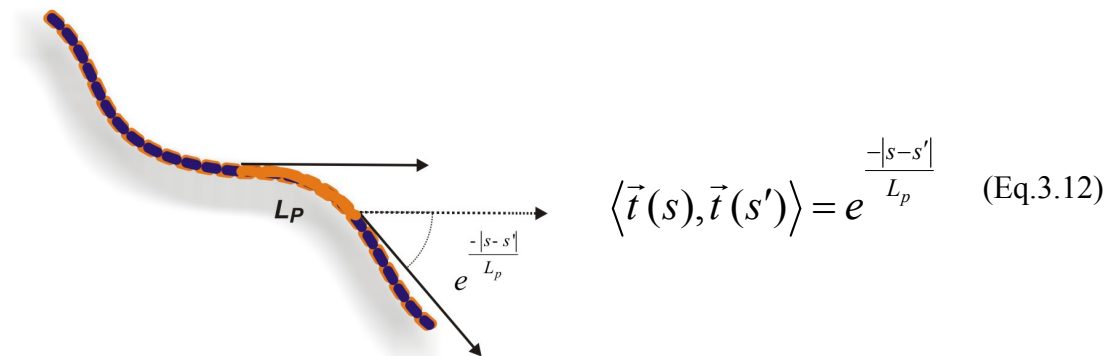


Figure 3-3 The persistence length is defined as the characteristic distance along the polymer chain over which the orientation of the tangents \vec{t} decays with Eq.3.12..

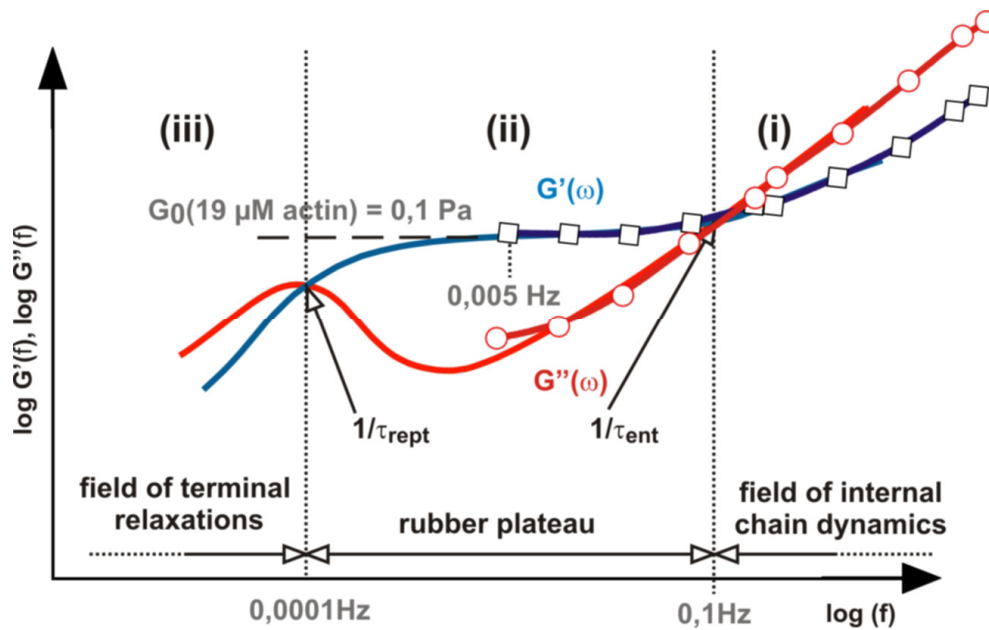


Figure 3-4 Typical frequency dependence of the viscous and elastic properties of semiflexible polymer networks. The solid line shows the theoretical frequency dependence of G' (blue line) and G'' (red line), the open squares (G') and circles (G'') refer to a real measurement by torsional macrorheometry of a $19 \mu\text{M}$ actin network. Three distinct regimes can be distinguished in the frequency dependent viscoelasticity. G_0 , τ_{ent} and τ_{rept} are explained in the text.

Three frequency regimes can be distinguished, which can be attributed to well-defined molecular processes with characteristic time and length scales:

- (i) a fast regime $f > \tau_{ent}^{-1}$ (τ_{ent} is the entanglement time defined below) which is determined by the entropic tension of the filaments (stresses can only relax by intra molecular processes)
- (ii) a plateau regime at $\tau_{rept}^{-1} < f < \tau_{ent}^{-1}$ (τ_{rept} is called reptation time) associated with the affine deformation of the network and
- (iii) the terminal regime at $f < \tau_{rept}^{-1}$ where the network starts to flow by self-diffusion of the filaments.

The crossover time's τ_{ent} and τ_{rept} have well defined meanings:

τ_{rept} is the reptation time (also called disengagement time) which is equal to the time a filament requires to diffuse over a distance equal to its contour length L (Morse 1998).

It is related to the self-diffusion coefficient D_{rept} of the filaments

$$\tau_{rept} = \frac{L^2}{\pi^2 D_{rept}} \propto L^3. \quad (\text{Eq.3.13})$$

τ_{ent} is the entanglement time (also called relaxation time) of the longest wavelength bending mode of a single filament which is not truncated by the constraints imposed by the other chains of the networks (or the wall of the tube). The entanglement time is given by (Isambert et al. 1996)

$$\tau_{ent} \approx \frac{\zeta_{\perp} L_e^4}{\kappa_0} \approx \frac{1}{k_B T} \cdot L_p^{1/3} \cdot d^{8/3} \approx L_p^{-1/5} \cdot c_{actin}^{-8/5}, \quad (\text{Eq.3.14})$$

where ζ_{\perp} is the friction coefficient of the filament within the tube, L_e is the entanglement length (see text below) and d is the tube diameter.

In the framework of the Edwards-De-Gennes tube model (Genies 1979) (Figure 3-5), the constraint by the surrounding polymers is accounted by the width of the tube, which is of the order of the mesh size.

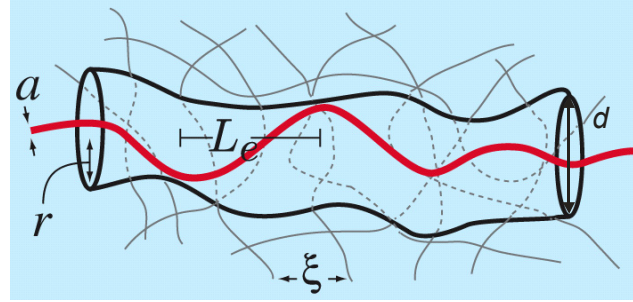


Figure 3-5 Reptation model by De Gennes (Gennes 1979). The filament is fluctuating in a tube that is built up by the constraints of the other filaments. Characteristic length scales are: mesh size ξ , filament diameter a , maximal fluctuation amplitude r , tube diameter d and entanglement length L_e .

The validity of the tube model was directly observed by fluorescence microscopy (Käs 1994). The typical distance between two collision points of a polymer with the surrounding chains (or the wall of the tube) is called the entanglement length L_e (also called deflection length) (Odijk 1993)

$$L_e \approx d^{2/3} \cdot L_p^{1/3}. \quad (\text{Eq.3.15})$$

3.3. Plateau Modulus of Homogeneous Entangled Actin Networks

From the experimental measurements, one can very easily obtain the plateau modulus G_0 (Figure 3-4). The plateau modulus is a measure for the elasticity of the network and depends strongly on how stress is propagated through the network.

There are two possibilities how macroscopic uniform stress is transmitted all the way through actin networks:

- In an affine deformation of the network the strain is uniform throughout the sample. As a consequence the mechanical response can be scaled down to the elastic properties of a single filament. E.g. for foam-like structures it has been already shown (Gibson et al. 1999) that it is appropriate to scale macroscopic elasticity down to a single cell.
- In a nonaffine deformation the deformation field that results from a uniformly applied stress is spatially highly heterogeneous over long length scales.

All models used to theoretically describe a network of semiflexible chains starting from the picture of a single filament. For a single actin filament the wormlike chain model

(Saitô et al. 1967) is applicable. The dynamic properties and viscoelasticity of actin networks are determined by the thermally excited bending fluctuations of the single actin filaments. The Hamiltonian describing the energy cost of an actin filament with bending modulus κ_0 can be written as

$$H = \frac{1}{2} \kappa_0 \int ds (\nabla^2 \bar{u}(s))^2. \quad (\text{Eq.3.16})$$

3.3.1. Picture of an Affine Linear Deformation of the Tube

In the framework of the tube model, the strain field is transmitted in an affine way through the network. Filaments are hindered by neighboring filaments and feel the strain as an increased constriction in the tube. Due to the applied strain transverse fluctuations will be suppressed which has to be taken into account in the free energy balance. Since each collision of a polymer with its tube reduces the conformation space there is a free energy cost of the order of $k_b T$ for each collision. Therefore the total free energy F of $\nu=c/L$ polymers per unit volume (c =concentration, L =contour length) weighted by the density of collision points is equal to $F \approx \nu k_b T L / L_e$ (Frey 2001). Combining Eq.3.15 with latter findings results in following expression of the free energy and hence the plateau modulus

$$G_0^{entangled} \approx F \approx \frac{k_B T}{\xi^2 L_e} \approx k_B T \cdot L_P^{-1/5} \xi^{14/5} \approx k_B T \cdot L_P^{-1/5} c_{actin}^{7/5}. \quad (\text{Eq.3.17})$$

This power law has been verified experimentally for entangled actin solution (Hinner et al. 1998). The polymer density defines the mesh size $\xi \equiv \sqrt{3/\nu L}$. Experimentally it was verified to scale as (Schmidt et al. 1989)

$$\xi \propto 0.34 \cdot \frac{1}{\sqrt{c_{actin}}}, \quad (\text{Eq.3.18})$$

which results in a mesh $\xi \approx 0.5 \mu\text{m}$ for $c_{actin} = 0.4 \text{ mg/mL}$ ($9.5 \mu\text{M}$).

3.3.2. The Affine Model of Stretching and Compressing Filaments

In another model the affine deformation of the network is described by longitudinal stresses that are transmitted over entanglements with the other actin filaments (Mackintosh et al. 1995). Due to the affine deformation the elastic properties of the network are scaled down to the properties of a single filament. To obtain the plateau modulus G_0 theoretically, an ensemble of chain segments of length L_e is considered. The elastic response of the network results from the tension in such chain segments as a function of the extension. The mechanism for elasticity is still entropic in origin and results from the thermal excited transverse undulations. Figure 3-6 shows a schematic picture that helps to understand the nature of the elastic properties of a chain segment ((Shin et al. 2004) supporting information).

- a) For zero temperature no thermal excited fluctuations are observable and therefore the end-to-end distance L of the chain segment equals the contour length.
- b) A rise in temperature results in thermal undulations of the filaments. Thermal fluctuations of amplitude h reduce the end-to-end distance by Δ' . Taking this into account in Eq.3.16 results in a bending energy $U_B \sim \kappa_0 L (h/L^2)^2$.
- c) Applying longitudinal stresses due to an affine deformation, results in an extensional force F onto the filament and the chain segment is stretched by δ with the stretching energy $U_F \sim FL\varepsilon \sim Fh^2/L$. Both bending and stretching of the filament is counted by the net strain $\varepsilon = (\Delta' - \delta)/L_e$.

Since the elastic energy has to be balanced by the thermal energy the imposed strain $\gamma \sim \delta/L_e$ and the stress $\sigma \sim F/\xi^2$ on a single filament can be calculated by the principle of equipartition of energy from $U_B + U_F \sim k_B T$ ((Shin et al. 2004) supporting information).

This leads to the following expression of the plateau modulus G_0 :

$$G_0^{entangled} \sim a \frac{\kappa_0^2}{k_B T} \xi^{-2} L_e^{-3} \approx \kappa_0 L_P^{2/5} c_{actin}^{11/5} \quad (\text{Eq.3.19})$$

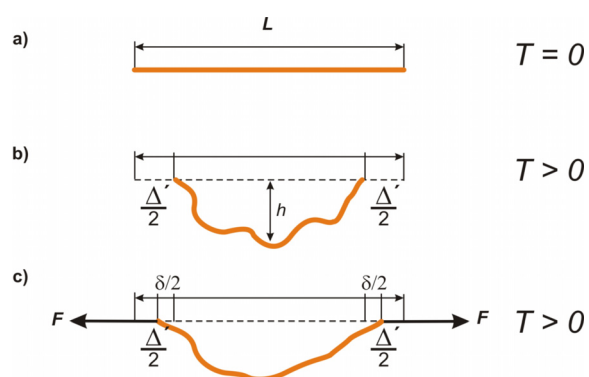


Figure 3-6 Schematic drawing of the effect of an external force to the elastic properties of a chain segment at finite temperature (drawing after (Shin et al. 2004) supporting information).

The exact theoretical calculations predict a high prefactor of $a=90$, which does not correspond to the experimentally measured values of G_0 for entangled actin. In addition, it is not obvious that longitudinal stresses can be transmitted over sliding entanglements.

Taking into account the huge time regime (10^{-4} - 10^2 Hz), the huge regime of the viscoelastic response of actin (0.01Pa – 10^3 Pa) and the accuracy of the experimental determination of the moduli it is not obvious to decide which scaling behavior describes the system the best. Moreover the differences in scaling both theories predict are rather small. Beside this the tube picture is widely accepted and seems to describe the elastic behavior of pure, entangled actin solutions best.

4. Experimental Methods

4.1. Experimental Determination of the Viscoelastic Properties

4.1.1. Microrheology

Since actin is difficult to obtain in large amounts and quantitative measurements on micrometer scale are of interest, methods with very small sample volume and micron probes are required. The experimental measurements described in the following were performed by using a) a micro-rheometer which is based on the principle of magnetic tweezers (Keller et al. 2001), and b) passive particle tracking, a micro-rheological technique which is based on the analysis of the Brownian motion of embedded micron beads (Gardel et al. 2003; Wong et al. 2004). For both methods a microscope and an image-processing unit are needed to visualize the micron sized probes.

Microscope

In the micro-rheology experiments presented in this thesis work colloidal particles are visualized on an inverted microscope Axiovert 10 (Zeiss, Oberkochen, Germany). The sample is imaged by a 32x Achromat long distance objective and an additional 2.5-fold magnification (Zeiss, Oberkochen, Germany). The microscope is mounted on a vibration-absorbing table (Technical Manufacturing Corporation, Peabody, MA, USA).

Image-processing unit

The sample is recorded by means of a peltier-cooled digital CCD-camera with a frame size 656x494 pixels (C4880, Hamamatsu, Herrsching, Germany). The frame rate is limited by the CCD chip read-out time. Therefore the image frequency can be varied only by choosing a suitable image size. In order to reduce the read-out time of the CCD chip by a factor of 2, binning as for example two fold binning can be used, where 2 x 2 pixel are combined to one. But on the other hand two fold binning lowers also the image resolution by a factor of 2. Thus, depending on the frame size and binning the frame rate can be adjusted in a range between $<1 \text{ s}^{-1}$ and 166 s^{-1} . As a read-out tool Jörg

Schilling developed in his diploma thesis in 1999 the image processing software “Open Box”(Schilling 1999).

With this software it is possible to control in real time

- reading and writing of the analog-digital/digital-analog card DT3010-32 (Data Translation, Marlboro, Ma, USA).
- image capturing of the CCD-camera by reading out the IC-PCI frame grabber card equipped with an AM-DIG-2M modul (Imaging Technology Incorporated, Bedford, MA, USA).
- data storage on a hard disk by a Fast Trak 66 Raid controller (Promise Technologies, San Jose, Ca, USA) with a writing speed of 16 MB/sec.
- following the motion of the beads with a bead tracking algorithm.

By the use of a tracking algorithm (developed by D.Simson, F. Ziemann und J.Schilling, Physics Department E22) based on a 2-dim. Gaussian fit of the intensity distribution it is possible to determine displacements of the bead with a resolution as small as 5nm.

4.1.1.1.Magnetic Tweezer

Magnetic Tweezer Setup

Figure 4-1 shows a schematic view of the magnetic tweezer Setup. Monodisperse super paramagnetic colloidal probes (Dynabeads M-450, Dynal Biotech ASA, Hamburg) with a radius of 2.5 μm are embedded in the actin network that is polymerized in the sample cuvette. The property “super paramagnetic” denotes that 0.19 weight % of Ferro oxide (Fe_2O_3) particles, which are smaller than the Weiss domain, are embedded in the latex beads. Due to the small size the remanence and hysteresis effects known from ferromagnetic materials are reduced to a minimum. In order to cancel any interaction between the magnetic beads a mean distance of about 10 bead diameters was adjusted via the bead concentration. The sample cuvette (Figure 4-2 (c)) made from teflon with a glued cover slide has a volume of 25 μl . In order to prevent evaporation and degradation on air-water surfaces the volume is airproof closed by a second cover slide and vacuum grease. Using a small wheel the cuvette, which is placed in a plastic ring, can be rotated

via a rubber ring in order to find the middle section in the sample chamber where the magnetic forces from the left side is equal to the right (Figure 4-2 (a) and (b)). The magnetic force is generated by an inhomogeneous magnetic field applied by two coils (42 mm length, 30 mm diameter, 1100 windings of a 0,63 mm copper wire) with an iron core (6 mm diameter). The amplifier (made by electronics workshop, Physics department) which generates a proportional output signal of maximum 60 V and 4.5 A is fed by a computer-integrated control voltage.

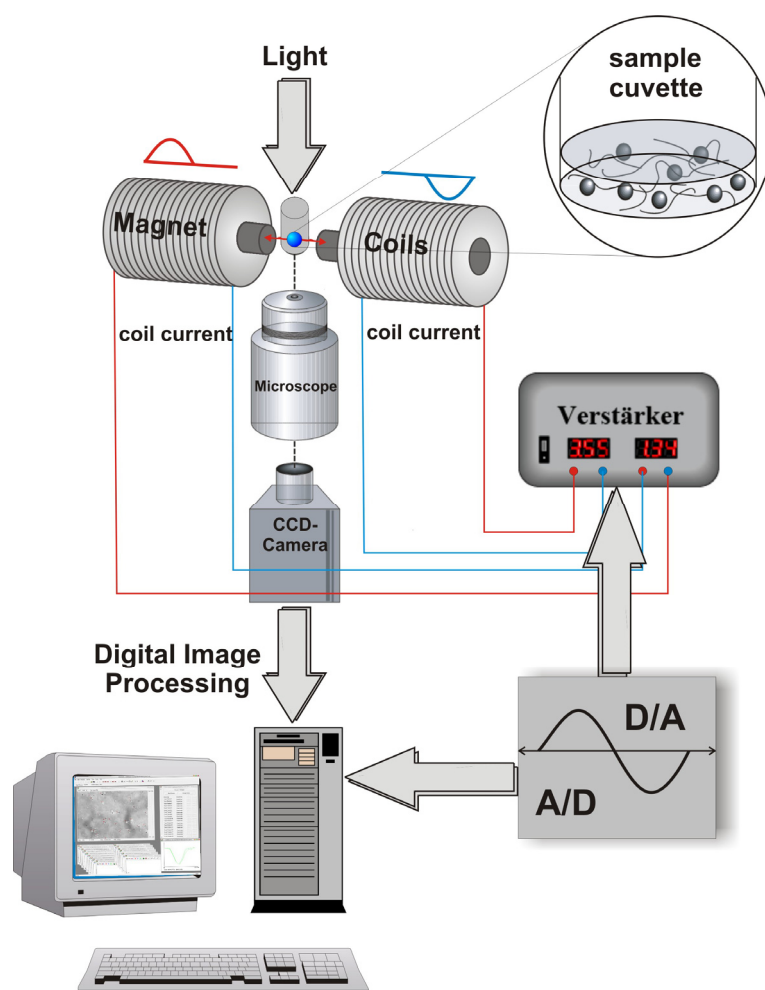


Figure 4-1 Schematic sketch of the magnetic tweezer setup with the control unit. The cylindrical shaped cuvette has a sample volume of 25 μl . The sample with embedded magnetic beads is enclosed between two glass cover slides. It is mounted on an inverted microscope together with a pair of coils. In order to generate an extremely inhomogeneous magnetic field an iron core is fitted into the coils. The triggering of the coils is done by an amplifier that is controlled by a computer using a digital/analog card. In order to follow the movement of the beads, this was filmed using a peltier-cooled CCD-camera.

In order to exert an oscillating force to the magnetic beads two magnetic fields exhibiting opposite field gradients are generated alternately in the two opposing coils. Therefore, the two coils are supplied with sinusoidal half waves. The amplifier produces these two output current signals. The output signal fed to one coil is proportional to the positive control signal while the signal fed to the second coil is proportional to the absolute value of the negative control signal.

The magnetic tweezer is mounted on an inverted microscope which is equipped with a CCD camera. The magnetic tweezer and the image processing is controlled by “Open Box” as described above.

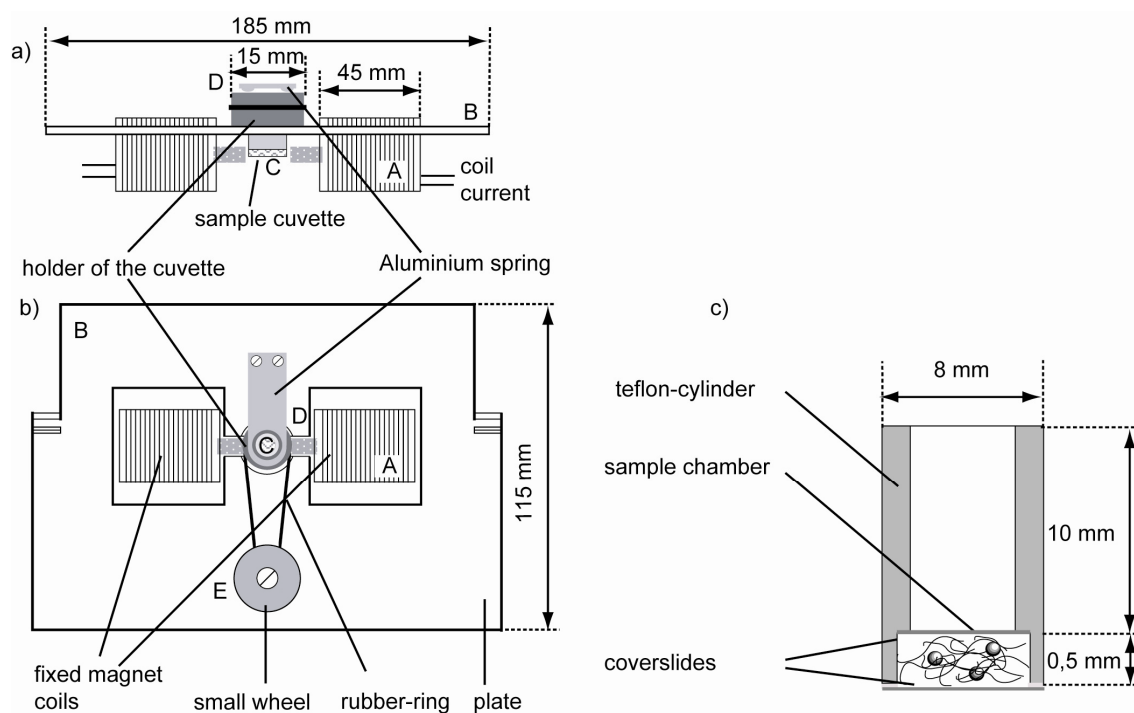


Figure 4-2 Central Magnetic Tweezer unit mounted on the microscope. a) The front view a) and the top view b) show the coils (A) with the iron core fixed on an aluminum plate (B) which can be inserted on the microscope. The cuvette (C) is placed in a plastic ring that can be rotated by a small wheel (E) and a rubber ring to find the middle section in the sample chamber where the magnetic force is balanced. The sample cuvette is enlarged in c) (drawn after (Keller et al. 2001)).

However, if one knows the applied force and measures the amplitude and the phase shift of the oscillations, it is possible to calculate the viscoelastic moduli G' and G'' (for detailed description of the physical principles see Appendix A).

$$\begin{aligned}G'(\omega) &= \frac{F_0}{6\pi R x_0(\omega)} \cos(\delta(\omega)), \\G''(\omega) &= \frac{F_0}{6\pi R x_0(\omega)} \sin(\delta(\omega)).\end{aligned}\tag{Eq.4.20}$$

During my thesis work I introduced two major improvements on the original magnetic tweezer setup. These improvements were necessary, because the existing setup suffered from two problems. First of all, the force of the original setup was too low to measure densely crosslinked networks and therefore the displacement of the beads was not detectable. As a solution to this problem both coils were replaced by other coils with more windings and bigger iron cores. With the new coils it is possible to reach higher forces (up to maximum 10 pN compared to around 3 pN in the old setup). The other problem the original setup suffered from was that the position of the sample cuvette stayed always at a fixed distance to the iron cores of the magnetic coils (Figure 4-3, left picture). Thus the amount of measurable beads in a sample was limited to the middle of the sample chamber where the magnetic force is balanced. As long as the sample is homogeneous this does not lead to a systematic effect, but if the sample is heterogeneous, e.g. in crosslinked and bundled networks, the measure of one or two beads leads to a high deviation between different sample measurements. In order to solve this problem the setup was modified in the following way. The coils are in a fixed position with respect to the objective while the sample cuvette is still able to move (Figure 4-3, right picture). This leads to a nearly constant force in the field of view with a relative deviation (error) below 19% (Wagner 2003). By moving the cuvette all beads in the sample chamber can be used for measurements. Under these conditions now a statistical analysis of the assay is possible, which presents both heterogeneity of the networks and comparability with macroscopic measurement.

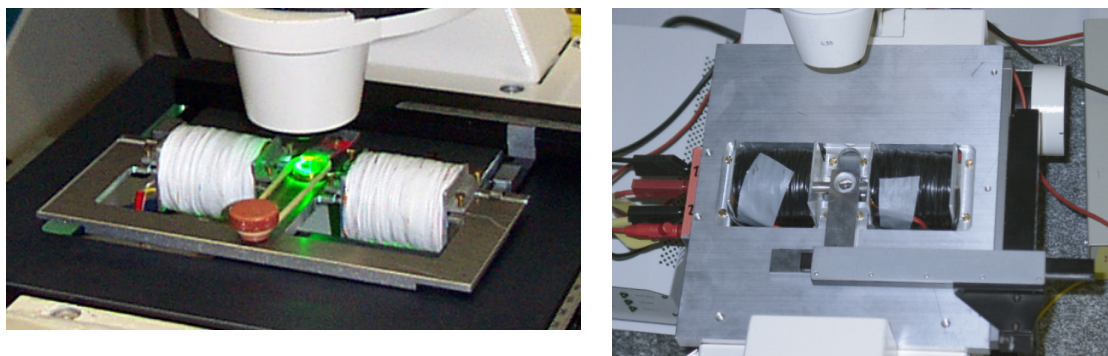


Figure 4-3 The picture on the left shows the old magnetic tweezer setup. In this setup the sample chamber is always in a fixed position with respect to the magnetic coils. The picture on the right shows the modified setup where the coils are fixed on the microscope plate. With this setup it is possible to use all particles contained in the whole sample volume for measurements.

4.1.1.2. Passive Microrheology – One Particle Microrheology

A further extensively used method to probe the mechanical response of soft materials on a micrometer scale is the passive rheology (F. Gittes 1997; Crocker et al. 2000; Levine et al. 2000; Gardel et al. 2003; Wong et al. 2004). Unlike active methods such as for example the magnetic tweezer in passive microrheology the linear strain fluctuations of the network are probed by observing the thermal motion of micron-sized colloidal spheres embedded in the sample. For this technique no external force needs to be applied and a possible destruction of the material is minimized. As a further advantage a small sample volume which is comparable to the ones of the magnetic tweezer can be used. The passive microrheology gives insight into both the linear rheological properties over an extremely wide frequency range (10^{-3} Hz - 10^5 Hz) and the local microstructure. Depending on the stiffness of the material – and thus on the displacement of the probed particle centers (that is coupled to the particular detection scheme) – the elastic modulus that can be measured is limited to some hundred Pascal (Gardel 2004). Several different particle tracking techniques have been developed in the past view years, e.g. optical tweezers, light scattering, and video microscopy, which vary mainly in the temporal and spatial resolution. There is also a significant physical difference if one tracks a single particle or multiple particles. One-particle rheology crucially depends on the microenvironment of the individual probe particles (Gardel et al. 2003). If the surface chemistry of the bead modifies the structure of the material around the bead, the one-particle response will be a reflection of the structure and mechanics of the

microenvironment rather than bulk rheology. If the probe size is larger than the length scale which characterizes the heterogeneity, then one-particle microrheology determines the bulk response. Unlike one-particle microrheology measuring the crosscorrelated motion of tracer particle pairs eliminates the response of local heterogeneities or effects of bead surface chemistry and therefore measures bulk rheology even if one particle rheology does not. However, recently it has been shown (Gardel et al. 2003) that although one particle microrheology yields different values for G' and G'' in the short time range it converges at long timescales (G_0 , the elastic response of the network) with two particle and bulk rheological measurements and thus measures the right plateau modulus G_0 . The elastic modulus can be obtained from the MSD using:

$$G_0 = \frac{k_B T}{\pi \langle \Delta \vec{x}^2(\tau \rightarrow \infty) \rangle a} \quad (\text{Eq.4.21})$$

The fact that the mean square displacement of a single particle is coupled to the local environment can be also an advantage. The width of the displacement distribution function gives rise to information on the heterogeneity of the examined network.

Experimental

The local elasticity of the network was probed by tracking embedded carboxylate-modified latex (CML) spheres (Interfacial Dynamics Corp., Portland OR., USA) with a 32x magnifying objective on a Axiovert 10 microscope (Zeiss, Oberkochen, Germany). It has been shown that the surface of the CML particles has a negligible effect on the determination of the local elastic plateau modulus G_0 of actin networks (Valentine et al. 2004). The sample was embedded into the sample chamber that can be closed from the bottom with a cover slide and vacuum grease and then be hermetic sealed from the top in the same way. The sample holder fits directly in the objective table of the microscope.

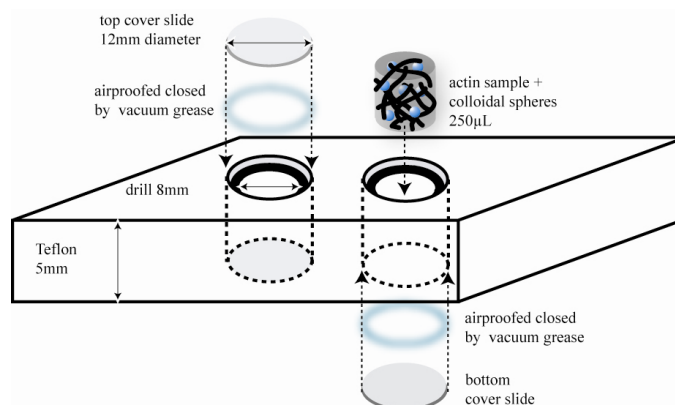


Figure 4-4 The sample is embedded into the sample chamber that can be closed from the bottom with a cover slide and vacuum grease and then be hermetic sealed from the top in the same way.

4.1.2. Macrorheology

Since actin is in vitro only available in small volume fractions, the material is extremely soft. During rheological measurements of such soft material using a macroscopic method minimal shear forces have to be applied. O. Müller developed a torsional stress controlled rheometer in 1988 which is able to measure extremely soft actin networks (<0.4 mg/ml) with very small deformations and concurrently small sample volumes (Mueller et al. 1991).

The length scale on which stress is applied by bulk rheology is much larger than the length scale of generally appearing heterogeneities. Therefore macroscopic measurements determine the volume averaged properties of the sample and are not affected by small local heterogeneities. This is the main advantage when measuring the viscoelastic properties of different appearing actin networks (bundled networks, micro gel domains within the network) where additional actin binding proteins were added.

4.1.2.1. Rotating Disc Rheometer

Macrorheometer Setup

The original idea of this macrorheometer setup which is shown in Figure 4-5 is based on a work from H. Gaub (Gaub et al. 1986) who studied phase transitions of lipid monolayers.

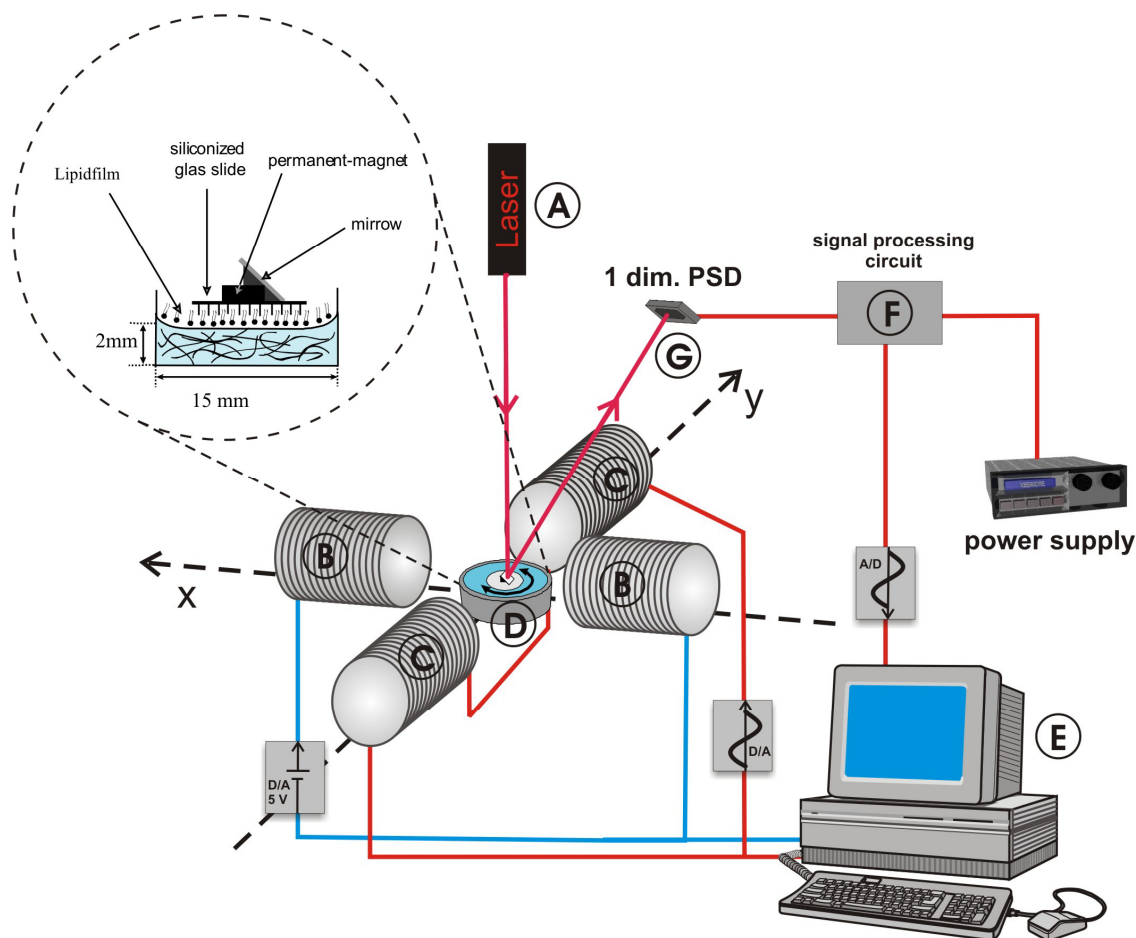


Figure 4-5 Schematic sketch of the rheometer setup (Müller88). Magnification of the cuvette (D): Onto the sample ($400\mu\text{l}$) a phospholipidic monolayer (DMPC) is placed to prevent denaturation of actin at the air-water interface. On top of the lipid film a glass plate ($R_1=4\text{mm}$, $d=0.1\text{mm}$) is located and centered by the meniscus of the fluid. In order to apply shear forces to the sample a small splitter of a permanent magnet is glued on to the glass disc. In order to reflect the laser beam (A) a small mirror is fixed on the magnet. The sample cuvette (D) (interior radius $R_2=7.5\text{mm}$) is positioned between two pairs of coils. The retain coils (B) are fixing the plate to zero whereas the deflection coils (C) are exerting the magnetic force on the permanent-magnet. The reflected laser beam is focused on a 1-dim PSD (G) that is operated by signal processing circuit unit (F). Both the control of the coils and the recording of the measured signal is done by reading out an AD/DA-card with a computer, respectively.

A round glass cuvette (inner radius $R_2=7.5\text{mm}$) contained $400\mu\text{l}$ of the sample to be analyzed. It was covered by a phospholipidic monolayer (DMPC, dimyristylphosphatidylcholine) in order to prevent denaturation of actin at the air-water interface. A rotating disc ($R_1=4\text{mm}$, $d=0.1\text{mm}$) was placed onto the sample and centered by the meniscus. By covering the cuvette with a glass slide any evaporation effects were eliminated. The deflection of the disc can be achieved by means of coils and of permanent magnets and is measured with a laser beam reflected from the rotating disc,

which is focused on a position sensitive detector (PSD). A computer controls the setup with an AD/DA-card (for detailed descriptions of the physical principles see Appendix A).

In order to measure the viscoelastic behavior of biological material with higher accuracy on one hand and, on the other hand, in order to be more flexible in the experimental procedures, several changes of the data processing unit were necessary. Therefore a new control and analyzing program “Rotating Disc 1.1” was written under LabView 6i (National Instruments Corporation, Austin, TX). Additionally a new computer with a higher performance and equipped with a (AD/DA) data acquisition card (DAQ) PCI-MIO-16XE-10 (National Instruments) was used. The AD/DA card provides a 16-bit resolution as well as 16 single ended analog input channels and 2 analog output channels (output range ± 10 V) with a sample rate of 100 kSample/sec each. The voltage of the retain coils is adjusted to 5V with one output channel; the second output channel applies the dynamic torque of the deflection coils. Additionally, a new one-dimensional position sensitive detector (PSD) S1352 (Hamamatsu Photonics, Herrsching, Germany) replaced the old defect PSD. The S1352 has a stripe-like active area of 2.5×34 mm² with a lateral position resolution of ± 2.1 μ m. This corresponds to the minimum detectable light spot displacement, which is fairly accurate enough to follow the reflected laser beam. All components needed to operate, i.e. to control and drive, the 1-dimensional PSD are mounted on a single compact PC board C3683-01 (Hamamatsu Photonics, Herrsching, Germany). This signal processing circuit includes a head-amplifier, signal addition/substraction electronics, and analog divider circuits and provides the position signal and the intensity signal of the reflected beam spotting on the PSD. Both signals are read in the computer by the use of two analog input channels of the DAQ card. The analysis of the measured signal is optimized by an applied Fast-Fourier transformation (FFT) that exhibit the applied torque, the amplitude of the angular deflection, and the phase shift of the oscillations. The measured viscoelastic properties G' and G'' are plotted by means of the program “Rotating Disc 1.1”. Thus, due to a modern computer system and an optimized software improved studies were possible.

4.1.2.2. Commercial Rheometer – Physica MCR 301

For the last three years industry has been improving the commercial acquirable techniques and at present very user friendly and high precision rheometer are available that are able to apply a minimal torque down to $0.1 \mu\text{Nm}$ and a maximum torque up to 200 mNm . Such a rheometer enables very comfortable measurements with a sophisticated control software. Due to the fully developed control mechanism these rheometers allow in principle the access to all parameters which are of importance in rheology. The rheometer Physica MCR 301 (Anton Paar, Graz, Austria) provides all these features and was used in the framework of this PhD for measurements of the bulk viscoelastic properties (Figure 4-6). Moreover, by means of that rheometer it is possible to obtain the nonlinear response of highly stressed composite actin networks. Such a regime is unreachable for the self-built rotating disc rheometer because of the small forces that can only be exerted onto the disc. Thus measurements of both bulk rheometers are complementary to each other.

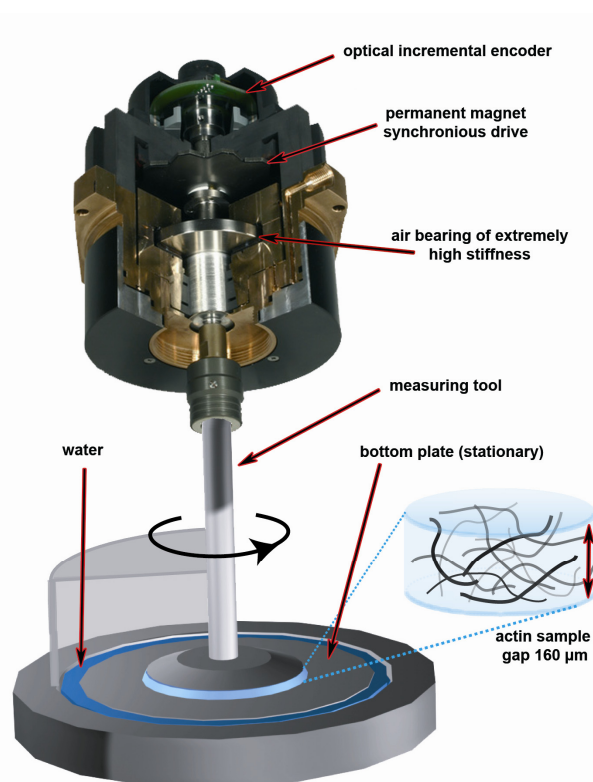


Figure 4-6 Measurement unit of the rheometer Physica MCR301.

Measurements of rheological values are in general based on the exact knowledge of the relationship between the shearing stress and the deformation of the substance. One of the two values is predetermined and the other one is measured by a measuring means, which is achieved by means of the MCR 301 by a highly dynamic synchronous EC-drive (electrically commutated) that is air bearing and equipped with a high resolution, optical incremental encoder (resolution $< 1\mu\text{rad}$). By deflection of the air bearings the normal force is capacitively measured.

The measurement system is easily exchangeable. Its geometry can be saved on a chip that is implemented in the coupling end and is read out by the MCR301 automatically. For the measurements with actin networks it was clarified by several experiments that the plate/plate (radius 25 mm) geometry is generally comparable to the measurements of the self build setup. Before loading the sample both the measuring system and the base plate are cleaned with Millipore water and pure ethanol. After the sample volume (517 μl) is placed on the base plate the measuring head is moved downwards to a preset gap position (160 μm). In order to prevent evaporation effects the whole measure cell is covered by a chamber while having water in the rim (Figure 4-6) ensures the air around the sample to be saturated by water. After one hour of polymerization measurements are started by the software “Rheoplus V2.62” (Anton Paar, Graz, Austria) that is installed on a computer (Intel Celeron 2.4 GHz, 512 MB Ram). The rheometer connected to the computer by a serial (RS232) connection.

4.2. Experimental Determination of the Network Structure

For the interpretation of rheological data it is of importance to observe the 3-dim. microscopic structure of the examined networks. It yields the correlation of the determined viscoelastic behavior to the length scales in the system. Unfortunately, it is still difficult to obtain information of the 3-dim. structure even with highly developed imaging systems, e.g., a confocal microscope or cryogenic electron tomography. Thus in addition 2-dim. methods are important in order to relate the microscopic structure to the macroscopic response.

4.2.1. Fluorescence Microscopy

In fluorescent microscopy actin filaments were marked with special fluorochromes that enable visualizing of the filaments on a light microscope (Axiovert 200, Zeiss, Oberkochen, Germany). The fluorochromes absorb light of a certain exciting wavelength for nanoseconds and emit it afterwards shifted to a longer wavelength. In the framework of this PhD work actin was marked with the fluorochrome Tetramethylrhodamine (TRITC) that is conjugated to phalloidine. It is known that phallotoxin, extracted from the fungus *Amanita phalloides* (death cap), binds to and stabilizes actin filaments (Alberts et al. 2002). TRITC can be excited by absorbing light of a wavelength of 540-545 nm while emitting light of a wavelength in the range of 570-573 nm. For the excitation by intensive light at the mentioned short wavelength a high pressure mercury short-arc lamp HBO 103 W/2 (Osram) with a monochromatic optical spectrum controlled by an Atto Arc 2 System (Zeiss) was used. In order to excite by and observe light at the specific wavelengths a filter set was used (Filter set #20, Zeiss Oberkochen, Germany).

4.2.2. Electron Microscopy

Another very common method to visualize the structure of actin networks is the method of negative stain electron microscopy (Figure 4-7).

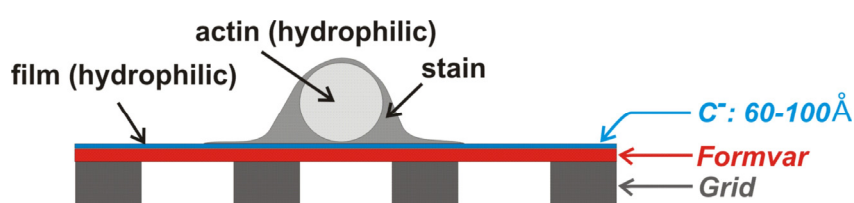


Figure 4-7 Schematic representation of the effect of the support film (hydrophilic) and the specimen surface (hydrophilic) on the meniscus of the stain before drying.

The procedure of negative stain electron microscopy consisted of the following steps: Carbon-coated formvar films fixed onto a copper grid were discharged in a glow discharge. Afterwards actin samples were adsorbed onto the formvar films for 60 seconds and washed in a drop of distilled water for other 60 seconds in order to reduce

the filament concentration and the amount of salt crystals. To make the filaments visible the samples were negatively stained with 0.8% uranyl acetate for other 60 seconds. After the negative staining another washing step was applied (60s) in order to remove excess stain. Subsequently the excess liquid was drained with filter paper to the edge of the grid and the sample was then permitted to air-dry. Due to the staining and dehydrating steps a variety of artifacts can be introduced to the networks. The main problem is the shrinkage that makes it difficult to analyze quantitatively important length scales such as the mesh size ξ and the cross link distance l_c of the networks. The measurement of the absolute filament thickness is also not possible due to the broadening by the absorbed stain. But in spite of the limitations of this method it is important to get any possible information about the structure of actin networks - even if it is just a rough idea of the homogeneity or the relative scaling behavior.

4.2.3. Cryo Electron Microscopy

A novel and very promising imaging technique is observing 3-dim. images of actin networks by electron tomography (ET). ET allows the visualization of the 3-dim. structure of unfixed and unstained biomaterial down to a resolution of ~ 5 nm. First experiments with biological material embedded in amorphous ice were done in the 1970^{ies} by Taylor and Glaeser (Taylor et al. 1974) and improved in the 1980^{ies} by Dubochet, Adrian and Lepault (Dubochet et al. 1982; Dubochet et al. 1988). In order to prevent sample destruction by ice crystal formation the actin networks have to be shock frozen in liquid ethan (87K) which leads in a direct phase transition (~ 150 K) to vitrified (glasslike) ice.

Also for this technique the actin sample was adsorbed (60 sec.) to glow-discharged carbon-coated perforated formvar films on copper grids which were washed in a drop of distilled water (60sec.). Further on colloidal gold particles were added to the actin-containing droplet and the sample was directly blotted and quickly frozen in liquid ethan (Figure 4-8). The gold particles are needed for the reconstruction, when the shifts in the different tilted projections are calculated.

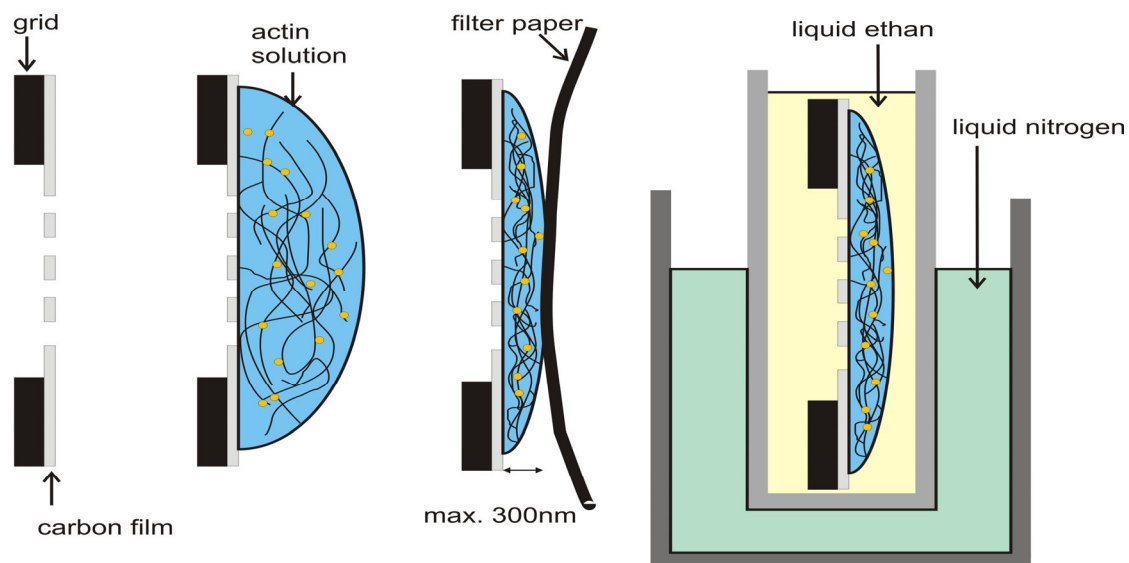


Figure 4-8 Schematic sketch of the cryo-fixation. The sample is adsorbed (60sec.) to glow-discharged carbon-coated perforated formvar films on copper grids. The grid with the sample is washed in a drop of distilled water (60sec.). Afterwards colloidal gold particles are added to the solution droplet that is directly blotted and quickly frozen in a bath of liquid ethan.

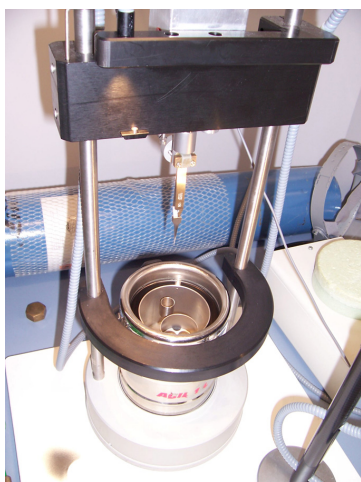


Figure 4-9 Left-hand side: photograph of the shooting apparatus for the cryo-fixation. Right-hand side: transfer of the sample from the storage box to the sample holder (Image provided by Anna Sartori, Max-Planck-Institute for Biochemistry, Dept. of Molecular Structural Biology)

For vitrification the liquid ethan is cooled by liquid nitrogen (77 K). Ethan features a high thermal conductivity in contrast to liquid nitrogen that evaporates by even a very small rise of the temperature and covers the sample with a gas “cushion”. In order to control the procedure of vitrification an injection apparatus was developed that works principally like a guillotine (Figure 4-9, left-hand side picture) (Dubochet et al. 1988). After the preparation the of the cryogenic sample it has to be kept continuously at liquid nitrogen temperature until it is transferred to the high vacuum of the microscope by means of a special cryo-sample holder (Figure 4-9, right-hand side picture). During this transfer it is precarious to get contaminations of ice crystals in the sample. Finally the holder can be kept at temperatures of 90 to 100 K for several hours which allows long measurements.

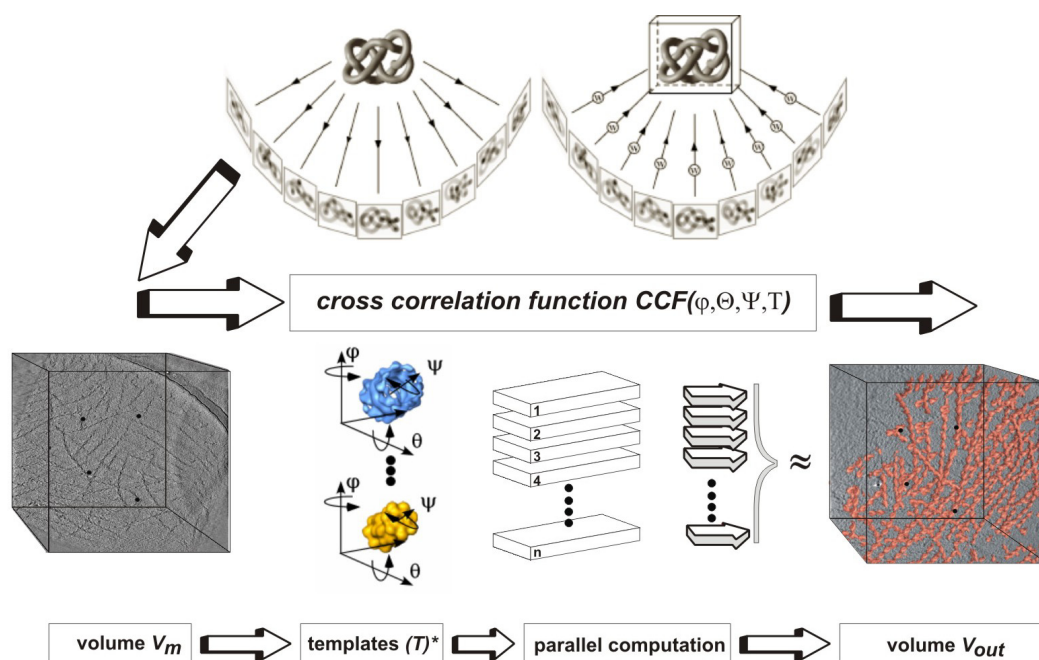


Figure 4-10 Cryo electron-microscopy: in a first step the object is imaged as 2 dim. projections under different tilting angles. Then the sample volume is reconstructed by a weighted back projection. In order to visualize specific molecules the method of template matching can be used but which needs a high computational power (after: (Plitzko 2005)).

From the cryogenic sample a series of tomograms of 2 dimensional projections of the sample under various tilting angle series is recorded perpendicular to the incident electron beam (Figure 4-10). The tilting angle ranges from -70° to $+70^\circ$. Unfortunately

it is not possible to reach the full range of $\pm 90^\circ$ because of the block out of the electron rays due to the sample holder. After the recording procedure a three-dimensional picture of the sample volume is reconstructed using a weighted back projection. In order to identify individual macromolecules the method of template matching is used. For this technique a detailed image of the specific molecule of interest, a “template”, is obtained by maybe another microscopic technique. The template can be used to search for the desired molecule in the entire volume of the tomogram making use of by cross-correlations (Plitzko 2005). Although after blotting the network still has a thickness of about 300 nm the network is affected by shrinking. In order to get rid of such artifacts the sample preparation can be improved by the method of cryo-sectioning. Here one polymerizes actin in a tube which is shock frozen. After that an approximately 250 nm thick slide of vitrified actin is cut and transferred onto the grid while keeping the temperature at liquid nitrogen conditions. The detailed procedure is still not sophisticated and further measurements are necessary to control all important parameters during sample preparation.

II. Results and Discussion

5. Mechanical Properties of Actin Networks Effectively Crosslinked by Depletion Forces

For the understanding of the cell functioning in “ideal” chemo-physical conditions it is the best to start with experiments which are well-defined and preferably at a steady state. However, usually cells are far away from such ideal specifications. Furthermore, for example a fascinating feature of non-ideality arises from macromolecular crowding: It is well known that proteins are packed down in 20-40 vol.-% of the cell volume (Ellis 2001). Around 10 % of these proteins exist in filamentous and 90% in globular form (Figure 5-1).

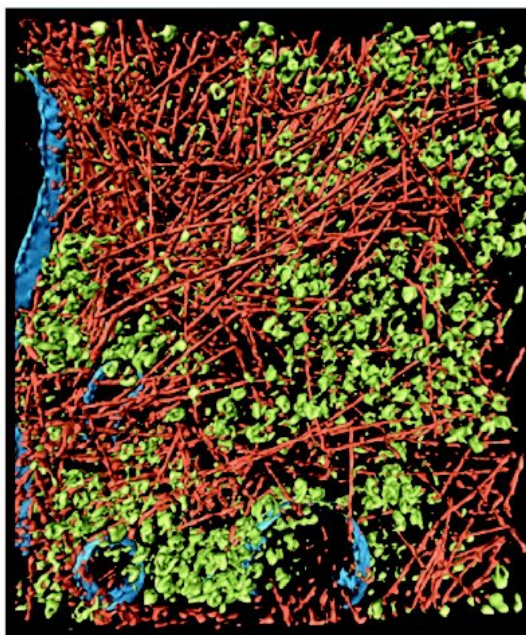


Figure 5-1 Picture on the left: Visualization of actin network, membranes, and cytoplasmic macromolecular complexes (actin filaments (reddish); other macromolecular complexes, mostly ribosomes (green); and membranes (blue))(Medalia et al. 2002).

In such crowded volumes chemo-physical processes like the diffusion of molecules in cytoplasm, solution equilibrium, reaction rates and the structure are affected.

The structure and rheology of cytoskeletal networks are regulated by actin binding proteins. Besides these specific interactions depletion forces which are generated by the gain of excluded volume can also alter the properties of cytoskeletal networks (Madden et al. 1993; Madden et al. 1994; Kulp et al. 1995).

In the following it is demonstrated that the addition of PEG as a depletion agent not only results in severe structural changes but also in alterations of mechanical properties of the actin solutions. In rheological measurements two regimes can be distinguished when plotting the plateau modulus over the PEG concentration. In the first regime the elastic modulus increases only slightly with increasing depletion agent, whereas above a critical concentration c^* a strong increase of $c_{PEG6k}^{3.5}$ is observed in a distinct second regime. Microrheological data and electron microscopy images show a homogenous network of actin filaments in the first regime, while at higher PEG concentrations a network of actin bundles is observed. The concentration dependence of the plateau modulus G_0 , the shift in entanglement time τ_e , and the nonlinear response indicate that for PEG6k concentrations below c^* the network becomes effectively crosslinked, whereas above c^* $G_0(c_{PEG6k})$ is primarily determined by the network of bundles that exhibits a linearly increasing bundle thickness.

5.1. The Origin of Attractive Forces Caused by Entropy

Considering a system of hard spheres without any attractive interaction between them, in general it is not obvious that there is crystallization. Crystallization is usually connected with yielding a higher ordered system and resulting in lower entropy of the system. However, a higher ordered system, e.g. crystals, results not in every case in a loose of entropy. In order to understand this feature it is important that – besides the configurationally entropy of the centre of mass of the spheres (it is for the random closed packed (hcp) apparently higher than for the hexagonal closed packed (hcp); Figure 5-2) – the entropy of the free volume (motional space between the spheres) is also taken into account. As a result the summation of both entropies shows that for a packing density of 54.5% the hcp configuration is preferred due to the higher free volume entropy (Bechinger et al. 1999).

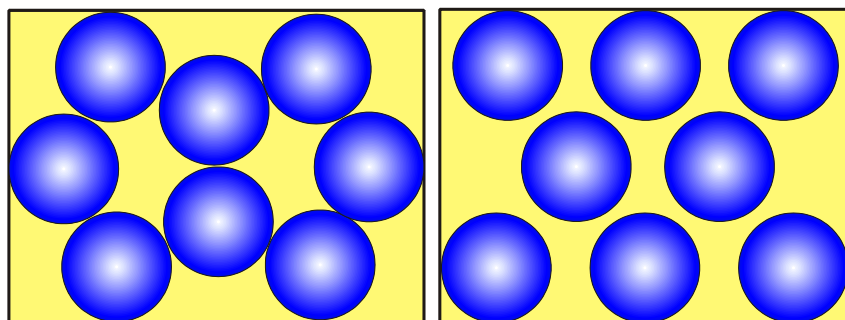


Figure 5-2 The entropy of the free volume in the left arrangement of the spheres is higher than the one in the hcp arrangement on the right. But due to the gain of the configurationally entropy of the centre of mass in the hcp this arrangement is preferred.

5.1.1. Depletion Force in Binary Colloid/Non-ionic Polymer Mixtures

In binary colloidal suspensions and colloid/non-ionic polymer mixtures depletion force results in an interaction between the large spheres themselves.

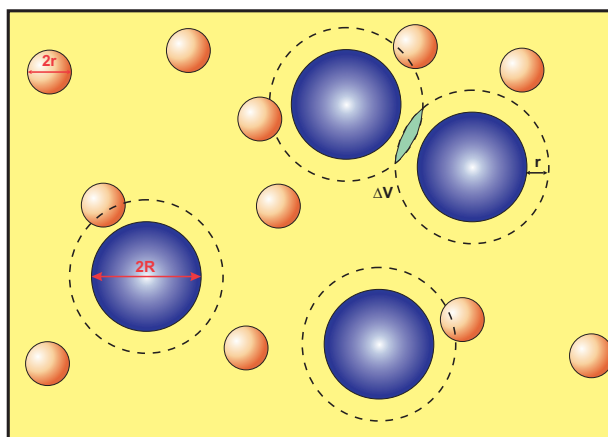


Figure 5-3 Schematic drawing of a binary colloidal suspensions. The smaller spheres are not able to enter with their centre of mass the volume (excluded volume) around the larger spheres visualized by the dashed lines. An overlap of the excluded volume results in increased entropy of the smaller spheres and reduces the free energy of the system. Therefore an attractive interaction occurs.

When two larger particles approach to within a distance z smaller than the diameter of the smaller colloidal particles $2r$, the overall configurationally entropy is increased by excluding the latter from this region (Figure 5-3). Consequently, the depletion of the smaller particles results in an effective osmotic pressure and leads to an effective

attraction between the larger colloidal species (Asakura et al. 1954; Madden et al. 1993). A theoretical description of such entropic interactions was done by Asakura and Oosawa (Asakura et al. 1954). In the ideal gas limit

$$\Delta F(z) = -T\Delta S = k_B T N \ln\left(\frac{V + \Delta V(z)}{V}\right) \approx -k_B T N \Delta V(z), \quad (\text{Eq. 5.1})$$

where N is the number of small colloidal particle and $\Delta V(z)$ is the overlap volume. The lowering of the free energy F of the small spheres is the reason for the attractive force between the larger spheres and it is nearly proportional to the overlapping volume.

5.1.2. Depletion Force in Mixtures of Actin and Non-ionic Polymeres

Because of the large persistence length, L_p , actin can be approximated as stiff rods on length scales much smaller than L_p . In this case the Asakura-Oosawa model (Asakura et al. 1954) can be easily expanded on stiff rods/sphere systems just by calculating the overlap volume of two cylinders (Figure 5-4).

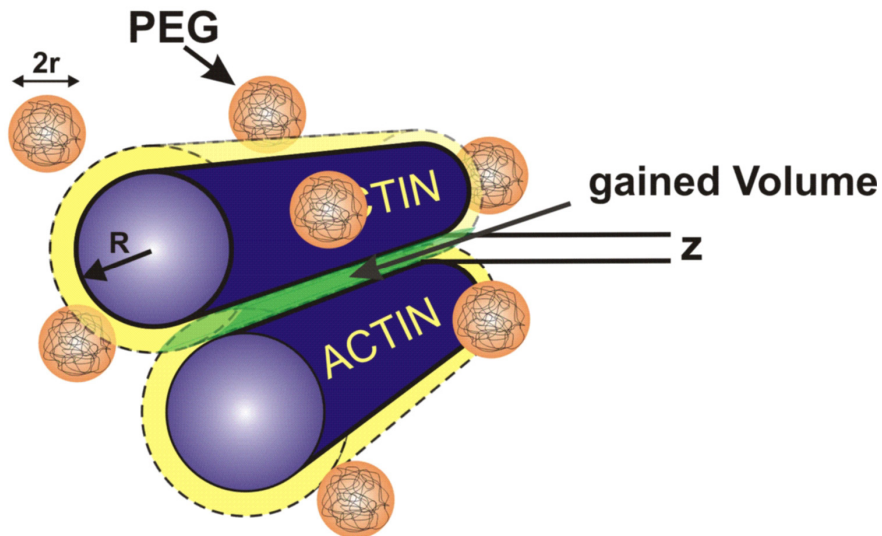


Figure 5-4 Schematic drawing of the expected interaction between actin filaments resulting from depletion force caused by PEG.

Note that for a maximal gain of free energy due to a maximal overlap volume the filaments have to be oriented in a parallel configuration. However, polymers have a high number of internal degrees of freedom which are hindered by the other polymers. Semi-flexible polymers like actin additionally interact in a strongly oriented potential

and have a high amount of other particles in the solvent. Therefore it is rather impossible to apply straightforward, analytical theories, like for example the classical theory of simple fluids for real soft matter (complex fluids), to explain the detailed behavior of actin under the influence of depletion potentials.

However, it has been shown by static light scattering, electron microscopy (EM), and fluorescence microscopy (FM) that above a critical concentration adding a typical depletion agent like PEG to actin solutions results in bundling of filaments (Suzuki et al. 1989; Suzuki et al. 1996; Hosek et al. 2004). PEG can be described in this context as a hard sphere system (Rudhardt et al. 1998). The observed structural rearrangements of the network are reminiscent to the structural changes induced by a high concentration of specific crosslinkers (Pelletier et al. 2003). However, for systems consisting of different crosslinker types different structural transitions have been predicted. While for depletion forces a direct cross-over from an isotropic to a purely bundled phase is predicted, mixed phases should occur for specific crosslinkers depending on the binding energies (Zilman et al. 2003; Borukhov et al. 2005).

5.2. Structure of Composite F-actin/PEG6k networks

The following measurements were done at room temperature (21°C). Polyethylene glycol with a molecular weight of 6000 Da (PEG6k) was added prior to the polymerization and the samples were gently mixed using pipettes with a cutoff tip. Polymerization assays observed in the fluorescence spectrometry of NBD (4-nitrobenzol-2-oxa-1,3-diazol) labeled actin showed that the presence of PEG was not significantly affecting the polymerization kinetics (Lindner et al. 1997).

The addition of PEG6K to the actin solution results in distinct changes in the network structure and morphology. Electron microscopy (EM) images showed that below a critical PEG6k concentration c^* actin filaments were organized as an isotropically disordered network (Figure 5-5 (a) and (b)). In this low PEG-concentration regime the appearance of actin bundles is rare; bundle formation starts at c^* (Figure 5-5 (c) and (d)). As soon as bundles begin to form in the network hardly any single filaments remain, as it is consistent with previous observations using light microscopy and static light scattering (Suzuki et al. 1989; Suzuki et al. 1996; Hosek et al. 2004). These

observations reaffirm that in the observed samples the isotropic network and bundled phases were non-coexistent in thermodynamic equilibrium. With increasing c_{PEG6k} , the cylindrical appearing actin bundles grew linearly in diameter (Figure 5-5 (e)) and the distance between the bundles increased.

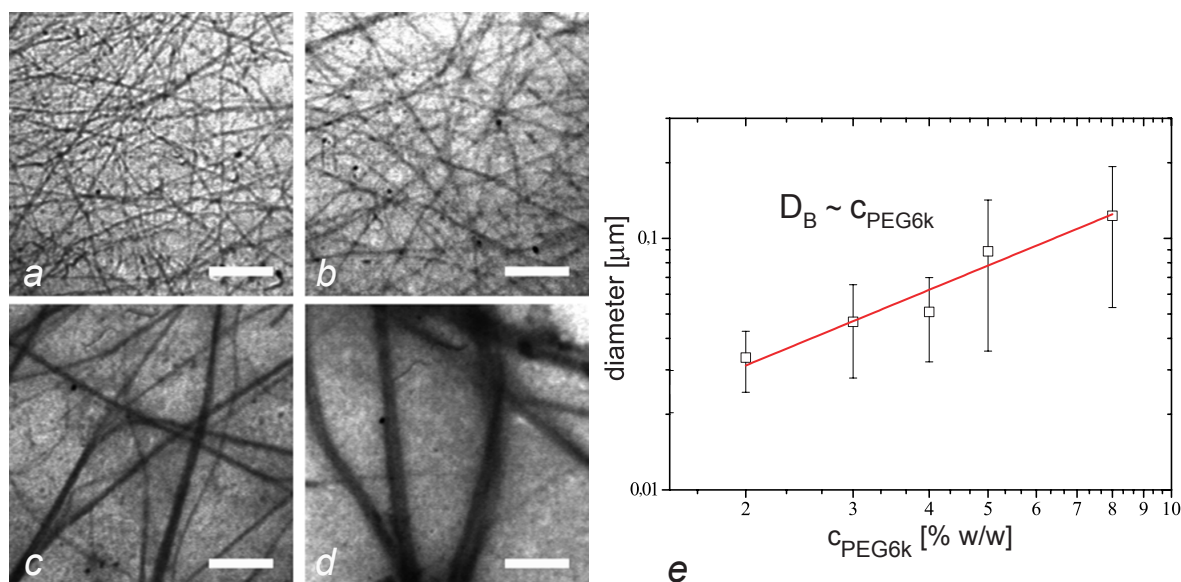


Figure 5-5 Electron microscopy pictures of composite F-Actin/PEG6k solution for different PEG concentrations ($c_{actin} = 9.5 \mu M$) (a) without any PEG and with the addition of PEG6k of (b) 1.5 % w/w, (c) 4 % w/w, and (d) 8 % w/w (scale bar 0.5 μm). (e) The increasing diameter of bundles determined by image analysis of the TEM pictures is shown. Below c^* no bundles were observed, whereas above c^* the diameter of the bundles increases linearly (solid line) with the PEG6k concentration ($c_{actin} = 9.5 \mu M$)

The bundle thickness was measured by drawing a line profile of 1 pix ($\approx 8nm$) diameter perpendicular to the bundle (Figure 5-6). The intensity distribution was fitted with a Gaussian fit function. The width of this Gaussian was assumed to be the diameter of the bundle. For each PEG concentrations about 20 bundles and about 5 different areas on the EM grid were analyzed. Figure 5-5 (e) shows the mean value of the width, and the error bars indicate the standard deviation.

In order to take care about the shortcomings and possible artifacts of analysis of EM pictures special care was taken during the preparation of the samples and different samples for each concentration were inspected. At yet higher concentrations of PEG (above 8%), complete demixing of the solution is observed. The network structure

changes dramatically above c^* , but even before bundling takes place smaller modifications in network properties are expected.

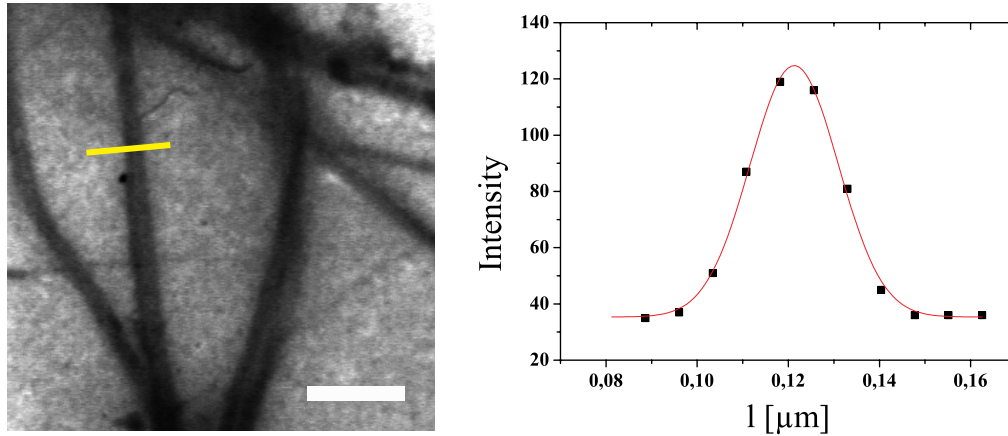


Figure 5-6 By drawing a line of 1 pix ($\approx 8\text{nm}$) diameter perpendicular to the bundle the intensity profile is observed. The width of the Gaussian fit of this profile yields the bundle thickness (scale bar $0.5\ \mu\text{m}$).

5.3. Rheology of Composite F-actin/PEG6k Networks

5.3.1. Linear Response

Concomitant with the observed local mechanical changes induced by increasing PEG concentration the macroscopic viscoelastic properties of the network are expected to alter. Increasing amounts of depletion agent increase the storage and loss moduli G' and G'' over the entire probed frequency range (Figure 5-7 b). The absolute values of the plateau storage modulus as a function of PEG concentration are in excellent agreement with the mean values obtained from microrheology. With an increasing elastic modulus the frequency dependence of G' and G'' becomes less pronounced. Simultaneously, the entanglement crossover time, τ_e , is shifted to higher frequencies, which implies that single filament fluctuations are hindered. At a c_{PEG6k} of 5 % w/w the elastic modulus G' is nearly constant over the whole frequency range and τ_e is shifted outside the probed frequency range. Plotting the plateau modulus G_0 at a frequency of 5 mHz against the depletion agent concentration (c_{PEG6k}) as shown in Figure 5-8 the two regimes separated by c^* can easily be distinguished. From the rheology data one obtain $c^* \approx 2\%$ w/w for $c_{actin} = 9.5\ \mu\text{M}$ which is somewhat lower than the 4-8% reported by others under similar

conditions (Suzuki et al. 1989; Hosek et al. 2004). The variation in values of c^* can probably be attributed to differences in the actin preparation and sensitivity of the method for the appearance of bundles.

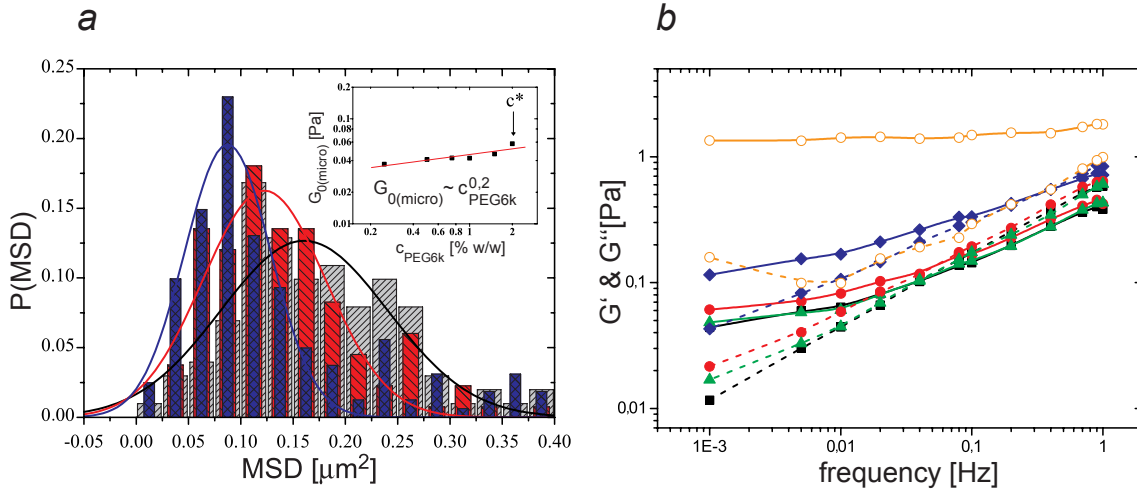


Figure 5-7(a) Histogram of the local mean square displacements of colloidal probe particles embedded in the actin network. Grey bars (dashed from left bottom to right top) represents pure actin, red (dashed from right bottom to left top) with addition of 1% w/w PEG, and blue with 2% w/w PEG. The center of the Gaussian fit (solid lines) can be used to calculate the plateau modulus at low frequencies as seen in the inset. Counts of beads were normalized by the maximal number of beads used for the distribution. (b) Frequency behavior of the moduli G' (solid lines) and G'' (dashed lines) for actin $9.5 \mu\text{M}$ (black, full squares), 0.6% w/w PEG6k (red, full circles), 1.25% w/w PEG6k (green, triangles), 1.9% w/w PEG6k (blue, diamonds), and 5% w/w PEG6k (orange, open circles).

In the regime below c^* we observe a small but significant increase of $G_0 \propto c_{\text{PEG6k}}^{0.2 \pm 0.1}$, consistent with the microrheological observations. The increase in the regime below c^* and the shift in τ_e can be explained by a continuous change from a regime where the entanglements and thus tube deformations dominate the elastic response to a regime where actin filaments are gradually pinned together and thus the force exerted on single filaments dominates the network. Forces exerted by depletion agents are homogeneous throughout the network, which implies that actin filaments are gradually pinned together more strongly with increasing PEG concentration - an increasingly stronger attraction corresponds to a deeper secondary minimum in the total interaction potential (Hosek et al. 2004). Changing the steepness of the minimum of the interaction potential results in increasingly effective crosslinks between the filaments and as a result the network behaves as if it was isotropically crosslinked. Thus the substantially lower

longitudinal thermal compliance of the filaments increasingly dominates the mechanical response of the network. This hypothesis agrees with the dependence of G_0 on c_{actin} ; while G_0 scales as $G_0 \propto c_{actin}^{7/5}$ in entangled networks (Hinner et al. 1998) a scaling of $G_0 \propto c_{actin}^{11/5}$ is reported for affine deformed crosslinked networks (Gardel et al. 2004). Below c^* , $G_0(c_{PEG6k})$ can only be fitted using one single prefactor for all actin concentrations when it is assumed that $G_0 \propto c_{actin}^{11/5}$ and the meshsize ξ is smaller than the length between crosslinks L_c (Figure 5-8)

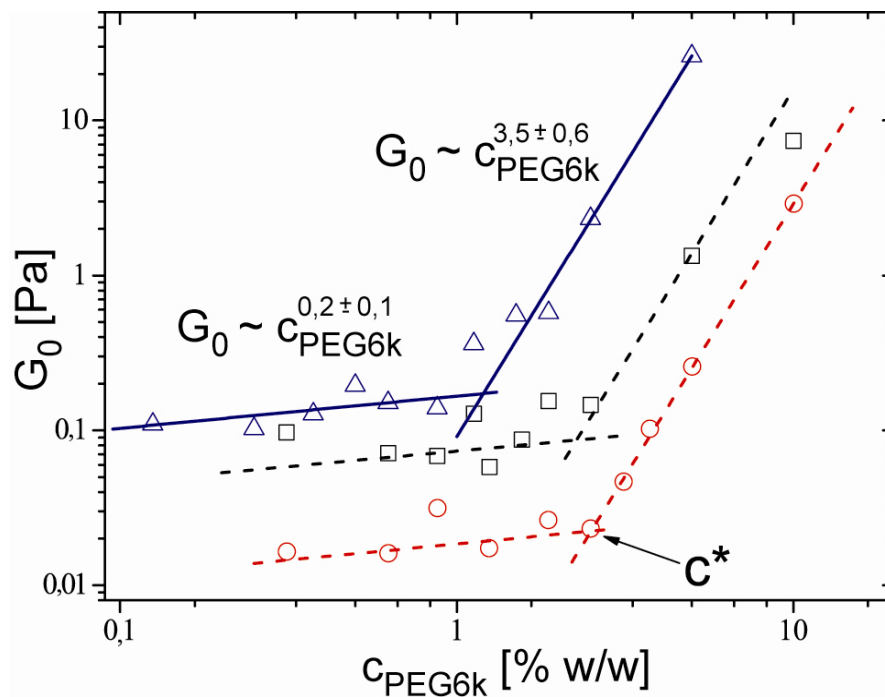


Figure 5-8 The macrorheological modulus G_0 as a function of c_{PEG6k} taken from the frequency spectra at 5 mHz. In the concentration dependence of the moduli two regimes can be distinguished: Below c^* we find a small increase of the moduli $G_0 \propto c_{PEG6k}^{0.2 \pm 0.1}$, while above c^* a steep increase is observable: $G_0 \propto c_{PEG6k}^{3.5 \pm 0.6}$. The actin concentrations are 4.75 μM (circles), 9.5 μM (squares) and 14.3 μM (triangles). The solid line is a best line fit to the experimental data (14.3 μM actin). The dotted lines below c^* are obtained by using the scaling for crosslinked networks $G_0 \propto c_{actin}^{11/5}$ with constant prefactor. Above c^* the dotted lines are obtained by renormalizing the data by c^* and using the observed scaling for crosslinked bundled networks $G_0 \propto c_{actin}^{5/2}$ with constant prefactor.

At c^* interfilament attractions become strong enough to overcome entropic contributions of single filament fluctuations (and mixing) and thus bundling becomes energetically favorable and a phase transition is observed (Hosek et al. 2004; Borukhov et al. 2005). Above c^* the appearance of a network of bundles results in a much more pronounced increase of $G_0 \propto c_{PEG6k}^{3.5 \pm 0.6}$ for all studied actin concentrations (Figure 5-8). The concentration c^* and thus the magnitude of the depletion forces needed to induce the structural transition depends on c_{actin} . Theoretical predictions for c^* depend on the microscopic interaction potential, taking into account explicitly not only the magnitude of the depletion force but also the standard DLVO potential between the charged filaments (de Vries 2001; Zilman et al. 2003; Hosek et al. 2004).

The moduli are determined by both the concentration and the mechanical properties of the bundles. Generally the network can be decomposed into statistically identical elastic unit cells of linear dimensions equal to the mesh size ξ as it is the case for foams and other cellular solids and the macroscopic response is simply the upscaled response of such a cell. The elastic response can be estimated by simple arguments and depends on whether the cell response is dominated by bending (Kroy et al. 1996) or stretching (Mackintosh et al. 1995) modes.

At a constant actin concentration the bundling of n filaments results in an increase of the mesh size $\xi \propto (n/c_a)^{1/2}$. The bending stiffness of the actin bundle will be strongly affected by the coupling of the filaments in the bundle. In the case of weak filament coupling where slip between the filaments is possible the following bending modulus is expected:

$$\kappa_B \sim \left(\frac{D_B}{D_0} \right)^2 \kappa_0 \sim n \cdot \kappa_0. \quad (\text{Eq. 5.2})$$

For the strongly coupled case we get:

$$\kappa_B \sim \left(\frac{D_B}{D_0} \right)^4 \kappa_0 \sim n^2 \cdot \kappa_0. \quad (\text{Eq. 5.3})$$

Therefore, if one assumes tight inter-filament coupling, the persistence length, L_p , of a bundle with a diameter D_B will increase as $L_p \propto D_B^4$ in accordance with theoretical predictions for homogeneous elastic rods (Landau et al. 1986; Shin et al. 2004; Claessens et al. 2005). Because the area of the bundle scales linearly with the number of filaments ($A \sim n \sim D_B^2$), the persistence length depends quadratically on the number of filaments ($L_p \propto n^2$).

In order to measure the bending stiffness of actin bundles G-actin is polymerized in the water phase of water in oil emulsion. When this is done in the presence of PEG6K, the filaments bundle and organize into a ring (Figure 5-9) (Claessens et al. 2005). By analyzing the fluctuation amplitude of this ring it is possible to extract the persistence length, l_p , of the bundles. Filaments bundled by PEG show a clear quadratic increase of $l_p(n)$ independent of the concentration of PEG.

It is interesting to note that in the affine-bending dominated case the effect of bundling is predicted to be canceled out by the shear modulus, since the increase in stiffness of the bundles is exactly balanced by the increase in mesh size. In the stretching-dominated case stiffening with increasing number of filaments in the bundles is predicted when $L_c = \xi$:

$$G_0 \propto \frac{l_p^2}{\xi^5} \propto n^{\frac{3}{2}}. \quad (\text{Eq.5.4})$$

In order to obtain the experimental observed dependence of $G_0 \propto c_{PEG6k}^{3.5}$ the number of filaments in the bundle should scale as $n \propto c_{PEG6k}^{2.3}$ and therefore the bundle diameter ($D_B = 2r$) should scale with the PEG6k concentration $D_B \propto c_{PEG6k}^{1.2}$. Indeed, by measuring the bundle thickness in pictures obtained by TEM a nearly linear increase of the mean bundle thickness can be observed Figure 5-5 (e). The increase of $G_0(c_{PEG6k})$ for the different actin concentrations can again be fitted using one prefactor. However, now the data has to be rescaled on the onset of the bundling regime, c^* ; the plateau modulus now scales as $G_0 \propto c_{actin}^{5/2}$, consistent with Eq.5.4 (Figure 5-8).

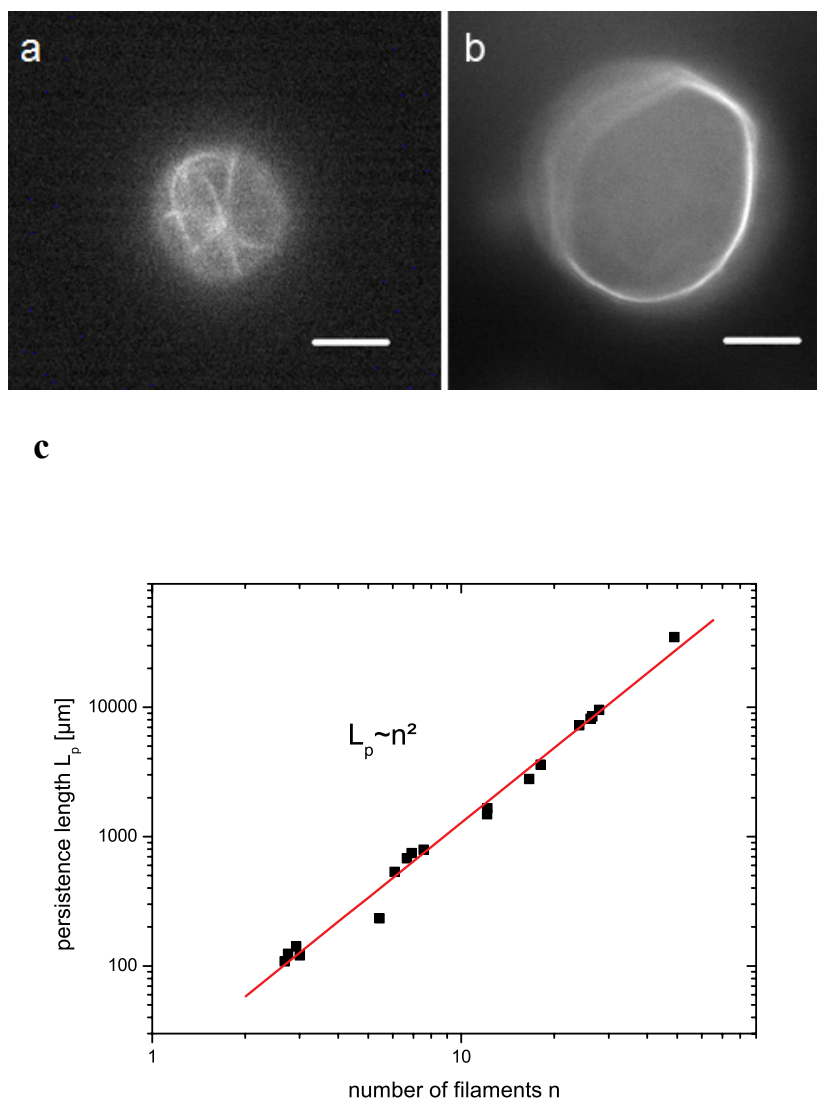


Figure 5-9 Derivation of the bending stiffness of actin bundles induced by the addition of PEG. a) Picture of an emulsion droplet containing labeled actin filaments without PEG. b) The addition of PEG results in a bundle where filaments are organized into a ring. c) By analyzing the fluctuation amplitude of this ring it is possible to extract the persistence length l_p of the bundles.

5.3.2. Nonlinear Response

The theory of linear viscoelasticity is limited to small deformations of the sample where the strain depends linearly on the applied stress. When the stress or strain of the sample is increased further the network response reveals a nonlinear behavior. If the elastic response decreases with increasing strain one speaks of strain weakening, whereas an increasing elastic response is called strain hardening.

The nonlinear response of 3-dim. semiflexible polymer networks is poorly understood. Both strain weakening and strain hardening were observed in actin networks. In actin networks with low crosslinker densities a strain weakening was measured and a strain hardening was found for actin networks with high crosslinker densities and bundles (Gardel et al. 2004). Recently reported models (Gardel et al. 2004; Storm et al. 2005) that should explain the strain hardening of densely crosslinked and highly entangled semiflexible polymer networks assume an affine network deformation. As already mentioned, this allows a scaling of the network response to the properties of single filaments. Experimental results suggest that the elastic response of these networks is dominated by stretching out thermal fluctuations of filaments as it is described above (Chapter 3.3.2). Therefore strain hardening might be understandable on the basis of the wormlike-chain model (WLC) (Kovacs et al. 1986). Thermal fluctuations reduce the end-to-end distance of the polymer and act as an entropic spring (Figure 3-6). For forces in the order of $F \sim k_B T / L_p$ it is possible to describe the force extension behavior $F(d)$ (d = polymer end-to-end distance) of a WLC-polymer by an interpolated formula developed from Marko and Siggia (Marko et al. 1995):

$$F = \frac{k_B T}{L_p} \left(\frac{d}{L} + \frac{1}{4 \left(1 - \frac{d}{L}\right)^2} - \frac{1}{4} \right) \quad (\text{Eq.5.5})$$

At high extensions, the end-to-end length d approaches the contour length L and the force diverges (in networks d corresponds to the distance between which the fluctuations are pulled out, therefore L_e or L_c).

It is known that it is not trivial to determine experimentally the elastic moduli G' of actin networks as at high stresses or strains the response is no longer linear with the applied force. To overcome this problem the Weitz group (Gardel et al. 2004) superposes a small oscillatory stress $d\sigma$ on top of a constant applied stress σ_0 . Analog if one wants to know the differential modulation of the force extension behavior under an applied external force F , Eq.5.5 can be rewritten in the following way:

$$F(d \rightarrow L) \sim \frac{1}{\left(1 - \frac{d}{L}\right)^2} \Rightarrow \frac{\partial F}{\partial d} \sim \frac{1}{x^3} \quad \text{für } x = \left(1 - \frac{d}{L}\right). \quad (\text{Eq.5.6})$$

$$\text{Since } x \sim F^{-\frac{1}{2}} \Rightarrow \frac{\partial F}{\partial d} \sim F^{\frac{3}{2}} \quad (\text{Eq.5.7})$$

Therefore for the nonlinear response of actin networks is analog interpretable to Eq.5.7

$$K' \Big|_{\sigma_0} = \frac{\partial \sigma}{\partial \gamma} \Big|_{\sigma_0} \sim \sigma_0^{3/2}. \quad (\text{Eq.5.8})$$

K' defines the differential elastic modulus that is measured under linear deformation at a certain prestress σ_0 . However this technique is only applicable to networks for which the viscous response during the measurement can be neglected which is not the case for entangled and weakly crosslinked networks. The response of entangled and weakly crosslinked actin networks will depend crucially on the time scale at which the network is probed (Xu et al. 2000). Viscous flow in the entangled networks during the experiment might be responsible for the observed strain weakening mentioned above (Figure 5-12 (b)). Furthermore it is questionable if thermal fluctuations of single filaments dominate the nonlinear response in networks that contains a high amount of very stiff bundles (Gardel et al. 2004; Gardel et al. 2004).

To eliminate possible time effects in this study the strain was increased at constant shear rate and the response of the sample was recorded. Stress-strain measurements on entangled actin networks clearly show that $\sigma(\gamma)$ depends crucially on the applied shear rate (Figure 5-10). At low shear rate only small shear stiffening is observed while for shear rates above 0.125 s^{-1} the response seems to be independent of the shear rate. This effect can possibly be attributed to rearrangements of the network at longer timescales.

Figure 5-11 show prestress experiments and stress-strain curves respectively. Both measurements result in a strain hardening of pure entangled actin solutions. In the prestress experiment one data point took 20 seconds and was obtained at 0.5 Hz lower frequencies will give rise to longer measurement times. Therefore the time effect will also play a role in prestress experiments.

The stress-strain curves of actin and crosslinked rigor-HMM/actin networks can be directly fitted by the WLC-model from Eq.5.5 resulting in a good agreement at small deformation, but at higher deformation a softer behavior dominates which may be attributed to rearrangements of the network until it is completely destroyed at high deformation.

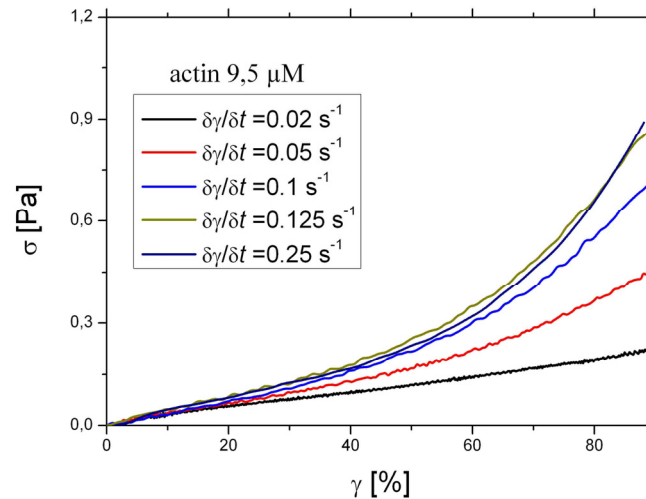


Figure 5-10 To eliminate possible time effects the strain is increased at constant shear rate and the response of the sample is recorded. The graph clearly shows that $\sigma(\gamma)$ depends crucially on the applied shear rate. At low shear rate only small shear stiffening is observed while for shear rates above 0.125 s^{-1} the response seems to be independent of the shear rate.

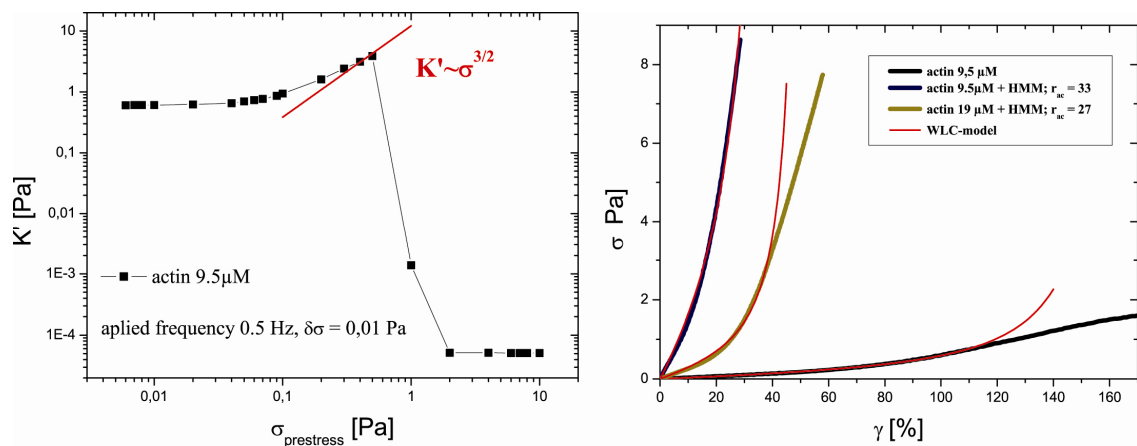


Figure 5-11 The graphs show a comparison between prestress experiments (left) and stress-strain curves (right). The poor agreement of the prestress experiments with the predicted scaling behavior from Eq.5.8 (red straight line) might be attributed to time and rearrangements effects of the network. The stress-strain curves of pure actin and composite rigor-HMM/actin networks (right graph) can be fitted by the WLC-model from Eq.5.5 (red line).

Besides the general considerations pointed out above, it was recently shown that the nonlinear response of a purely entangled actin network is also dependent on filament length, temperature and ionic strength (Semmrich 2005). But a more detailed analysis of the nonlinear behavior and comparison of different measurement methods are still necessary.

To underline the hypothesis that the attraction between the filaments is becoming stronger with increasing depletion forces, measurements to probe the onset of the nonlinear regime were performed.

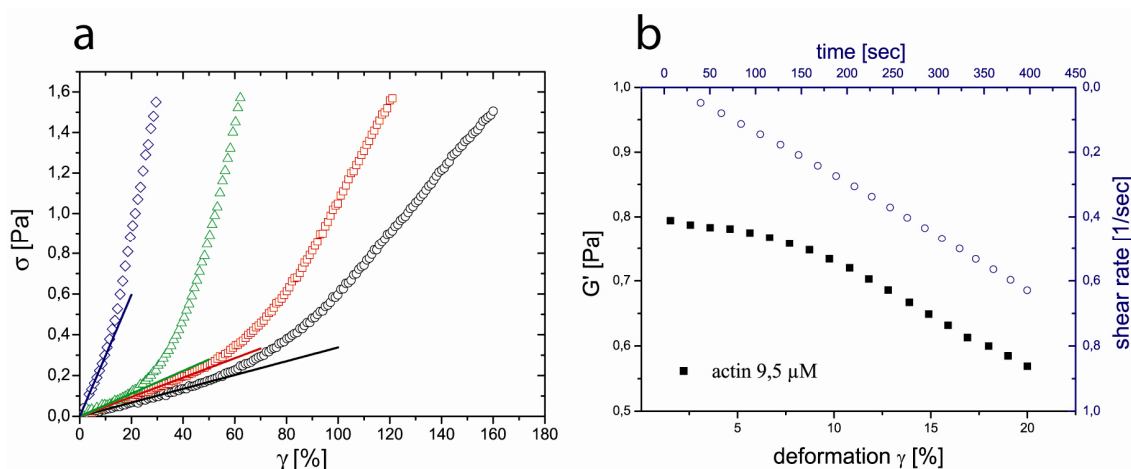


Figure 5-12 a) The nonlinear regime was probed by shearing the sample at a defined shear rate of 12.5%/sec. The stress is increasing with the strain first linearly while starting at a well defined strain a non-linear stiffening response occurs which is observed for actin 9.5 μ M (circles), addition 1% w/w PEG6k (squares), addition 1.5% w/w PEG6k (triangles), and addition 2% w/w PEG6k (diamonds). The increase in the slope $\delta\sigma/\delta\gamma$ of the linear response regime corresponds to the observed increase $G_0 \sim c_{PEG6k}^{0.2 \pm 0.1}$ obtained from the macro- and microrheological measurements. b) Classical measurement probing the non-linear behavior. With increasing amplitude of an oscillatory strain (0.5Hz) a strain weakening was observed for pure entangled F-actin (9.5 μ M).

A strong prediction of the model that is used to fit $G_0(c_{PEG6k}, c_{actin})$ is that with increasing crosslink density the non linear response regime starts at decreasingly smaller deformations. When deforming the composite networks at a constant shear rate below c^* the onset of non-linear elasticity decreases almost linearly ($\sim 25\%/PEG\%/w/w$) with increasing concentration of depletion agent (Figure 5-12 (a)). This suggests that increasing attractions between the filaments is equivalent to an increasing crosslinker density. The rise in the initial slope $\delta\sigma/\delta\gamma$ of the linear response regime corresponds to

the observed increase $G_0 \sim c_{PEG6k}^{0.2}$ obtained from the macro- and microrheological measurements.

5.3.3. Discussion

However, the detailed mechanism of the elastic response in the regime above c^* is not necessarily fully understood. It is important to realize that as a consequence of the quadratic dependence of the persistence length on the number of filaments in the bundles already bundles of 10 filaments have persistence lengths in the millimeter range. It is hard to imagine how a linear response is still dominated by entropic contribution with such stiff rods. As it was recently convincingly demonstrated for two-dimensional random fiber networks (Heussinger et al. 2006) the simple cell model is not applicable to elastic rod networks so that the proper explanation for the observed increase in elasticity may be somewhat more complicated. Only mesoscopic simulations will enable a further understanding the underlying physics (Head et al. 2003; Wilhelm et al. 2003; Heussinger et al. 2006; Heussinger et al.).

A phase transition from an isotropically crosslinked network to a microgel and finally to a network of bundles has been observed in α -actinin-crosslinked networks (Tempel et al. 1996). In contrast to these specifically crosslinked networks the unspecific-acting depletion forces induce a direct transition of the isotropically crosslinked network to a pure network of bundles, whereas a microgel formation can not be observed. The rheological properties reveal structural changes and changes in the effective interaction inside of each phase. The observed dependence of $G_0(c_{PEG6k})$ above c^* is much stronger for the depletion forces than for short rigid crosslinkers like scruin, where the moduli scale with $G_0 \propto c_{CL}^2$ (Gardel et al. 2004; Shin et al. 2004). This can be attributed to the fact that for depletion forces a pure bundle-phase is observed, while for scruin a mixed phase of bundles and an isotropic network was observed. This suggests that the scaling of the moduli with the crosslinking molecules gives a measure for the bundle effectiveness of the crosslinking molecule. The bundle effectiveness of the crosslinking agent will depend on the geometry of the binding domains and the interaction energies of the crosslinker. These determine whether a purely bundled network or an isotropically crosslinked network mixed with bundles or even a nematic phase is present (Borukhov et al. 2005). Specific crosslinkers can only bind to specific places and the

bundling is limited by their geometry and the discrete crosslinker density (Wagner et al. 2005). The continuously-increasing, homogenous attraction induced by depletion agents acts along the full filament length and thus bundling is most effective. Interestingly, for networks crosslinked by specific crosslinkers such as α -actinin or scruin no increase at low concentrations was observed and a strong increase of the moduli started already at concentrations of about $1\mu\text{M}$, which is roughly a factor of 10^3 less than observed for the unspecific depletion forces.

The stability of the solution and the observed demixing above 8% PEG suggest that a finite equilibrium bundle size exists in a defined range of PEG concentrations. As the depletion attraction should increase with increasing bundle diameter the equilibrium bundle size should be attributed to a repulsive interaction between the bundles. This repulsion may arise from interactions between bundles which could be elastic and which are overcome at high PEG concentrations where the full demixing of the solution is observed (Henle et al. 2005). However, further investigations of this phenomenon, which go beyond the scope of this thesis work, are necessary to fully understand the observed phase behavior.

6. Active- and Rigor-State in Actin-Myosin Networks

As mentioned in chapter 2, Myosin II acts as an enzyme, which is able to convert chemical energy due to ATP hydrolyzation to mechanical energy. Two states can be observed in nature: first an active highly non equilibrium state when myosin act as active motor under ATP excess and second the rigor state under ATP depletion. In excess of ATP the rate limiting step in the rotating crossbridge cycle is the binding of the molecular motor to the filament (Chapter 2.3). Due to the non-processivity of HMM, the motor molecules diffuse through the sample volume in ATP excess. In time more and more ATP is used up due to the hydrolysis cycle of the motors and ATP depletes in the whole sample volume. Hence the binding of the nucleotide is the rate limiting step in the hydrolysis cycle which depends on the concentration and diffusion of the ATP molecules. The time the motor stays connected to the filament τ_{on} increases with decreasing amount of ATP. This attached time τ_{on} is an important parameter in the concept of the duty ratio (Howard 1997) which allows the classification of the motors by processivity, non-processivity and speeds. During each crossbridge cycle, the motor domain spends an averaged time attached to the filament, τ_{on} , during which it makes the working stroke and an averaged time detached from the filament, τ_{off} , during which it makes its recovery stroke. By recovering during the detached phase, the motor avoids taking a step backwards, and thus progresses through a distance along the filament equal to the working distance δ (Figure 6-1). The measured working distance of myosin II differs with the applied technique (Finer et al. 1994; Mehta et al. 1997; Tyska et al. 1999). The consensus is that the unloaded working distance is 5nm.

The duty ratio is defined by the time the motor domain stays attached to the substrate divided by the total time of the crossbridge cycle:

$$r = \frac{\tau_{on}}{\tau_{on} + \tau_{off}} = \frac{\tau_{on}}{\tau_{total}} \quad (\text{Eq.6.1})$$

If a two-headed motor is able to maintain continuous attachment to the substrate, the duty ratio of each head has to be at least 0.5 otherwise there are times where a complete

detachment is possible and the motor is able to diffuse away. In contrast to latter processive motors the duty ratio of fast skeletal muscle myosin from vertebrates is small $r \sim 0.01$ to 0.02 (Howard 2001).

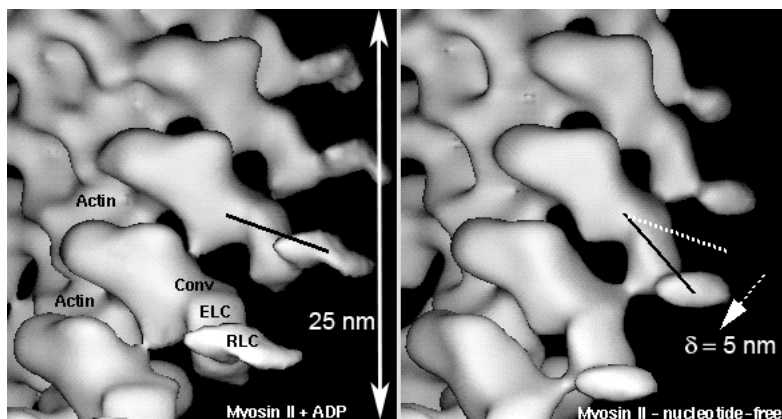


Figure 6-1 Comparison of the ADP (left) and nucleotide-free (right) 3D maps of smooth muscle myosin II attached to F-actin (taken by cryo electron microscopy). Solid lines indicate the long axes of the calmodulin or light chain binding domains of the myosin. Arrow show the direction of rotation and the working distance when ADP is released. The rotation is roughly 23° for myosin II. (source: (Wells et al. 1999), <http://www.mrc-lmb.cam.ac.uk/myosin/Structures/cryoEM.html>;))

Since an ATP is needed for the release from the filament, the binding of ATP is the limiting step in the chemo-mechanical cycle when ATP is depleted. This leads to an increase of τ_{on} , the time the motor is bound to the filament. Therefore more and more motors trapped in rigor state (step (a) Figure 2-1). Without additional ATP, myosin is bound strongly to actin and can act as effective crosslinker due to the two heads. Thus with increasing amount of motors in rigor state, the network elasticity increases.

The phase transition from a sol like to a gel like network can be experimentally observed by micro and macro rheology (Figure 6-2). In all experiments with molecular motors, they were added in a molar ratio $r_{ac} = c(\text{actin})/c(\text{crosslinker})$ to the actin sample before polymerization was started with standard F-buffer (see Appendix C). To adjust the mean length of actin filaments to $21 \mu\text{m}$ gelsolin was added to the sample in the molar ratio of actin to gelsolin $r_{A/G} = 1/7770$ before initiating polymerization (Janmey et al. 1986). All measurements were done at room temperature 21°C . Samples were gently mixed with pipettes with a cutoff tip.

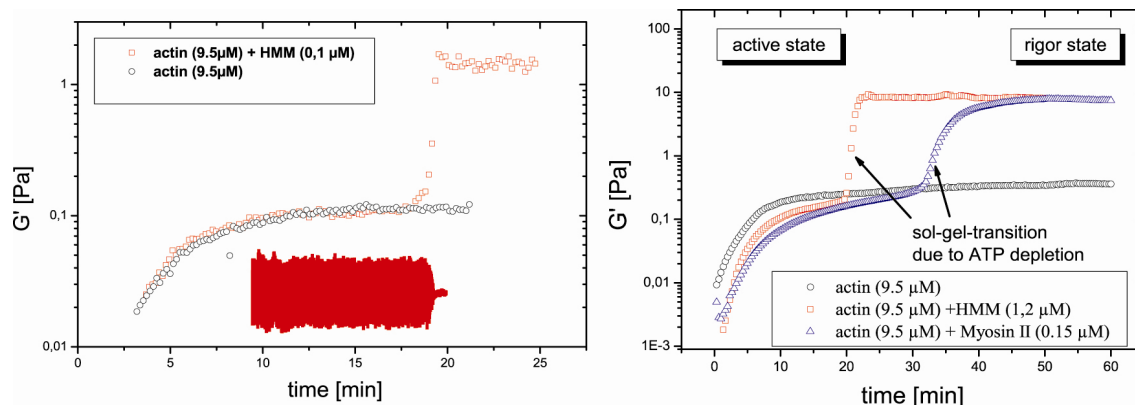


Figure 6-2 The graphs show the detection of the sol-gel transition by rheological method. Left graph shows the ATP depletion that is accompanied by an increase in the elastic behavior G' of an actin-HMM network measured by magnetic tweezer (inset visualizes the behavior of the bead amplitude). Right graph represents the ATP depletion of a HMM/actin- and a Myosin II/actin network measured by the rheometer Physica MCR301.

For measurements in the active state ATP was added before polymerization in excess ($\geq 2mM$). To be sure that actin is already polymerized and no significant change in the viscoelastic behavior is expectable the measurements were started after one hour of polymerization. For measurements in rigor state, the appearance of the sol-gel transition was adjusted to $t_{transition} > 20$ minutes by an initial ATP concentration that was added to the sample before polymerization. This is the time where actin polymerization reaches the plateau and further small changes in the length distribution of the actin filaments are neglectable. Since actin-myosin II networks are not measurable with the magnetic tweezer method (due to the myosin filaments (chapter 2.3) the network structure exhibit extremely heterogeneous) the majority of experiments were done with the commercial macrorheometer “Physica-MCR301”. If not it is explicitly mentioned in the following chapters.

The increase of the motor concentration in the sample results in a higher consumption of ATP and therefore shifts the sol-gel transition to shorter times. Figure 6-3 shows both, the temporally appearance of the transition in dependence of the molecular motor concentration at a fixed actin concentration (9.5 μ M) for HMM and Myosin II. It comes out that the transition time is inverse proportional to the motor concentration in the measured range ($r_{ac} = 320 - r_{ac} = 1$) for both motor proteins. This linear behavior is expected and the scaling behavior for HMM/actin networks that was observed by

magnetic tweezer in a range from $r_{ac} = 880 - r_{ac} = 88$ ($t_{sol-gel\ transition} = c_{HMM}^{-0,75}$; (Keller 2003)) is somewhat lower to the macroscopic observation.

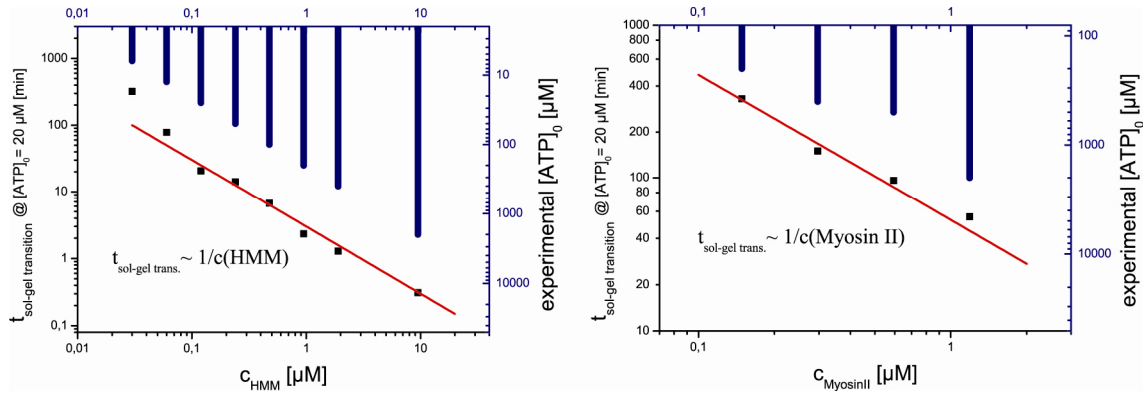


Figure 6-3 Both graphs show the temporal appearance of the sol-gel transition due to ATP depletion in dependence of the molecular motor concentration (left: HMM, right Myosin II). Since the transition time passes four orders of magnitude the initial experimental ATP concentration has to be adjusted (for low HMM concentrations the concentration of the initial ATP has to be low. Otherwise the appearance of the transition takes time of several days.) The blue bars indicate the used initial experimental ATP concentration. To determine the appearance of the sol-gel transition in dependence of the motor concentrations, the experimental observed transition time is extrapolated to an initial ATP concentration of 20 μM . The actin concentration was kept constant ($9.5\mu\text{M}$; standard F-buffer conditions). For both Myosin II and subfragment HMM an inverse proportionality is observed.

The sol-gel transition is predictable by the use of following formula (Keller 2003):

$$t_{transition} = \frac{[ATP]_0}{[M]_0 \cdot k_{ATPase}} \quad (\text{Eq.6.2})$$

k_{ATPase} describes the over all ATPase rate, $[ATP]_0$ is the initial ATP concentration and $[M]_0$ is the initial motor concentration. For HMM one has to take into account that this is a nonprocessive, soluble motor that releases the filament after one hydrolysis cycle, and therefore the motor protein need time to diffuse to another actin filament where the motor can execute another hydrolysis cycle. Thus, the ATPase rate in 3.-dim. networks is limited in the beginning by the diffusion of the motor molecules. The time between two contacts of the motor with the actin filaments can be estimated by some assumption and the use of the equation of diffusion (Keller 2003). The outcome is a maximal contact rate $k_{contact} \approx 4.5s^{-1}$. In contrast the processive microneedle of myosin II should result a similar ATPase rate that is observed by different kind of measurements $k_{ATPase} \approx 20s^{-1}$ (Howard 2001).

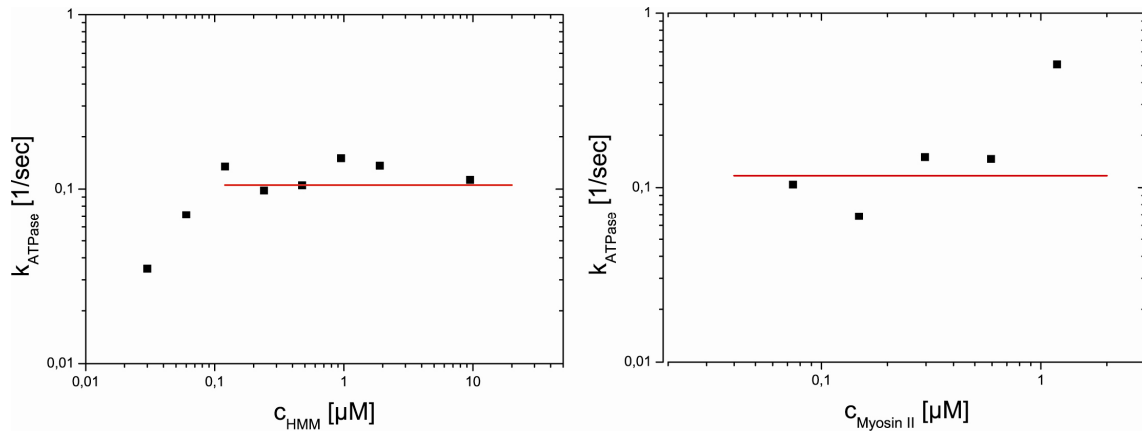


Figure 6-4 For both actomyosin systems an ATPase rate of 0.1 s^{-1} was observed by macrorheology. The left plot shows a decrease in the ATPase rate for low HMM and ATP concentrations. This results from HMM molecules in rigor state which have to wait till an ATP molecule enables the release from the filaments.

The results from experiments (actin concentration of $9.5 \mu\text{M}$) show an ATPase rate of 0.1 s^{-1} for both HMM and Myosin II. This is far away from the maximal ATPase rate of 20 s^{-1} for fast skeletal myosin or even the contact rate 4.5 s^{-1} for HMM. It has been shown that the salt concentration and therefore the Debye screening length play a crucial role during the specific interaction of the actomyosin complex (Keller 2003). It is assumed that the motor domain is preoriented by electrostatic interactions before it executes the powerstroke. This measurement is further evidence that the observed ATPase rate in such 3 dimensional networks is mainly dominated by the used salt concentration (Uhde 2004). The left plot in Figure 6-4 shows a decrease in the ATPase rate for low HMM and ATP concentrations resulting from HMM molecules in rigor state which have to wait for an ATP molecule enables the release from the filaments. This effect is also responsible for the drastically increased duration of the transition.

7. Rigor-HMM/Actin Network (rigor state)

The previously mentioned increase in τ_{on} with decreasing amount of ATP corresponds to an increase of the duty ratio r and enables a phase of active directed transport during ATP depletion. This effect was observed and analyzed in detail (Uhde et al. 2004). When ATP is completely consumed the network ends up in rigor state. All motor heads are strongly bound to actin and HMM molecules can act as crosslinks between actin filaments. It is assumed that crosslinks are formed at intersections of the filaments. The increasing amount of crosslinks in the network is visible as increase in the elastic response (the sol-gel transition). Further, it is expected that after crosslinking the network will be frozen in the isotropic, homogeneous form as observed for the pure entangled networks. Further it is assumed that the motors bind just with one head to an actin filament due to high crosslinking ability, whereas the other independent head is dangling around or just weakly bound and waiting to bind to another suitable actin filament (Margossian et al. 1978; Offer et al. 1978; Wendt et al. 1999; Berger et al. 2001; Wendt et al. 2001). However, in the literature there is still a controversy, since the complexity of the binding to actin is additionally regulated by the phosphorylation of the regulatory light chains in smooth and non muscle HMM. For skeletal HMM used in this studies even less is known. Some groups reported, that HMM is able to bind with two heads to one filament (Eisenberg et al. 1972; Greene et al. 1980; Tyska et al. 1999; Ellison et al. 2003). This point has still to be clarified.

7.1. Structure of Rigor-HMM/Actin Networks

Visualizations of rigor-HMM/actin networks with microscopic techniques confirm the assumed homogeneity of the crosslinked network. Figure 7-1 (a) represents a weighted back projection of an actin network mixed with HMM in an äquimolar crosslinker density $r_{actin/crosslinker} = 1$ observed with 3-dim.-cryo tomography (chapter 4.2.3). The image clearly shows on a nanometer scale actin filaments that are decorated with molecular motor. The decoration of filaments with HMM leads to a distinct arrowhead structure which was also observed previously for HMM (Huxley 1963; Ishikawa et al.

1969; Moore et al. 1970). Since the high moduli measured suggests a high amount of crosslinks in rigor state, the cross sections of the filaments in the image should represent crosslinks between filaments. The picture demonstrates that between intersections, motors just stay on the filament without crosslinking. To gain more spatial information, individual motor molecules were identified on the filament by the method of template matching (Figure 7-1 (b)). For this the detailed image of S1 (template) were used to search the entire volume of the tomogram⁵ by cross-correlation. Since the network shrinks in the blotting process, characteristic length scales are not available from the tomogram. The most important result obtained from the cryo-pictures is that even at highest motor concentrations no bundles are formed in the complex network.

Similar results were obtained from electron microscopy using the technique of negative staining (Figure 7-2 (b) and (d)). The micrographs show an isotropic crosslinked network without any bundles.

In contrast to the agreement in the isotropic disordered structure between pure and rigor-HMM/actin networks, a distinct difference is observable in the fluorescence pictures. Fluorescence microscopy of rigor-HMM/actin networks (Figure 7-2 (a) and (b)) reveal a strained network with sharp edges ($< 90^\circ$) on a μm scale (Figure 7-2 (e)). This strained state was also observed by Jörg Uhde and Manfred Keller after the active transport phase (Uhde et al. 2004).

⁵ Special thanks for the image-analysis to Anna Sartori, Julio Ortiz and Marek Cyrklaff from the Max-Planck-Institute for Biochemistry, Dept. of Molecular Structural Biology.

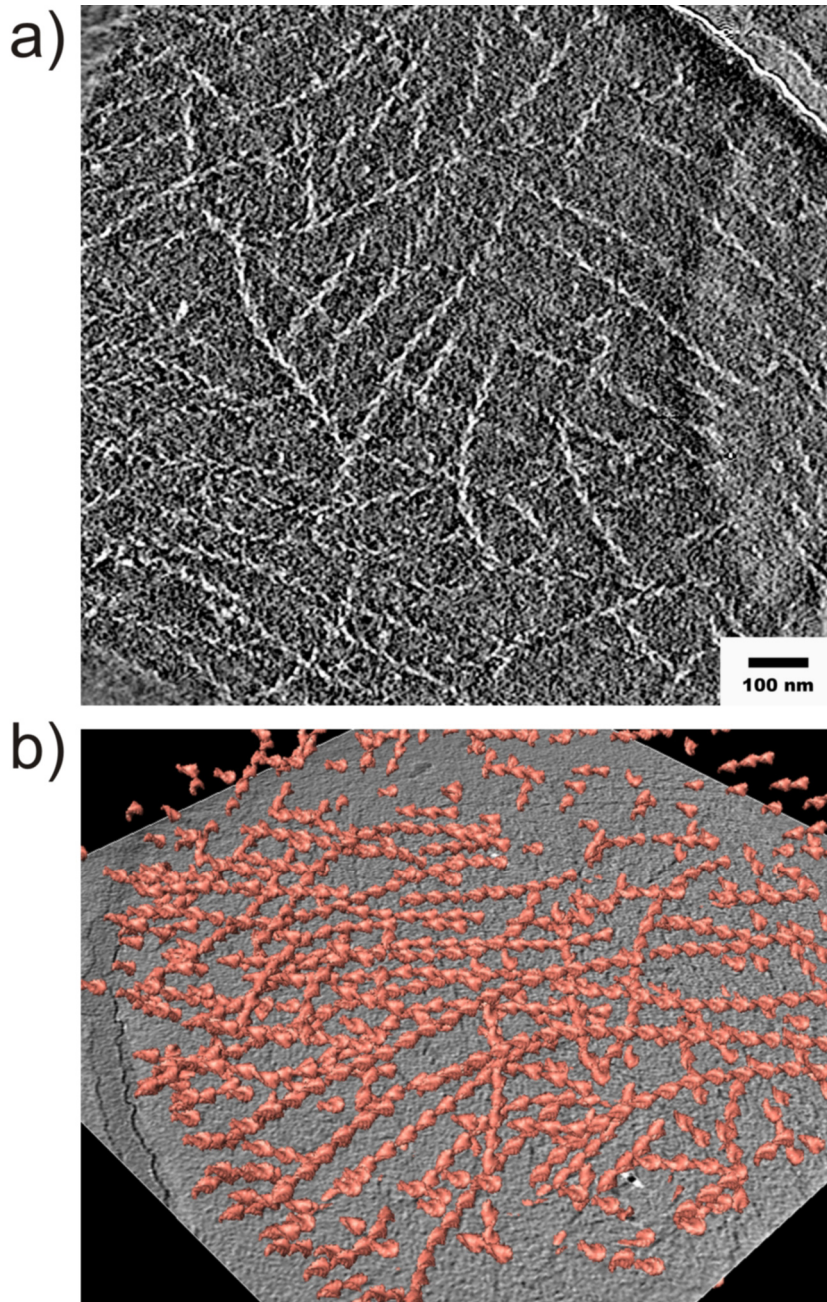


Figure 7-1 Picture (a) represents a weighted back projection of an actin network mixed with HMM in a ratio $r_{ac} = 1$ observed with 3dim-cryo tomography. The image clearly shows the actin filaments which are decorated by the molecular motor. The decoration of filaments with HMM leads to this distinct arrowhead structure in a distance that is equal to the actin twist repeats of 37 nm (Huxley 1963; Ishikawa et al. 1969; Moore et al. 1970). (b) By image analysis a 3-dim. reconstruction of the network is possible. For template matching the observed structure of S1 was used since the arrowhead structure looks similar to that of actin filaments decorated with S1 (Holmes et al. 2003).

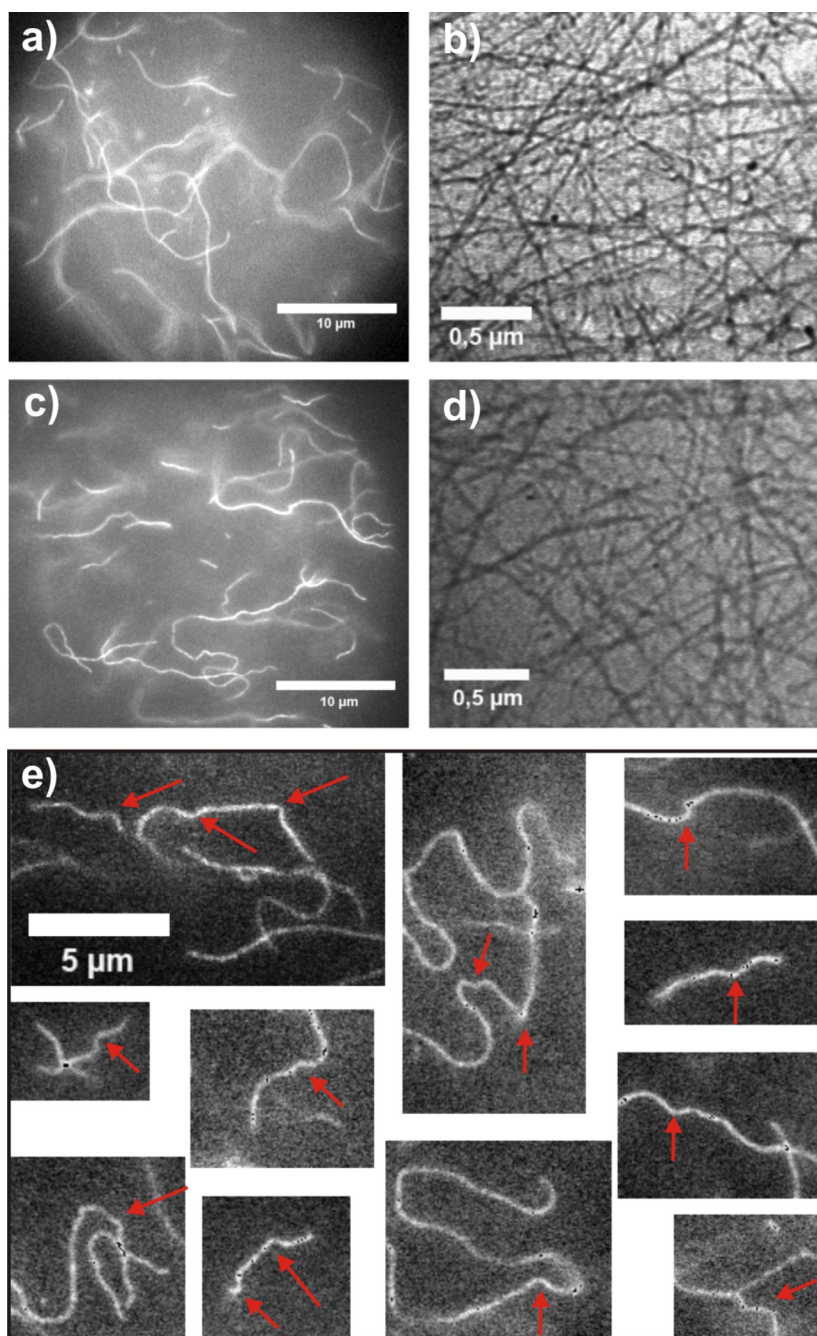


Figure 7-2 Fluorescence image of a pure entangled actin sample (a) (actin concentration $23.8 \mu\text{M}$, 1 reporter-filament/ 500 unlabeled filaments, adjusted filament length $21 \mu\text{m}$). (c) represents the same actin network after addition of HMM (ratio $r_{ac} = 5$). (b) and (d) show electron microscopy picture of the networks shown in (a) and (c) respectively. The strained filaments that can be found in rigor-HMM/actin networks are enlarged in (e).

Since still small amounts of ATP may diffuse through the sample volume in the rigor state, a possible explanation for these edges might be a powerstroke event after the sol-gel transition. Referring to the Euler force (Howard 2001)

$$F_c = \pi^2 \frac{EI}{L^2} = \pi^2 k_B T \frac{L_p}{L^2}, \quad (\text{Eq.7.3})$$

a single motor head that is able to generate a lateral force onto the filament of 1.5 pN, that causes buckling of the filament or stretching out thermal fluctuations to a critical length of $\approx 0.7 \mu\text{m}$. This is somewhat higher than the meshsize and possibly will be responsible for sharp edges and kinks in the fluorescence microscopy images.

7.2. Rheology of Rigor-HMM/Actin Networks

7.2.1. Linear Response

In a pure isotropically crosslinked network the stress is transmitted through the network in an affine way. Rheological measurements of HMM/actin networks in rigor state were performed 10 minutes after the observation of the sol-gel transition. Increasing amounts of HMM increase the storage and loss moduli G' and G'' over the entire frequency range probed (Figure 7-3, left hand). An extrapolation of G'' and G' to a high frequency regime suggest that the entanglement crossover time, τ_e , shifts to higher frequencies. Similar to the observations in composite PEG6k/actin networks this implies decreasing fluctuations of individual filaments. For crosslinker densities $r_{ac} < 500$ a distinct minimum in the frequency dependence of the loss modulus G'' can be observed. This minimum in G'' defines the frequency at which the plateau modulus G_0 is mostly pronounced. Plotting the plateau modulus G_0 over the crosslinker density shows a scaling $G_0 \sim r_{ac}^{-1.2}$ (Figure 7-3, right hand). A higher actin concentration shifts the curves parallel to higher values without changing the scaling of G_0 . Therefore the scaling $G_0 \sim r_{ac}^{-1.2}$ can be just attributed to the increase in crosslinker concentration. At high crosslinker densities $r_{ac} < 10$ no further increase of G_0 is observable; G_0 even decreases slightly. A reasonable explanation might be that for high HMM concentrations the mean distance between the molecular motors is smaller than the mesh size.

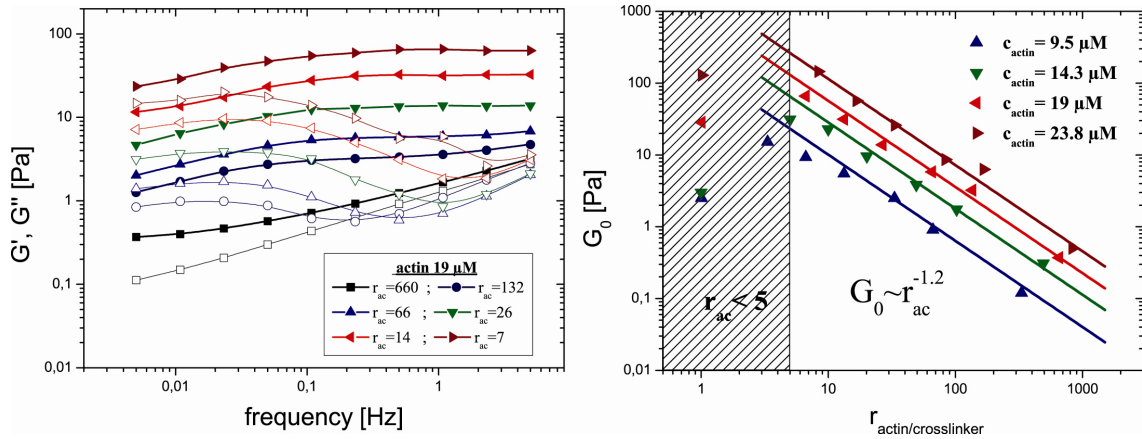


Figure 7-3 Left: Frequency dependence of the moduli G' (full symbols) and G'' (open symbols) for a composite rigor-HMM/actin network at different HMM concentrations (actin concentration $19 \mu\text{M}$). Right: When plotting the plateau modulus G_0 over crosslinker density, for all actin concentration measured, the same increase in elasticity $G_0 \sim r_{ac}^{-1.2}$ is observed with increasing HMM concentration. At high crosslinker densities $r_{ac} < 10$ no further increase of G_0 is observable.

Since the way HMM binds to actin is not known in detail (one headed or two headed) and only a fraction $\theta = \frac{c_{HMM}}{K_d + c_{HMM}}$ is bound to the filament due to the dissociation rate of HMM ($K_d = 0.5 \mu\text{M}$, (Howard 2001)) in rigor state, it is not trivial to relate the amount of crosslinkers to the crosslinking distance L_c . Several groups report a periodicity of the arrowheads (HMM bound to actin) that is equal to the twist repeat of actin every 37 nm (Huxley 1963; Ishikawa et al. 1969; Moore et al. 1970). In comparison to the observation with S1 decorated filaments, where the arrowhead structure results from the binding of S1 to every actin monomer ($\approx 6 \text{ nm}$) (Figure 6-1), the distance between the HMM molecules is assumed to be somewhat larger ($\approx 18 \text{ nm}$) due to sterical hindrances. A rough estimate of the distance between two motors on a filament for a crosslinker density $r_{ac} = 15$ gives values in the order of the meshsize without taking into account that just a fraction might be bound.

For the case the mean crosslinker distance L_c in the network decreases below the mesh size the sol-gel transition should be accompanied by shrinkage of the network or a reorganizing of the network due to bundles. The above observed structure verifies a homogenous, isotropic network without reorganization due to bundle appearance. In addition the normal force F_n stays constant during sol-gel transition Figure 7-4, which

indicates that the network does not shrink. This strengthens the conclusion of a minimal crosslinker distance in the network $L_c \approx \xi \approx L_e$. If crosslinks can just appear at intersection points of the filaments ($L_e \approx \xi \approx L_c$) and the corresponding crosslinking point on another filament is already occupied by other motors (due to the high crosslinker concentration), less crosslinks will be formed. Therefore the elasticity should start to decrease at high crosslinker densities as it is observed for all different actin concentrations.

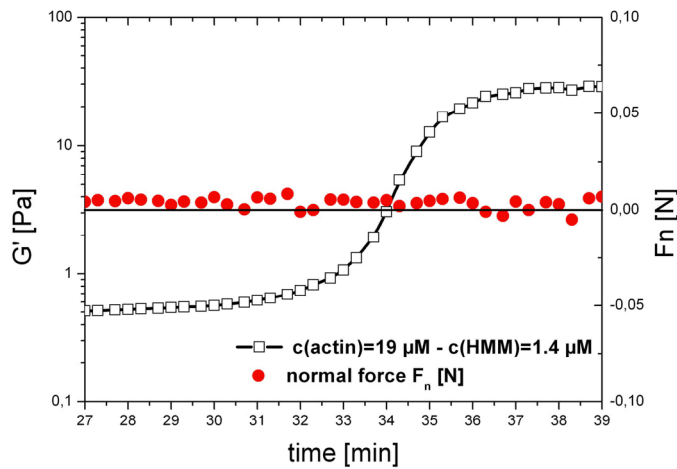


Figure 7-4 To strengthen the assumption that there is no shrinkage of the network during sol-gel transition the normal force F_n was recorded. The graph shows that there is no force applied to the measuring tool because of shrinkage. Since the coupling of the filaments to the sensor head is of great importance and not known in detail, this measurement should be interpreted carefully.

For clarity some important network parameter for the used pure actin concentration are summarized in Table 2.

c_{actin}	ξ	l_e	d
9.5 μM	0.54 μm	1 μm	0.27 μm
14.3 μM	0.44 μm	0.91 μm	0.21 μm
19 μM	0.38 μm	0.86 μm	0.18 μm
23.8 μM	0.34 μm	0.74 μm	0.15 μm

Table 2 Summarization of some important parameter of pure entangled actin networks for the used actin concentrations. The parameters were calculated from formulas mentioned in chapter 3.

7.2.2. Nonlinear Response

Beside the frequency dependence of G'' and G' the stress-strain relation of rigor-HMM/actin networks was probed. Since in a densely crosslinked network was expected, the viscose flow in the network should be neglectable and the appearance of the nonlinear behavior is expected to be at small strains. Therefore a low constant shear rate of $\dot{\gamma} = 0.02s^{-1}$ was applied to have a better resolution of the network response at small deformations. An typical measurement pointing out the parameters of interest is shown in Figure 7-5 (a).

These nonlinear measurements exhibit two distinct regimes. At a continuously increasing strain first a linear regime is observed which corresponds to the linear viscoelastic response of the sample. A further increase of the strain results at $\sigma_{crit}(\gamma_{crit})$ in a nonlinear strain hardening behavior. At a certain maximum strain $\sigma_{max}(\gamma_{max})$ the network weakens strongly due to network rupturing or filament alignment.

An increase in crosslinker density results in several changes of the stress-strain curves (Figure 7-5 (b) and (d)). Whereas the nonlinear network response starts at lower strains with increasing crosslinker concentration, the rupture stress increases around one order of magnitude. The parallel shift of the curves in the linear regime is equivalent to an increasing slope in the lin.-lin. plot (Figure 7-5 (d)).

Because of the elasticity dominates the network response, the plateau modulus can be approximated by Hook's law $G_0 = \delta\sigma/\delta\gamma$ (Eq.3.3) and the increasing slope in Figure 7-5 (d) can be attributed to increasing elasticity. The analysis of the increasing slope with increasing HMM results in the same scaling dependence $G_0 \sim c_{HMM}^{1.2}$ as it is observed from the frequency dependent measurements (Figure 7-3). Interestingly γ_{crit} and γ_{max} stay constant when plotting the nonlinear behavior at a constant crosslinker concentration for different actin concentrations (Figure 7-5(c)). This is a further indication that the changes in the elastic response are dominated by the crosslinker concentration.

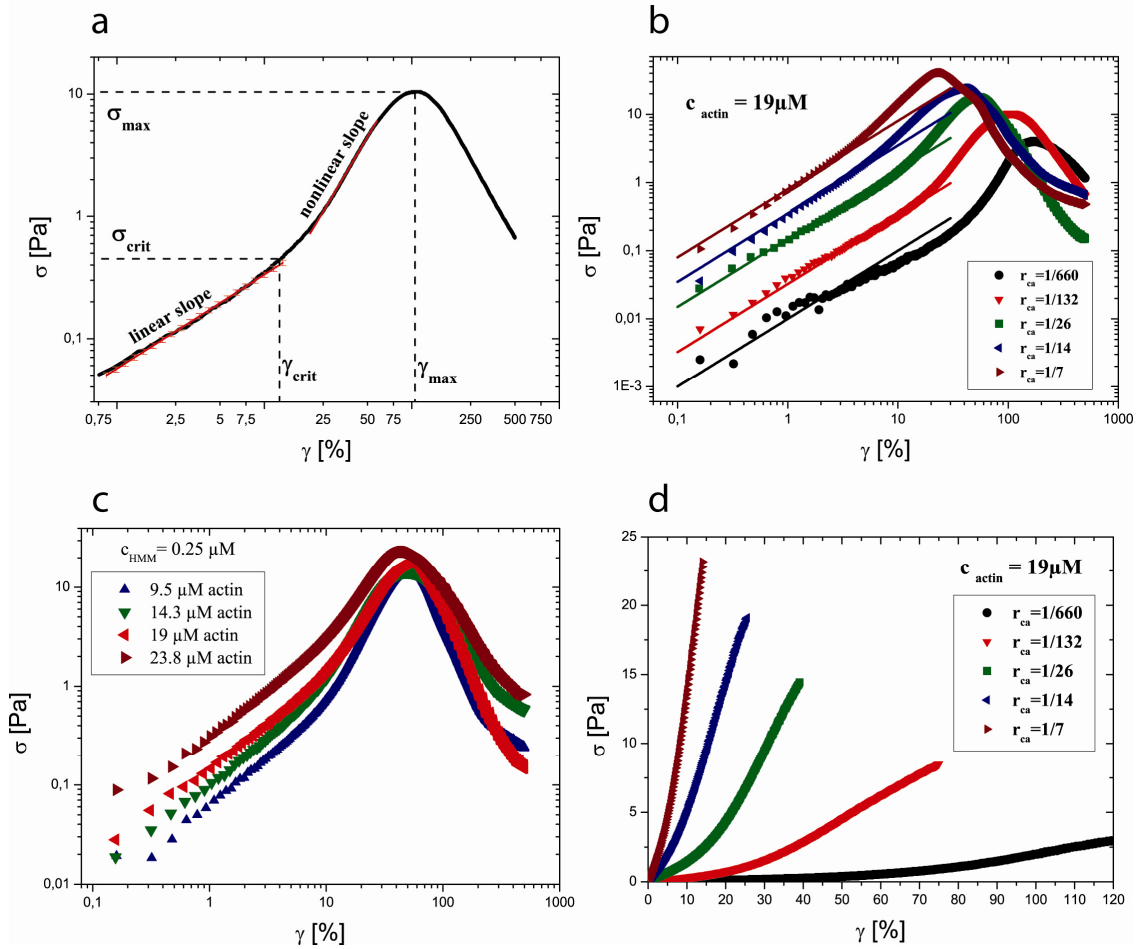


Figure 7-5 The parameter of interest in stress strain measurements are highlighted in (a). (b) and (d) show the nonlinear behavior of an actin network ($c_{actin} = 19 \mu M$) under the influence of increasing concentrations of rigor-HMM. The parallel shifts of the different curves in the log-log plot (b) correspond to the increase in the slope in the linear plot (d) and therefore represents $G_0 = \delta\sigma/\delta\gamma$. (c) For a constant crosslinker concentration the stress strain response behaves similar (γ_{crit} , γ_{max} stays constant) since the elastic properties are dominated by the amount of crosslinkers.

7.2.3. Discussion

Recently, first numerical simulations of the linear response of homogeneous and isotropic 2-dim., crosslinked semiflexible polymer networks under an small applied stress at zero temperature were performed (Head et al. 2003; Wilhelm et al. 2003; Heussinger et al. 2006). These simulations predict distinct regimes were the applied stress is transmitted affine or nonaffine throughout the network. The boundaries of the different regimes depend on the polymer flexibility, the cross linker concentration and filament length, and thus on the crosslinker density L/L_c . At low crosslinker densities a nonaffine network deformation is expected and was already predicted in the past to be

bending dominated (Kroy et al. 1996; Frey et al. 1998). Figure 7-6 shows a simulation of the static mechanical properties of random, semiflexible, crosslinked networks in the linear response regime (Head et al. 2003).

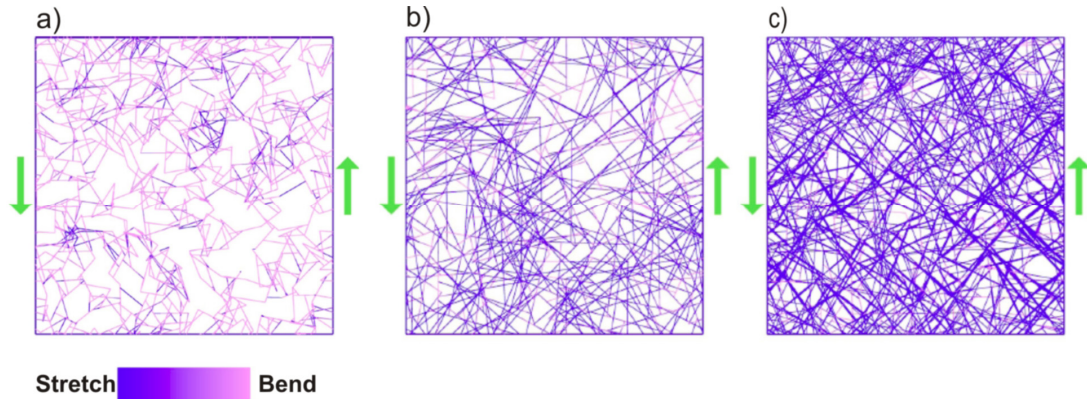


Figure 7-6 false color image of the bending dominated network deformation that is found slightly above the percolation point a) $L/L_c \approx 8,99$. b) $L/L_c \approx 29,09$ and c) $L/L_c \approx 46,77$ illustrates that the system is dominated by stretching and compression modes when the crosslinker density is increased (Head et al. 2003).

The filaments are monodisperse of length L , and uniformly distributed in a 2-dim. shear cell of certain size $W \times W$. Every filament intersection represents a crosslink. L_c is the crosslinker distance and the filaments are allowed to freely rotate around the intersection points.

With increasing crosslinker density there is a continuous phase transition at the rigidity percolation point that is defined at the cross-link density $L/L_c \approx 5.93$. Below this point the network shows no elastic response and the sample behaves like a fluid.

By generating more cross-links, the simulation shows a new regime over which the elastic deformation of the gel is dominated by nonaffine filament bending (Frey et al. 1998). In this regime the network elasticity is difficult to simulate. Generally more degrees of freedom are expected to give rise to values of the plateau modulus G_0 smaller than predicted for an affine network deformation (Mackintosh et al. 1995).

A further increase of the crosslinker density leads to a regime of affine deformation where the end to end distance of the filaments follows the macroscopic shear deformation. In this regime all macroscopic network properties can be scaled down to the response of a single filament. Under this assumption one finds different scaling

relations for the elastic plateau modulus depending on how the stress is transmitted through the sample (Heussinger et al.).

$$G_{affine} = \xi^{-d+2} \cdot \begin{cases} a \cdot \kappa_{\perp} = \frac{\kappa_0}{\xi^3}; (\text{bending dominated}) \Rightarrow G_{affine}^{3\text{-dim.}} \sim c_{actin}^2 \\ b \cdot \kappa_{tension} = \frac{EA}{\xi}; (\text{mechanical stretching}) \Rightarrow G_{affine}^{3\text{-dim.}} \sim c_{actin} \\ c \cdot \kappa_{\parallel} = \frac{\kappa_0 L_p}{\xi^4}; (\text{entropic stretching}) \Rightarrow G_{affine}^{3\text{-dim.}} \sim c_{actin}^{2.5} \end{cases} \quad (\text{Eq.7.4})$$

The details of the network structure only enter the prefactor a , b and c . The weighting of the dimensions $d = 2, 3$ is taken into account by ξ^{-d+2} . ξ has to be interpreted as the unit length scale in the system. In the case of crosslinked actin networks the unit length is the crosslinker distance L_c . E represents the Young modulus and A the cross sectional area of the polymers.

With the simulations mentioned above it was shown that the *bending dominated* regime is observable in regular foams but not in semiflexible, isotropic crosslinked polymer networks (Heussinger et al. 2006). In the affine filament stretching regime one has to differentiate between two longitudinal compliances of different origin. At finite temperature transverse fluctuations can be pulled out and this defines the compliance κ_{\parallel} corresponding to an *entropic filament stretching* (Chapter 3.3.2). In the other case the compliance of the filament is defined by longitudinal changes in the contour length and thus stretching of the filament backbone, like one find for a mechanical Hookean spring, defining the stretching modulus $\kappa_{tension}$. Since values in GPa range were measured for the tensional Young modulus E of actin (Howard 2001) it is unlikely that the *mechanical stretching* dominated case can be observed in experiments: the crosslinker will probably unbind before stretching the filament backbone is possible.

However, experimental findings of the elastic modulus might result from a combination of all these deformation modes where one mode might dominate. The affine modulus can be described by the following equation (Heussinger et al.):

$$G_{affine}^{-1} = \xi^{d-2} \left(a \cdot \kappa_{\perp}^{-1} + b \cdot \kappa_{tension}^{-1} + c \cdot \kappa_{\parallel}^{-1} \right) \quad (\text{Eq.7.5})$$

All measurements of the rigor-HMM/actin networks indicate that entropic stretching dominates the network response, where thermal fluctuations results in nonlinear entropic elasticity as it is predicted by the WLC-model. Under this assumption and taking into account that $L_c \geq \xi$, the linear response of the plateau modulus should scale as follows (Mackintosh et al. 1995):

$$G_0 \sim \frac{\kappa_0^2}{k_B T \xi^2 L_c^3}. \quad (\text{Eq.7.6})$$

As crosslinks appear only at intersection points of the actin filaments the crosslinker distance can be rewritten as

$$L_c \cong l_{c(HMM)} L_e \sim l_{c(HMM)} \left(\frac{\kappa_0}{k_B T} \right)^{1/5} c_{actin}^{-2/5}. \quad (\text{Eq.7.7})$$

$l_{c(HMM)}$ depends only on the crosslinker concentration and is a coefficient of the minimal crosslinker distance $L_c \approx L_e$; ($l_{c(HMM)} > 1$).

This assumptions result in following scaling behavior of G_0

$$G_0 \sim \frac{\kappa_0^{7/5}}{(k_B T)^{2/5}} \cdot l_{c(HMM)}^{-3} c_{actin}^{2.2}. \quad (\text{Eq.7.8})$$

When normalizing the obtained data of the plateau modulus to the dependence of the actin concentration $c_{actin}^{2.2}$, all data points collapse on each other (Figure 7-7 (a)).

Therefore the scaling behavior

$$\frac{G_0}{c_{actin}^{2.2}} \sim \frac{\kappa_0^{7/5}}{(k_B T)^{2/5}} l_{c(HMM)}^{-3} \sim c_{HMM}^{1.2}, \quad (\text{Eq.7.9})$$

can just be attributed to the distance between crosslinker at a certain HMM concentration. In the framework of this model the elastic behavior of a single actin filament is determined by the thermally excited bending fluctuations where the mean square amplitude of these fluctuations $\langle u^2 \rangle$ strongly depends on the length between crosslinks as $\langle u^2 \rangle = k_B T L_c^3 / \kappa_0$ (Mackintosh et al. 1995; Keller et al. 2003) and small changes in κ_0 are neglectable (Loïc Le Goff 2002). For composite rigor-HMM/actin

networks also a prefactor >90 is observable which is not observed for pure entangled networks and predicted in the used model.

As already mentioned in chapter 5.3.2, a strong prediction of this model is that with increasing crosslinker density the onset of the non linear response is shifted to smaller deformations. Since in the expansion of the extension to applied tension only linear terms are accounted for and nonlinear terms are neglected, it is assumed that the maximum strain is related to the onset of the nonlinear regime and therefore allows the prediction of γ_{crit} (Mackintosh et al. 1995; Shin et al. 2004):

$$\gamma_{crit} \sim \frac{k_B T L_c}{\kappa_0} \sim \left(\frac{k_B T}{\kappa_0} \right)^{4/5} l_{c(HMM)} c_{actin}^{-2/5}. \quad (\text{Eq.7.10})$$

The analysis of γ_{crit} and σ_{crit} in the stress-strain curves results in a distinct scaling of the critical strain and stress with the crosslinker concentration (Figure 7-7 (c) and (d))

$\gamma_{crit} \sim c_{HMM}^{-0.4}$ and $\sigma_{crit} \sim c_{HMM}^{0.8}$. Inserting the observed scaling in Hook's law $G_0 \sim \sigma_{crit} / \gamma_{crit} \sim c_{HMM}^{0.8} / c_{HMM}^{-0.4} \sim c_{HMM}^{1.2}$ results in the same scaling of G_0 with the HMM concentration as observed from the frequency response of the sample.

The mechanical response of rigor-HMM/actin networks shows a strong dependency on the distance between crosslinkers. Measurements can be explained by a model that predicts thermal filament fluctuations as the origin of elasticity. In contradiction to former applied model stay the sharp edges seen in the fluorescence images. But when assuming that just two motors crosslink every filament (which is already the case at very low crosslinker concentrations) the mechanical response should stay constant with increasing HMM concentration since all long wave modes above $0.7 \mu\text{m}$ are already pulled out. This is not observed experimentally and therefore the influence of sharp edges to the elastic response may be weak.

When normalizing the obtained data of γ_{crit} to the dependence of the actin concentration $c_{actin}^{-2/5}$ (Eq.7.10), the data points again collapse on each other (Figure 7-7 (c)). For the case $l_{c(HMM)} = 1$ (at high crosslinker concentration), the crosslinks appear at the distance of the entanglement length and $L_c = L_e$ (Eq.7.7). This strengthens again the fact that

mechanical response of rigor-HMM/actin networks is just determined by the distance between crosslinker L_c .

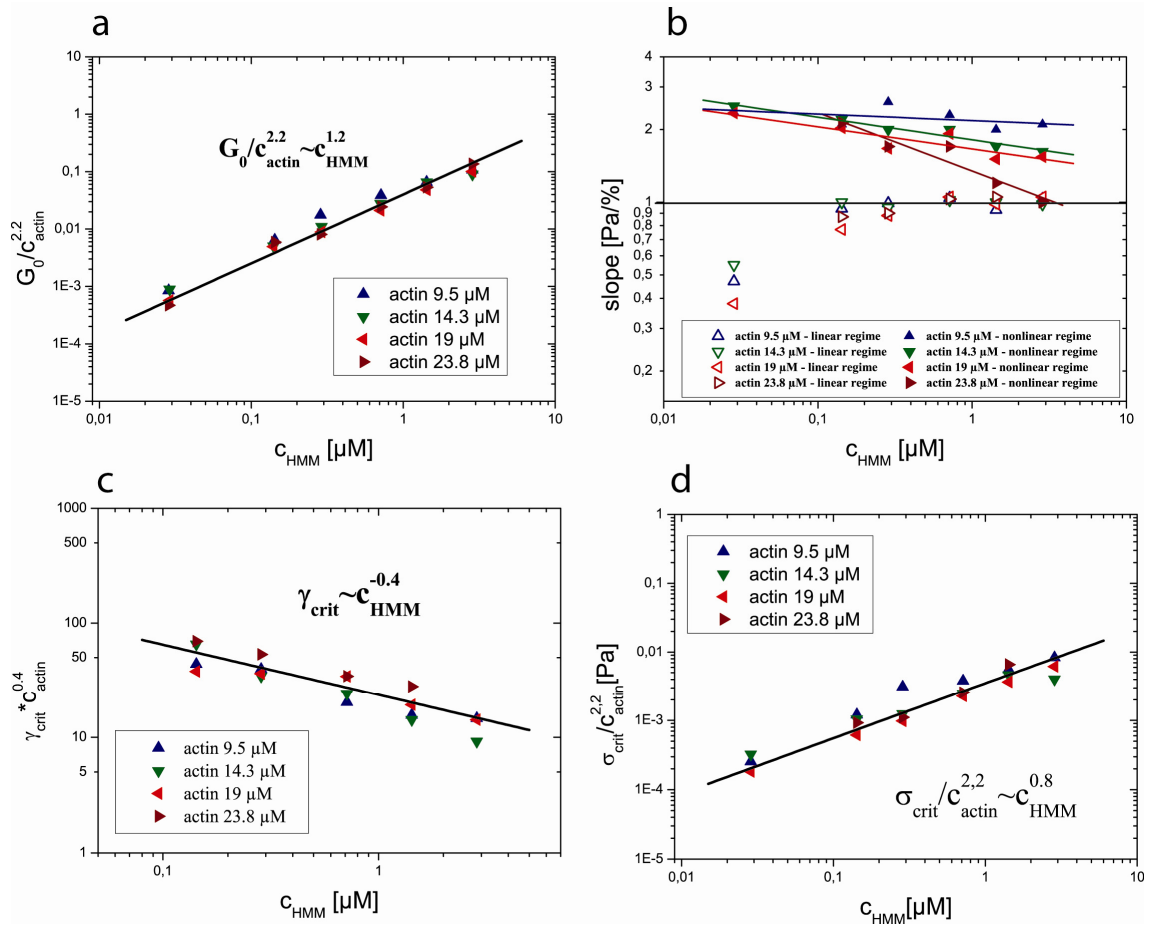


Figure 7-7 If the data of the plateau modulus are normalized to the actin dependence that is predicted by the used model all data points collapse on each other as presented in (a). The analysis of the slope in the linear regime (open symbols) and in the nonlinear regime (full symbols) reveals several features: first there is a viscous flow visible for low HMM concentration. Thus the scaling in the log-log plot represents a nonlinear response. For higher HMM concentration the slope of the first regime stays constant linear. Next in the second nonlinear regime a decreasing scaling exponent with increasing motor concentration is observable. For the highest crosslinker and actin concentrations the nonlinear regime disappears completely. This might indicate that all fluctuations of the actin filaments are vanished and the system response is dominated by bending modes. The combination of the scaling of γ_{crit} and σ_{crit} ((c) and (d)) with the HMM concentration determined by the stress strain measurements $G_0 \sim \sigma_{crit} / \gamma_{crit} \sim c_{HMM}^{0.8} / c_{HMM}^{-0.4} \sim c_{HMM}^{1.2}$, reveals the same scaling as was determined from the plateau modulus of the frequency behavior observed in (a).

For a better understanding of the maximal acquirable linear deformation γ_c one has to consider the total excess length $L_\infty - L_0$ of the segment between two crosslinks, where L_∞ is the averaged contour length and L_0 is the corresponding end-to-end distance in equilibrium without applied external force. The used model predicts an averaged end-to-end distance L to linear order with applied stress

$$L \approx L_\infty - \underbrace{\frac{L^2}{6L_p}}_{\delta L_{\text{equilibrium}}} + \underbrace{\frac{L^4}{k_B T L_p^2}}_{\delta L(\sigma)} \sigma. \quad (\text{Eq.7.11})$$

Equation 7.11 can be used to calculate the total excess length $L_\infty - L_0$

$$L - \underbrace{\frac{L^4}{k_B T L_p^2}}_{L_0} \sigma \approx L_\infty - \underbrace{\frac{L^2}{6L_p}}_{L_0} \Rightarrow L_\infty - L_0 \approx \frac{L^2}{6L_p}. \quad (\text{Eq.7.12})$$

Under the assumption of maximal linear deformation Eq.7.12 can be rewritten

$$L_{\text{max}} - L_0 = \delta L_{\text{max}} = \frac{L_{\text{max}}^2}{6L_p} \sim \gamma_{\text{crit}} L_{\text{max}} \quad (\text{Eq.7.13})$$

$$\gamma_{\text{crit}} \sim \frac{k_B T L_c}{\kappa_0} \Rightarrow L_c \sim \gamma_{\text{crit}} L_p$$

Using Eq.7.13 the crosslinker distance L_c (Figure 7-8), the accessible deflection length δL_{max} , the contour length $L_\infty(L_c)$ and the crosslinking coefficient $l_{c(HMM)}$ can be calculated from the data of γ_{crit} . Since for the highest HMM concentration a crosslinker distance of the size of the entanglement length (Table 2) is expected and only a relative scaling is predicted the calculated values have to be normalized to get the absolute crosslinker distance L_c . The normalization factor is given by a and ranges between 0.1-0.3 for the different actin concentrations. Rescaling the data with a factor a might be necessary as e.g. the additional flexibility of the crosslinker is not accounted for in the model. Additionally the small differences between the crosslinker distances for different actin concentration and uncertainties in the determination of γ_{crit} only allow the dependency on the actin concentration to be roughly determined.

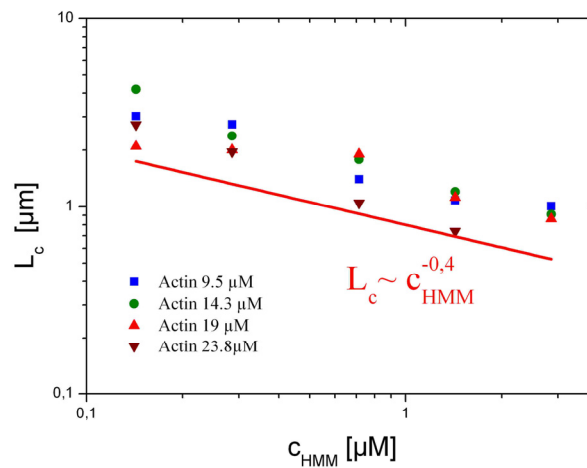


Figure 7-8 The graph shows the change in crosslinking length L_c calculated from Eq.7.12. over the used crosslinker concentration. Data is shown for different actin concentrations. The small differences between the crosslinker distances for different actin concentration and uncertainties in the determination of γ_{crit} give rise to a large error and the dependency on actin concentration can only be roughly determined.

The analysis of the slope in the linear regime shows for low crosslinker concentration below 0.1 μM a nonlinear behavior (Figure 7-7 (b)) that has to be attributed to the viscose flow as it was shown in detail in chapter 5.3.2..

By analyzing the slope of the nonlinear regime (Figure 7-7 (b)), a clear decrease with increasing actin and HMM concentration is observed (Figure 7-9 (a) and (b)). For the highest actin and crosslinker concentrations the nonlinear behavior disappears completely until only a linear dependence of the stress on the applied strain is observed (Figure 7-9 (b)). These measurements do not agree with the model applied above, where thermal filament fluctuations are supposed to be origin of elasticity. The differential elastic modulus K' over the applied deformation can be obtained after smoothing and deviating the stress-strain curves. Figure 7-9 (c) and (d) show clearly the decreasing slope in the nonlinear regime and contradict recent theories of a general scaling in the nonlinear behavior of semiflexible polymer networks (Gardel et al. 2004; Storm et al. 2005). The analysis of the scaling exponents of Figure 7-9 (c) and (d) reveals the full range between 0 and 2. Beside this the dependence of K' in the linear regime scales with the HMM concentration in the same way as it was observed before (Figure 7-10 (a)).

One possible explanation might be that the network is at such high crosslinker densities dominated by bending of the segments between crosslinks as there are no more fluctuations to stretch out. Since in the experiments shown only the crosslinker density is changed, it seems that for 23.8 μM actin with an entanglement length of $\approx 0.7 \mu\text{m}$ all measurable thermal fluctuations are already stretched out and the nonlinear network response is solid like. Under an assumption of a continuous transition from entropic stretching to bending of the filaments, the predicted scaling of the plateau modulus G_0 with the actin concentration should change from an exponent of 2.2 to 2. This is almost indistinguishable in the data set and more measurements at such high densities are still necessary to clarify this.

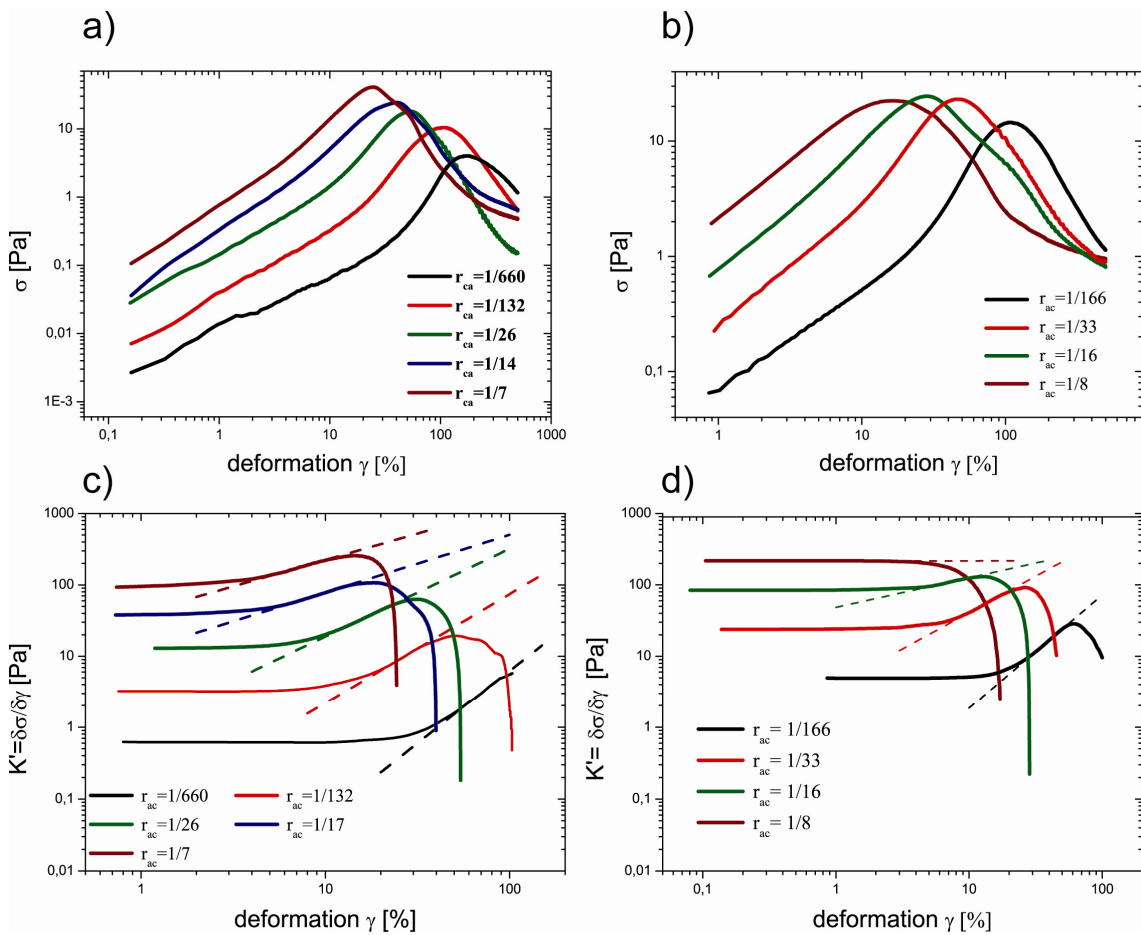


Figure 7-9 By smoothing and deviating the stress-strain curves (a) and (b) it is possible to obtain the differential elastic modulus K' over the applied deformation (c) and (d) respectively. The differential elastic modulus K' clearly shows a disappearing nonlinear response contradicts the existence of a general scaling law.

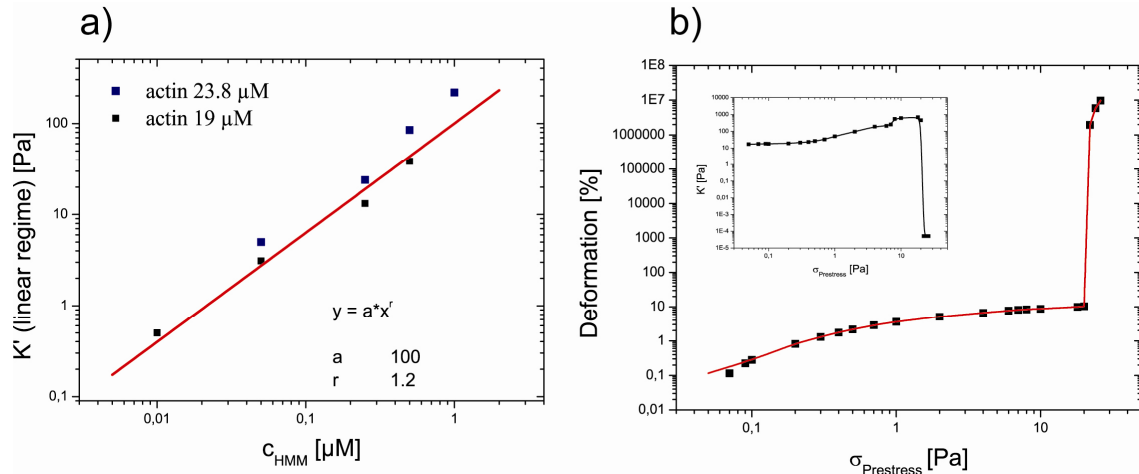


Figure 7-10 As a check, the same scaling behavior of the linear response is observed in the deviations of the stress-strain curves (left handed). To proof that the network really ruptures, a prestress measurement was performed (right handed, actin 9.5 μM and $r_{ac} = 40$).

Since for both actin concentration in Figure 7-9 (c) and (d), the yield stress at highest HMM concentration is nearly the same another possible explanation appear. The disappearance of the nonlinear regime might be attributed to the maximum elasticity the network can withstand and therefore the network rearrangements due to rupturing may influence the nonlinear behavior and even dominate the nonlinear response. From stress-strain measurements it is not observable if the network ruptures because of the continuous increase of the deformation at a constant speed. To observe if the network ruptures, prestress experiments were done. By integration of $K'(\sigma_{\text{prestress}})$ one obtain the deformation over the applied stress (Figure 7-10, left hand). This measurement confirms what can be seen by eye, the measure head rotates freely and the deformation jumps at the yield stress to enormous values.

Although the used model fits the data quite nicely one has to think more about the real applicability in the case of such complex networks. Since the network is densely crosslinked and the actin segments between two crosslinks ($L_c \approx 0.7\text{-}5 \mu\text{m}$) have to be very stiff, concerning the persistence length $L_p = 17 \mu\text{m}$, it is not obvious that thermal fluctuations can be stretched out. There are still open questions and a full explanation is still missing. Further investigation is therefore necessary.

8. Active-HMM/Actin Networks (active state)

8.1. Structure of Active-HMM/Actin Networks

The structure of the composite active-HMM/actin networks was observed by fluorescence microscopy (Figure 8-1 (a), (c)) and TEM (Figure 8-1 (b), (d)). Both measurements indicate that the addition of HMM under ATP excess is not visibly changing the network structure. Actin filaments are organized as isotropically disordered networks like the ones found in pure actin samples.

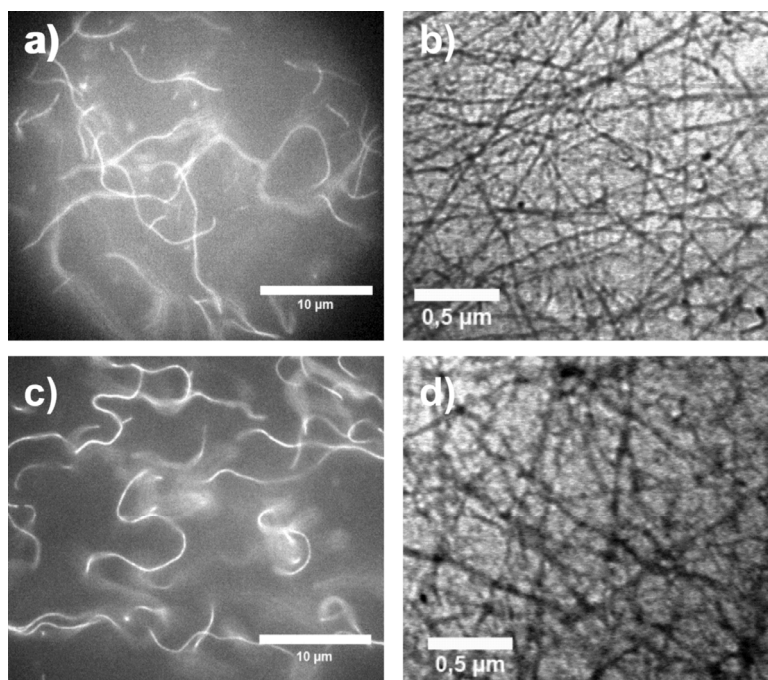


Figure 8-1 Picture a) represent a fluorescence image of a pure entangled actin sample (actin concentration $23.4\mu\text{M}$, 1 reporter-filament/ 500 unlabeled filaments). b) Electron microscopy pictures of a pure entangled actin sample (actin concentration $9.5\mu\text{M}$). c) Fluorescence image of a composite active-HMM/actin sample ($r_{ac} = 5$, 1 reporter-filament/ 500 unlabeled filaments). Both fluorescence images represent an average of 10 pictures. The observable network structure has no significant differences between pure actin and composite active-HMM/actin.

8.2. Rheology of Active-HMM/Actin Networks

In contrast to the similarity in network structure a crucial change in the viscoelastic moduli is observed between pure actin network and an active-HMM/actin network. Macrorheological experiments show a dependence of the moduli G' and G'' on the amount of added active HMM (Figure 8-2). In these experiments the actin filament length was adjusted to $21\ \mu\text{m}$ in a $9.5\ \mu\text{M}$ actin solution. For high HMM concentrations ($r_{ac} < 40$) the moduli decrease with increasing HMM concentration and the overall shape of the frequency dependence of G' and G'' is changed. Active HMM molecules are able to reduce the plateau modulus G_0 around 70% of the value measured for pure entangled actin networks (Figure 8-4). The disengagement time τ_d decreases from 10000 seconds (Isambert et al. 1996) to ~ 100 s which points at a fluidization of the entangled actin due to the addition of active HMM molecules. Interestingly the entanglement time τ_e increases (Figure 8-3) with increasing HMM concentration. For highest HMM concentration $r_{ac} = 5$ the resolution limit of the rheometers is almost reached ($\approx 0,01$ Pa) and therefore the frequency dependence of the viscoelastic moduli may be somewhat off from the expected value.

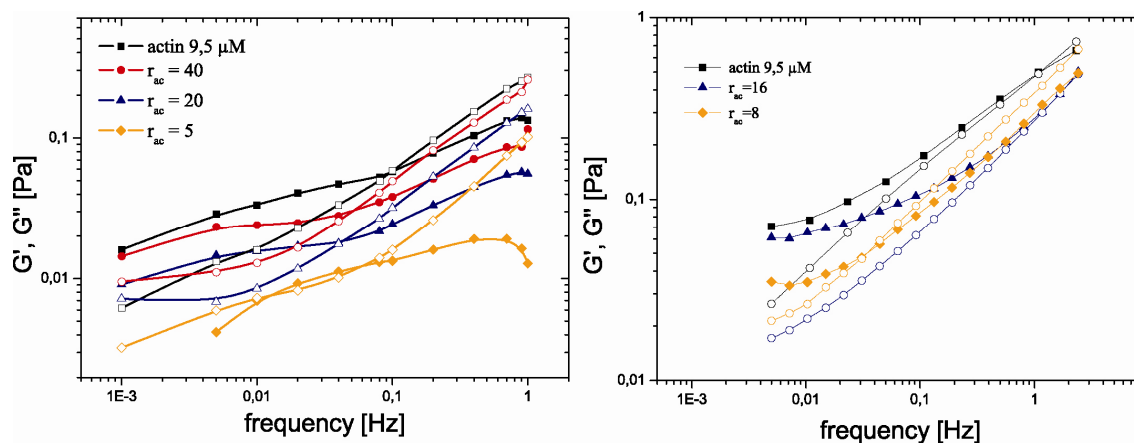


Figure 8-2 Left graph represents the frequency dependence of G' and G'' for an actin network without and with addition of different motor concentration measured in the "Rotating Disc" setup. Right graph shows the same experiment measured in the commercial rheometer MCR301.

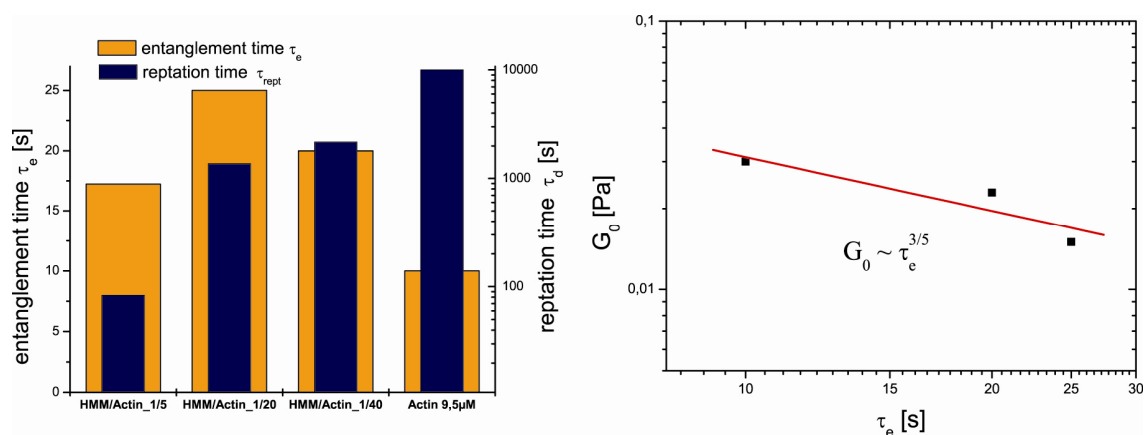


Figure 8-3 Concomitant with the decrease of the plateau modulus G_0 the entanglement time increases and the reptation time decreases with increasing HMM concentration (left graph). Data were analyzed from the left graph of Figure 8-2. Due to fluctuation amplitudes stretched out by molecular motors the entanglement length increases and the entanglement time has to scale with $G_0 \sim \tau_e^{3/5}$.

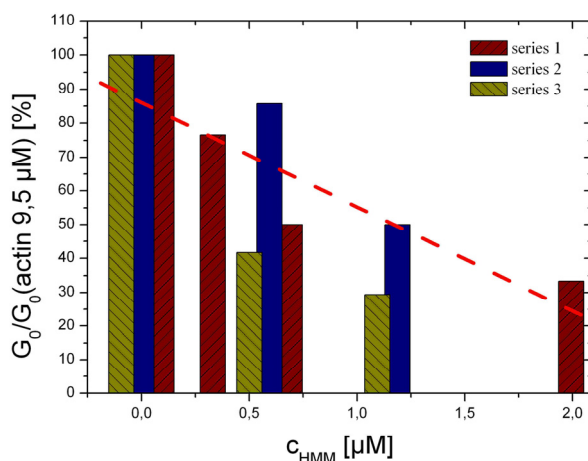


Figure 8-4 The graph shows the decrease of the plateau modulus in dependence of the motor concentration for three different series. The data are normalized on the plateau modulus of the pure actin measurement.

Recently similar findings were reported for measurements with composite active-myosin II/actin networks (Humphrey et al. 2002). In excess of ATP these measurements showed a decrease of the elastic modulus to $40 \pm 10\%$ of G' for actin solutions without myosin II. The disengagement time was reduced to 8 ± 0.4 s. Despite the fluid like behavior the existence of a remnant elastic plateau in all experiments was attributed to a small, unavoidable amount of inactive myosin heads.

Since a small amount of dead myosin may be sufficient to cause an elastic response and inhibit active fluidization, special care was taken to the purity of the HMM solution used in the present study. To ensure to work with highly pure and active molecular motors the activity of the HMM preparation was compared before and after additional purification. To purify the HMM a already polymerized actin/HMM solution were centrifuged under high ATP condition 2 h at 4°C and 38.000 rpm. The supernatant were used for the activity test in an UV/VIS-spectrometer. The reaction velocity is determined in a lactate dehydrogenase coupled assay system (Figure 8-5) by measuring the decrease in absorbance at 340 nm resulting from the oxidation of NADH (Figure 8-6). The decay rate of absorption reveals the ATPase activity of myosin molecules. These tests let assume that the motor activity is not affected by the purification and only a marginal fraction of dead motors is present in the preparation. Therefore there is no need to get rid of impurities of dead motors.

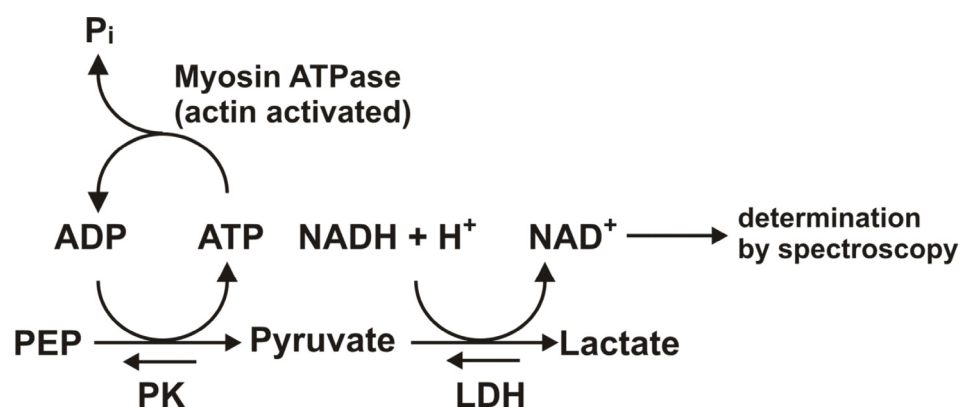


Figure 8-5 A brief scheme of reaction involved in NADH coupled ATPase assay: One ATP molecule is hydrolyzed by HMM generating an ADP molecule. The ADP generated is converted back into ATP by the action of pyruvate kinase using PEP as a substrate. Subsequently, NADH is oxidized into NAD⁺ by Pyruvate catalyzed by L-lactic-dehydrogenase. The reaction is monitored at 340 nm by spectroscopy (refer to the absorption curve of NADH and NAD⁺). The decay rate of absorption reveals the ATPase activity of myosin molecules.

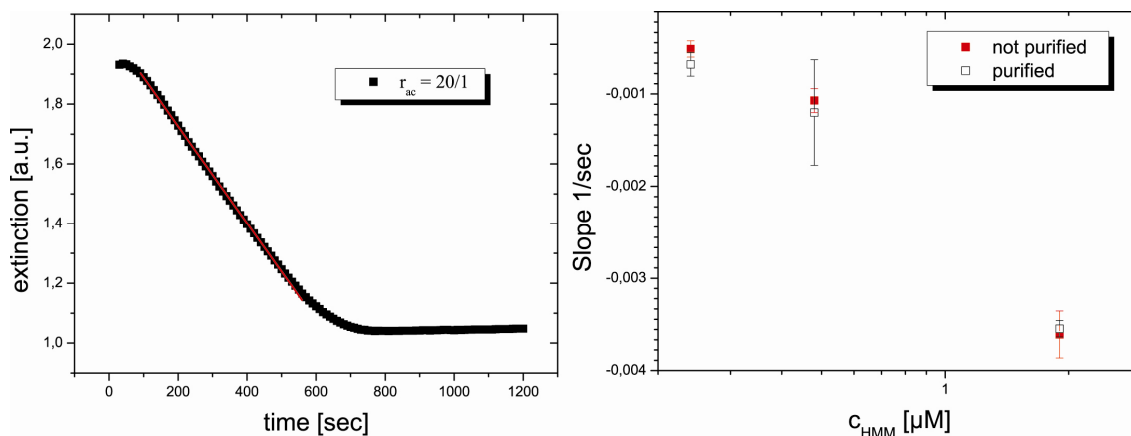


Figure 8-6 The left graph represent a measure for the decreasing ATP concentration in the sample measured by UV/VIS-spectrometer. The slope reveals a value for the ATPase rate of the molecular motors (actin 9.5μ M). The right graph shows the comparison of the ATPase rate between purified and not purified HMM at different motor concentration (Error bars represent three measurements).

To ensure, that the effect of fluidization is not caused by a delayed or an affected polymerization, the polymerization was recorded for 3 hours with and without HMM. In both cases a plateau was reached within the first hour and no significant changes were observed in the next two (Figure 8-7). This strengthens the idea that active molecular motors are able to change the network dynamics just by the execution of the power stroke when they are attached to the filament. Stress-strain measurements reveal a disappearance of the nonlinear regime that is accompanied by a decreasing slope in the linear regime and a reduced yield stress at the same deformation.

In contrast to experiments with myosin II microfilaments, HMM is a non processive motor that releases the filament after the powerstroke. Therefore a directed motion of filaments that was assumed to be the reason for the reduction of reptation time and elastic strength in the composite active-myosin II/actin networks is more complicated to explain in the active-HMM/actin system. It may only work if short HMM tails are subject to viscous drag during the powerstroke or several motors are simultaneously picking on the filaments. Here it is important to mention that due to the low duty ratio of myosin II ($r = 0.02$, chapter 2.3) the probability of the simultaneously binding of both heads to different actin filaments is very low $P_{both} \approx r^2 \leq 0.02^2$ and therefore unlikely for several motors in chorus.

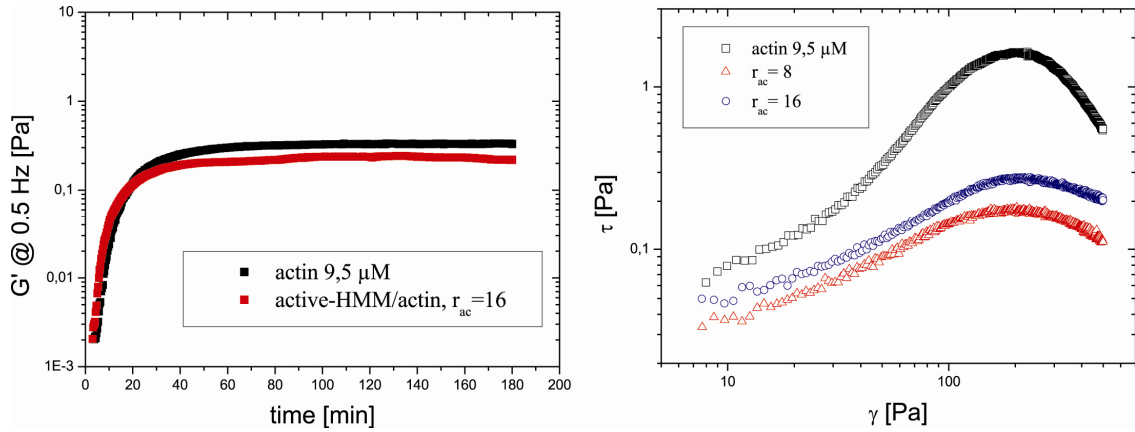


Figure 8-7 On the left hand the graph shows the elastic modulus G' recorded at a frequency of 0.5 Hz over 3 hours of polymerization for a pure entangled actin network and an active-HMM/actin network ($r_{ac}=16$) respectively. Both curves exhibit a plateau that is constant during 3 hours. On the right hand stress-strain curves show the disappearing of the nonlinear behavior with increasing motor concentration corresponding to a decrease in the fluctuation amplitude.

The drag force generated by one single motor executing the working stroke of $\delta = 5$ nm can be estimated by assuming a cylindrical shape of the HMM tail of length $L \approx 50$ nm and diameter $2r = 2$ nm. This results in a drag coefficient (Wendt et al. 2001) (Howard 2001)

$$\gamma_{\perp} = \frac{4\pi\eta L}{\ln(L/2r) + 0.84} \approx 1 \cdot 10^{-10} \frac{N}{m} \quad (\text{Eq.8.1})$$

in water of $\eta = 1$ mPa. The drag force of a single HMM motor against the water viscosity can be calculated using the drag time τ_{drag} and the working distance δ in following equation (Howard 2001),

$$F = \gamma_{\perp} v = \gamma_{\perp} \frac{\delta}{\tau_{drag}} \approx 0.4 \cdot 10^{-15} \frac{N}{s} \quad (\text{Eq.8.2})$$

Thus in an actin solution with an averaged filament length of 21 μ m containing HMM in a ratio $r_{ac} < 40$, the directed viscous drag of thousands of motors per filament are able to generate an overall force to the filament in a Pico Newton range.

There are two possible explanations that describe these experimental findings:

1. The HMM induced fluidization may be explained by a diffusive directed motion of the actin filaments within their tube (Humphrey et al. 2002). This possibly will result from increasing longitudinal fluctuations along the filament contour activated by the actomyosin interaction. This ought to give rise to a higher effective temperature in the sample and lead to different scaling behaviors in the different time regimes as it was predicted by Liverpool (Liverpool et al. 2001). A slight increase in the entanglement time τ_e is predicted as also observed in experiments with active-HMM/actin networks. Beside this the plateau modulus of active networks with long polymers ($L_p < L$) is predicted to stay equal to that of pure entangled networks which stays in strong contrast to the observations. The experimental observed decrease in the disengagement time is in accordance with the prediction of the model suggested by Liverpool (Figure 8-3, left graph). But this enforced reptation should lead to a clearly visible motion of filaments within ~ 100 s over a distance of the contour length. Recorded movies of fluorescently labeled reporter filaments (Figure 8-1) do not exhibit any directed motion even at high ratios ($r_{ac} = 5$) under ATP excess. Therefore the fluidization of active-HMM/actin networks can not be explained alone by this theory.

2. Another explanation might be an increasing bending modulus that results from the continuously actomyosin interaction by suppressing long transversal relaxation modes of the filaments. This effect can be visualized by picturing a motor picking on the actin filament during the powerstroke against the water viscosity. The Euler force that is needed to cancel out thermal bending fluctuations down to the length scale of the entanglement length $L_e \approx 1\mu m$ can be calculated to (Howard 2001):

$$F_c(L = 1\mu m) = \pi^2 \frac{EI}{L^2} = \pi^2 k_B T \frac{L_p}{L^2} \approx 0.7 pN. \quad (\text{Eq.8.3})$$

However, 0.7 pN can be attributed to thousands of active motors doing their viscous drag (which is satisfied at these high ratios) but also one head of the molecular motor is able to generate force around 1.5 pN when the other head is connected to another filament at the same time. Since the probability of the simultaneously binding of both heads to different actin filaments is very low $P_{both} \approx r^2 \leq 0.02^2$ it is unlikely but possible.

All in all this is a highly dynamically process in non-equilibrium by the reason that the attached time of the motor head under ATP access is below 1ms.

As a result of the suppressed long transversal relaxation modes the resistance to thermal bending, which is described by the persistence length L_p , behaves stiffer which corresponds to an increase of the filament bending modulus (therefore also L_p increases).

An increased persistence length entails several changes in the viscoelastic behavior of the network: The typical distance between two collision points within the tube, the entanglement length $L_e \approx d^{2/3} \cdot L_p^{1/3}$ increases when the polymer concentration and thus the tube diameter d is assumed to be constant. Consequently the density of entanglement points decreases which might explain the reduced yield force and the disappearance of the nonlinear behavior. Moreover the slightly rising entanglement time can be also explained by the increase of the bending rigidity $\tau_{ent} \approx \frac{\zeta_{\perp}}{k_B T} \cdot L_p^{1/3} \cdot d^{8/3}$. When d is assumed to be constant the plateau modulus has to decrease with increasing persistence length L_p and entanglement time

$$G_0^{entangled} \approx k_B T \cdot L_p^{-1/5} c_{actin}^{7/5} \sim \tau_e^{-3/5}.$$

This trend is observed in the measurement shown in the right graph of Figure 8-3. It is important to mention that the shape of the frequency response is poorly reproducible in different experiments. Due to this the quantitative analysis of the frequency behavior is just shown for one single measurement series. In further measurements the decrease of the plateau modulus G_0 was analyzed as shown in the right graph of Figure 8-2. The decrease in elasticity is clearly visible and shown for three experimental series in that were measured in both macrorheometers.

As confirmed in measurements showed before, the purity of HMM and therefore dead motors cannot be responsible for the difficulties of repeatability. But for different actin preparations this effect was poorly reproducible. Recent experiments suggest that these active measurements are highly sensitive to the quality of the actin since the decrease in the elastic moduli is just attributed to the mechanical behavior of the actin filaments.

But a more thorough analysis of the different behavior and comparison of different measurements are still necessary.

A prove for the theory of reduced thermal fluctuations due to the unidirectional power stroke of the active HMM motors might be the reduction of the filament length and thus pre-diminish the thermal fluctuations to a minimum. The effect of fluidization should disappear. Indeed the fluidization is not observable anymore but surprisingly macrorheological measurements of active networks with filament length of $10\ \mu\text{m}$ result in an increased plateau modulus. These results are in accordance to measurements with the magnetic tweezer setup which were thought to be contrary to the determination of the fluidization. Since the accessible wave modes of the magnetic tweezer are in the order of the colloidal probes ($4.5\ \mu\text{m}$) all long wave modes are inaccessible. This may be a further prove for the theory of reduced thermal fluctuations due to the unidirectional power stroke of the active HMM motors. For the increased elasticity in the plateau regime an explanation is still missing.

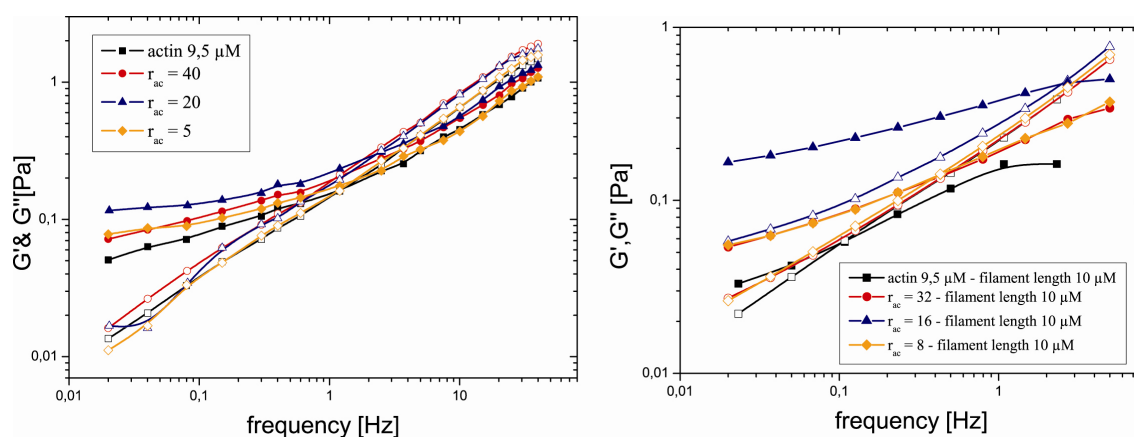


Figure 8-8 Both graphs represent the frequency behavior of the viscoelastic moduli G' and G'' for an actin network without and with addition of different motor concentrations. Left handed graph shows curves measured in the magnetic tweezer setup with an adjusted actin filament length of $21\ \mu\text{m}$. Right handed graph represents the macrorheological measurements where actin filaments had a mean length of $10\ \mu\text{m}$. Both measurement series exhibit the same behavior with increasing motor concentration.

9. Conclusion

Similar to *in vivo* observed actin network structures, *in vitro* actin networks exhibit several distinct structural appearances, ranging from pure bundled networks over extremely heterogeneous composite bundled and crosslinked networks to homogenous isotropic crosslinked networks. In cells, these structural changes are outstandingly controlled by a wide range of actin binding proteins. By a bottom up strategy composite *in vitro* F-actin networks can be used to mimic cells on a strongly simplified way (Wagner et al. 2005 ; Claessens et al. 2006; Tharmann et al. 2006).

Despite this, important effects can be investigated in simplified system as *in vitro* F-actin networks and the results contribute as piece of a puzzle to the over-all picture of the cell. Thus, the observed viscoelastic behavior of *in vitro* actin networks in the presence of polyethylene glycol (chapter 5) suggests, that depletion forces play a crucial role as effective crosslinkers *in vivo*, altering the network structure and mechanics dramatically. Therefore, in cells where about 20%-40% of the volume consists of globular proteins depletion forces will be strong enough to severely alter the cytoskeletal structure and mechanics (Kulp et al. 1995). In the crowded environment of cells low concentrations of specific crosslinkers might thus be acting in an already pre-arranged network structuring and thereby fortifying it. For further insight into the function of specific crosslinkers in *in vitro* systems it will be important to consider specific crosslinkers and depletion forces simultaneously.

The theoretical basis to describe complex *in vitro* polymerized actin networks is on the way. Due to huge efforts of theoreticians one is able to predict different regimes in the mechanical behavior for 2.-dim. isotropic crosslinked, semiflexible polymer networks (Head et al. 2003; Wilhelm et al. 2003; Onck et al. 2005; Heussinger et al. 2006). To fortify these upcoming models, unambiguous experimental data of the mechanical behavior of distinct network structures are necessary. Since most of the biologically relevant specific crosslinkers cause in *in vitro* F-actin networks extremely complex composite bundle and crosslinked network structures the structure and rheology data is intricate to interpret. Therefore, it is highly welcome that the sub fragment HMM of the molecular motor myosin II forms homogenous, isotropic crosslinked networks under

ATP depletion. This makes it easier to ascribe the linear mechanical response of rigor-HMM/actin networks to an already existing theoretical model (Mackintosh et al. 1995). This model predicts an entropic origin of the network elasticity understandable by the properties of a single filament. Since one would expect filaments to behave as stiff rods at very small crosslinker distances, it is convincingly shown that the existence of a minimal crosslinker distance of the order of the intersection point still enables thermal fluctuations below L_c to contribute to the network elasticity. By the fact that ATP is no more available in the sample volume the crosslinker properties of HMM are activated after complete polymerization of the actin filaments. This may be the reason for the limited crosslinker distance and also the structural appearance of rigor-HMM/actin networks. This challenges the preparation techniques of *in vitro* actin networks in the presence of ABPs. Since *in vitro* actin polymerization is normally done in presence of ABPs (e.g. α -actinin, Filamin, Fascin, Cortexilin and so on) the emerging structure may be strongly influenced by the presence of ABPs, whereas the polymerization kinetics are not necessarily changed. It is an interesting question if *in vitro* there is a difference between activating the crosslinker properties before and after polymerization of the actin filaments and if cells make use of the possibility to activate/deactivate crosslinkers or to provide locally activated crosslinkers to achieve distinct network structures e.g. bundles.

However, on the one hand Peg6K/actin networks form a pure bundle network phase and on the other hand rigor-HMM/actin networks display a homogenous, isotropic crosslinked actin network. Both unambiguous datasets can be consulted to obtain a better understanding for the more complex case of composite bundle and crosslinked networks and to get more insight into the strong influence of crosslinker geometry to the network structure and mechanical response (Wagner 2003; Wagner et al. 2005).

In contrast to the crosslinking properties of HMM, under ATP access the motor activity can drive F-actin networks in a highly non equilibrium state. In this active state the rheological response exhibits a significant fluidization of the networks. Given that the chemical energy stored in ATP is converted by the molecular motor into mechanical force in the bound state, a change in single filament dynamics is responsible for this stimulating effect. Since fast changes of the cell shape are necessary this raises the question, if motor activity is also used to soften the cytoskeleton on the length scale of a

cell or if this effect is only relevant in *in vitro* active-HMM/actin networks with long filaments and has no biological significance.

This present study is the first in providing unambiguous experimental observed data for pure bundled and pure crosslinked actin networks. First explanation attempts to the results are made and waiting to be confirmed by other studies.

10. Outlook

As discussed earlier the presence of active crosslinker might influence the network structure that emerges during actin polymerization. Since in N-Ethylmaleimide-modified heavy meromyosin (NEM-HMM) the ATP hydrolysis activity is deactivated, but the rigor binding to actin is still possible, NEM-HMM may be used to clarify if the presence of active crosslinker during polymerisation alters the mechanical response by changing the network structure.

All actin binding molecular motors examined so far are driven by ATP-hydrolysis which has the advantage to control the crosslinking properties in motor/actin networks. Molecular motors are very diverse in structure and are therefore extremely useful to explore the relation between the structure and the mechanical properties of complex composite cytoskeletal networks.

Beside myosin II the molecular motor myosin V can also be used to crosslink actin networks. In contrast to myosin II, Myosin V is a processive motor with a long neck domain which enables the motor to walk along actin filaments in steps of 37 nm. Figure 10-1 right side shows myosin II and myosin V respectively. When myosin V acts as crosslinker the hinge may be more flexible compared to myosin II. In preliminary experiments it was possible to observe the sol-gel transition of myosin V/actin networks (Figure 10-1) by microrheometry. Since the hydrolyzation activity of myosin V is extremely slowed down by a small amount of ADP (Adenosin-di-Phosphate) in the sample volume (De La Cruz et al. 1999), one has to get rid of the ADP that appears with each motor cycle. The amount of ADP was reduced by mean of the enzyme apyrase which converts ADP and ATP to AMP (Adenosin-mono-Phosphate) very fast.



The transition from active state into the rigor state could only be observed when additional apyrase was added.

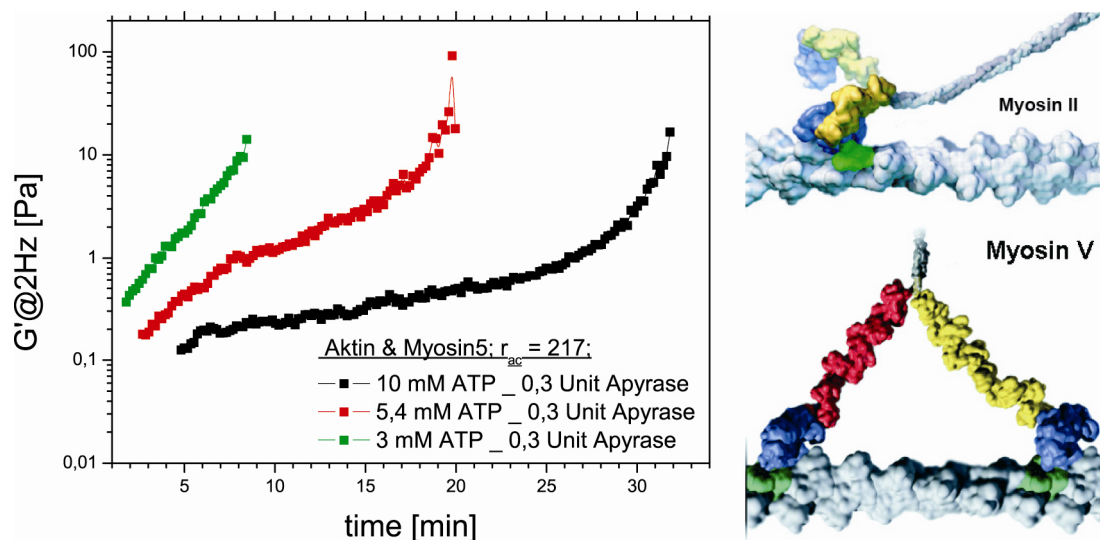


Figure 10-1 Left graph shows the sol-gel transition of myosin V/actin networks for different ATP concentrations forced by the use of the enzyme apyrase. Right handed both myosin II and myosin V is depicted respectively (Vale et al. 2000).

As already mentioned in chapter 6, it is not only possible to measure the sol-gel transition in HMM/actin networks the transition is also observed in myosin II/actin networks in the same way. Under physiological conditions the tail region of myosin II is able to oligomerize with other tails to thick bipolar microfilaments resulting in an array of heads (Figure 10-2), the rigor-myosin II/actin network structure (Figure 10-2) is therefore completely different than that of rigor-HMM/actin networks. The polymerization kinetics of myosin II microfilaments is strongly influenced by the concentration of several ligands (Harrington et al. 1972). It is therefore possible to adjust the length of the microfilaments. The experiments presented here were done with myosin II microfilaments of 1 μm size. The length of the microfilaments was adjusted by the KCl concentration in the solvent ($c_{\text{KCl}}=100\text{mM}$). As shown in Figure 10-2 the composite network consists of bundle and crosslinked filaments. Concomitant with the structural differences the elastic response G_0 of rigor-myosin II/actin networks scales more pronounced with the crosslinker concentration compared to HMM. The observed exponent ($G_0 \sim c_{\text{MyosinII}}^2$) (Figure 10-3) ranges between the exponent found for the pure bundled Peg6k/actin network ($G_0 \sim c_{\text{PEG6k}}^{3.5}$) and the one of the purely crosslinked rigor-HMM/actin network ($G_0 \sim c_{\text{HMM}}^{1.2}$).

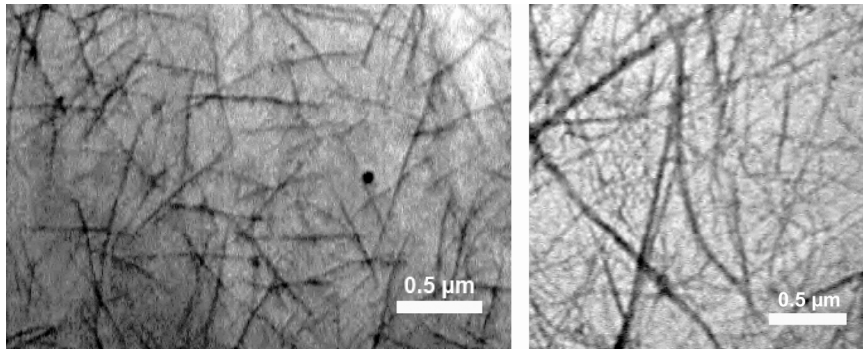


Figure 10-2 Left represents an electron microscopy picture of pure myosin II microneedles whereas the right electron microscopy picture represents a composite rigor-myosin II/actin network ($r_{ac}=64$) showing both bundles and filaments.

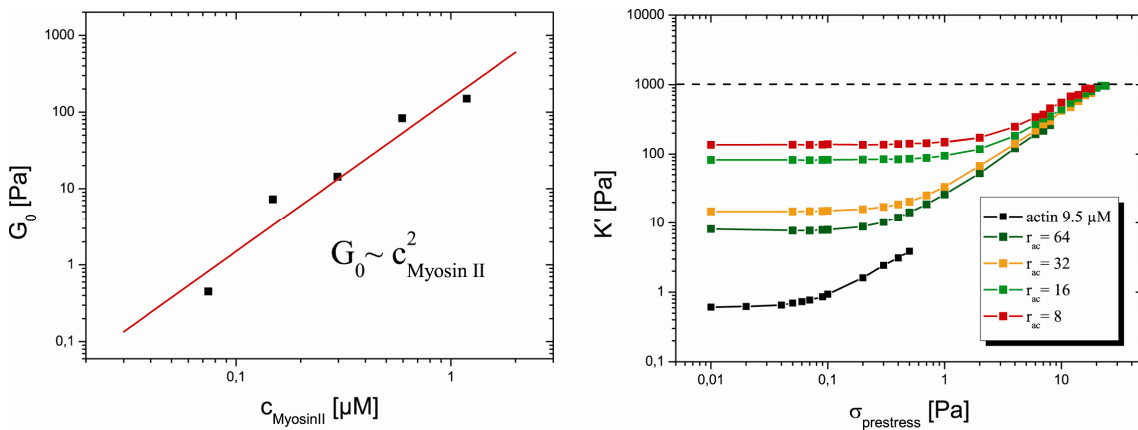


Figure 10-3 Left: The macrorheological modulus G_0 as a function of c_{HMM} taken from the frequency spectra reveals a scaling $G_0 \sim c_{MyosinII}^2$. Since the structure is build up of bundles and filaments it is expected for the scaling to be between the one for the pure bundled Peg6k/actin network ($G_0 \sim c_{PEG6k}^{3.5}$) and the one of the pure crosslinked rigor-HMM/actin networks ($G_0 \sim c_{HMM}^{1.2}$). Right: Respectively the prestress measurements are shown. The elasticity of these composite networks ranges over two orders of magnitudes and can withstand stresses up to 30 Pa. Interestingly the slope of the nonlinear regime seems not to change.

It was already convincingly shown, that on the one hand the different structure of crosslinker proteins results in different network structures with different scaling of $G_0(R)$ (Wagner 2003; Wagner et al. 2005) and on the other hand that the onset of the strong increase of G_0 is coupled to the appearances of bundles (Tharmann et al. 2006). This suggests that the strong increase of the plateau modulus as a function of concentration can be understood as a measure of the bundle propensity which dominates the mechanical effectiveness.

Therefore bundle networks where bundle length can be adjusted, like the rigor-myosin II/actin network may enlighten these rheological studies. Beside this rigor-myosin II/actin networks show an extreme stiffening prestress in experiments. The elasticity of these composite networks ranges over two orders of magnitudes and can withstand stresses up to 30 Pa (Figure 10-3).

Since myosin II is an important component in cells and is thought to play an essential role in generating contractile bundles in the cortex it is important to note that the mechanical response of cells is in the same range of elasticity (Fabry et al. 2003). Further investigations of these networks are therefore highly interesting.

In this outlook also measurements are shown to probe the properties of contractile myosin II/actin bundles by analysing vesicle shape. Vesicles embedded inside active-myosin II/actin networks can act as force sensors to measure forces in the range of pN. This is the magnitude of force that motor proteins typically exert on filaments. Vesicles were prepared either with positively charged lipids to couple electrostatically to the negatively charged actin filaments or with polymer spacers to repel the network. In parallel, a magnetic bead microrheometry measurement was carried out in the same chamber, so that the shape of the vesicle and the oscillations of the magnetic bead could be monitored at the same time. Figure 10-4 shows three phase contrast images of the vesicle and the magnetic bead in a time series. The elastic modulus of the network can be deduced from the bead oscillations. Figure 10-5 displays the tracking data of the bead movement. The amplitude of bead oscillation decreases drastically in time, which is indicative of a percolating crosslinked/bundled network. Additionally, the shape of the vesicle was analyzed over time to quantify its deformation. The strongest deformation of the vesicle occurred when the bead movement showed the largest

decrease in amplitude. Image analysis was done with a shape detection algorithm (Roth 2004). A scan over the entire sample showed several vesicles which deviated strongly in shape from their initial spherical or ellipsoidal shapes (Figure 10-5). This preliminary result shows that active-myosin II/actin networks seem to exert internal forces when they percolate and that lipid vesicles can serve as force sensors with appropriate resolution.

These specific contractile properties of myosinII/actin networks are also very interesting from the point of already crosslinked networks (e.g. filamin, α -actinin ...) with additional motor proteins active or in rigor state. The addition of motor proteins might result in an already prestressed network under tension. First experiments with such composite networks let assume that an optimal ratio between crosslinker and motor proteins has to be adjusted since both proteins compete for binding sites on actin filaments.

These preliminary results, present a selection of possible experiments in forthcoming works.

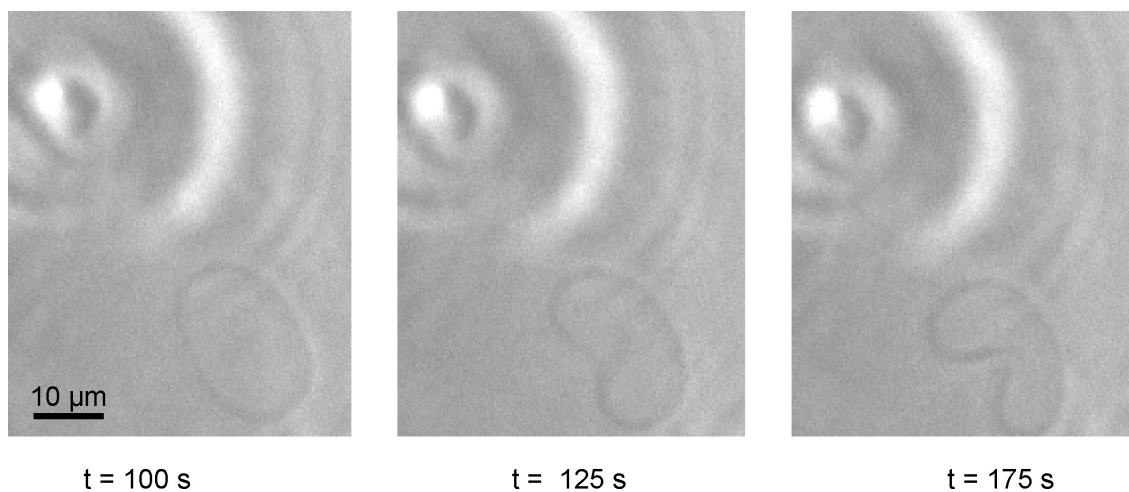


Figure 10-4 Microscopy images of a vesicle and a magnetic bead embedded in an active actin – myosin II network at successive times.

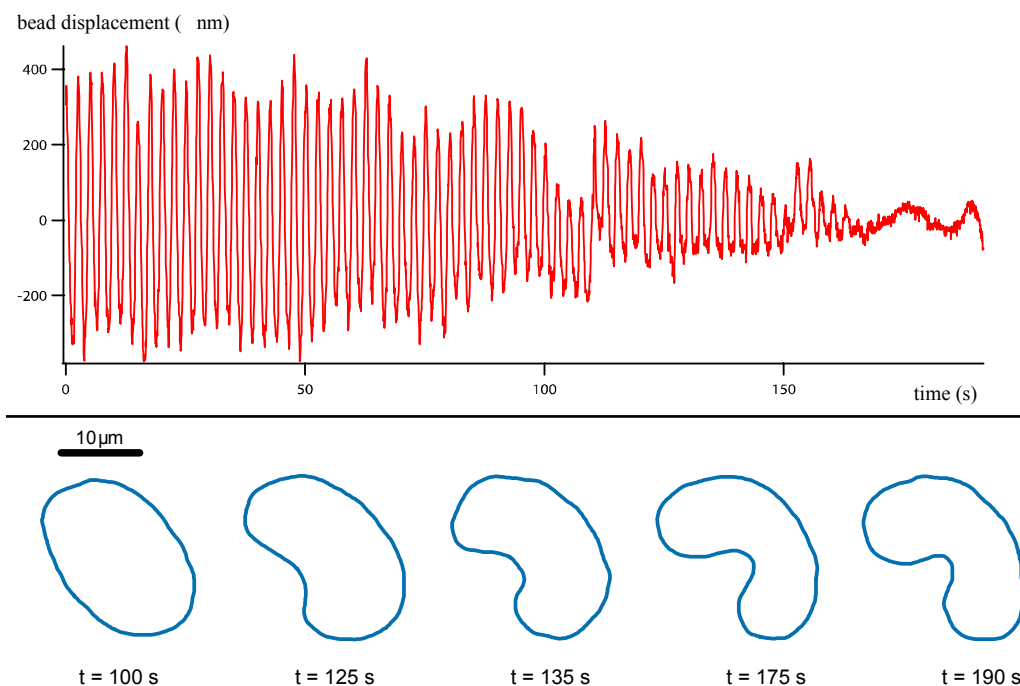


Figure 10-5 Figure shows the bead tracking data and vesicle shape (below) during the process of ATP depletion of an actin – myosin II network. The network stiffens and forces acting on it deform the vesicle.

III. Appendix

A. Physical Principles of the Experimental-Setups

Magnetic Tweezer

The physical principles are based on the theory of linear viscoelasticity that was discussed in detail in chapter 3.1. Using the magnetic tweezer the viscoelastic properties are determined by dynamic measurements, which are periodic in time. Measuring the frequency dependent response of the sample, the applied force $F(t)$ of the magnetic beads leads to a deflection $x(t)$. This can be expressed by an equation of motion where the mass m of the bead, the viscous and the elastic properties of the medium have to be concerned:

$$m \cdot \underbrace{\frac{\partial^2 x(t)}{\partial t^2}}_{\text{term of inertia}} + g_v \eta \cdot \underbrace{\frac{\partial x(t)}{\partial t}}_{\text{viscous response}} + \underbrace{g_e E \cdot x(t)}_{\text{elastic response}} = F(t) \quad (\text{Eq.A.1})$$

The first term in Eq.A.1 concerning the inertia is very small due to the small values of m and thus negligible. The geometrical prefactor ($g_v \eta$) in the second term representing the viscosity can be obtained from Stokes law. If a bead is moved in a pure viscous fluid the Eq.A.1 can be simplified to $F_{Stokes} = 6\pi R \eta \partial x(t) / \partial t$ yielding $g_v = 6\pi R$.

The elastic prefactor g_e in the third term of Eq.A.1 was calculated to be $6\pi R$ (Ziemann 1997). Combining all results the equation of motion simplifies to

$$6\pi R \eta \cdot \frac{\partial x(t)}{\partial t} + 6\pi R E \cdot x(t) = F(t). \quad (\text{Eq.A.2})$$

The viscosity η and the Young modulus E are time dependent for viscoelastic samples, and have to be written in the terms of the linear viscoelasticity $G'(\omega)$ for $E(\omega)$ and $G''(\omega)/\omega$ for $\eta(f)$. A sinusoidal excitation $F(t) = F_0 \sin(\omega t - \delta)$ results in a sinusoidal oscillation of the colloidal probe $x(t) = x_0 \sin(\omega t)$ with a phase shift δ . Using the addition theorem, $x(t)$ and $F(t)$ in Eq.A.2 one obtains

$$6\pi R x_0 (G''(\omega) \cos(\omega t) + G'(\omega) \cdot \sin(\omega t)) = F_0 (\cos(\omega t) \sin(\delta) + \sin(\omega t) \cos(\delta)). \quad (\text{Eq.A.3})$$

A comparison of both sides from Eq.A.3 yields

$$\begin{aligned} G'(\omega) &= \frac{F_0}{6\pi R x_0(\omega)} \cos(\delta(\omega)), \\ G''(\omega) &= \frac{F_0}{6\pi R x_0(\omega)} \sin(\delta(\omega)). \end{aligned} \quad (\text{Eq.A.4})$$

Hence, if one knows the applied force and measures the amplitude and the phase shift of the oscillations, it is possible to calculate the viscoelastic moduli G' and G'' .

The magnetic tweezer is calibrated by measuring the response signal of a M-450 Dynabead embedded in a pure viscous fluid (Glycerol containing a fraction of cesium-chloride⁶ to adjust the density to the density of the beads) with a known viscosity η . Using the Stokes equation $I_{coils} \sim F_{Stokes} = 6\pi R \eta \partial x(t) / \partial t$ one can obtain the dependency between the force and the coil current, as shown in Figure A-6.

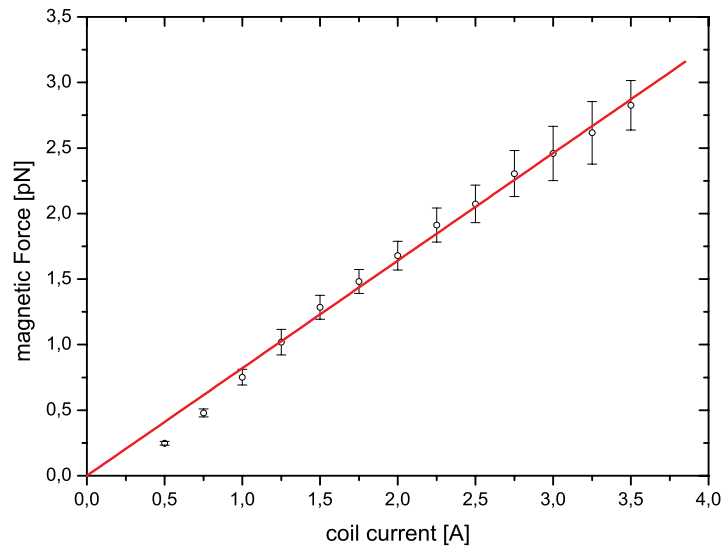


Figure A-6 Calibration curve of the Magnetic Tweezer by analyzing the response signal of a bead embedded in a purely viscous medium of viscosity η . The red line is a linear fit to the data. The error bars represent the bead-to-bead variation.

⁶ The density of Caesium-chloride is similar to the one of the beads resulting in levitation of the latter.

Passive Microrheology

The embedded CLM beads are subject to thermal motion driven by the energy $k_B T$. Only in sufficiently soft materials thermal motion give rise to a detectable displacement which limits the applicability of the method. The local elasticity can be obtained from the time–displacement correlated function that is called the mean squared displacement (MSD):

$$\langle \Delta \bar{x}^2(\tau) \rangle = \int_0^t |\bar{x}(t+\tau) - \bar{x}(t)|^2 dt \quad (\text{Eq.A.5})$$

where \bar{x} defines the bead position and τ is the lag time. The diffusion in purely viscous fluids (Brownian motion) is well understood and described by the diffusion equation

$$\langle \Delta \bar{x}^2(\tau) \rangle = 6D\tau. \quad (\text{Eq.A.6})$$

Using the Stokes-Einstein equation $D = k_B T / 6\pi\eta a$, where a is the particle radius, the viscosity η can be obtained from the MSD.

In contrast, viscoelastic material like actin behaves much more complex. The motion of the tracers reveals both a viscous and elastic contribution. The MSD of a tracer in viscoelastic material exhibits an anomalous subdiffusive behavior and scales differently with τ (Wong et al. 2004):

$$\langle \Delta \bar{x}^2(\tau) \rangle \sim \tau^\alpha \quad (\text{Eq.A.7})$$

In the case of pure Brownian motion the MSD scales with $\alpha = 1$ (which is the case described above by Eq.A.6) which is contrary to subdiffusive motion where $0 < \alpha < 1$ (including elastic and viscous response). Furthermore, if the bead is locally constrained, the response becomes purely elastic ($\alpha=0$). In this case the thermal energy density of the particle $k_B T / a^3$ equals the elastic energy density of the material $\langle \Delta \bar{x}^2(\tau \rightarrow \infty) \rangle G' / a^2$ that is deformed.

A plateau in the MSD demonstrates that the bead is confined (Figure A-7). Therefore the elastic modulus can be obtained from the MSD using:

$$G_0 = \frac{k_B T}{\pi \langle \Delta \bar{x}^2(\tau \rightarrow \infty) \rangle a} \quad (\text{Eq.A.8})$$

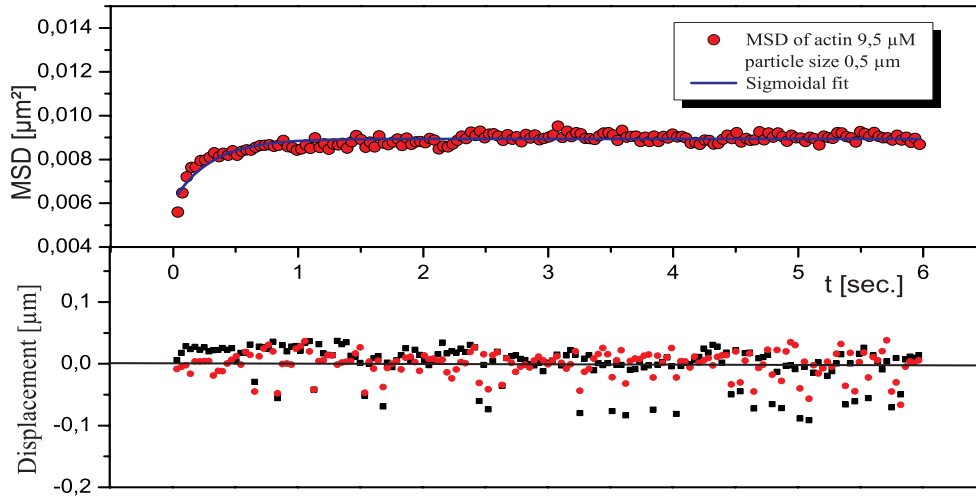


Figure A-7 Displacement and resulting mean squared displacement of a bead in 9,5 μM actin solution. The diameter of the embedded bead is in the order of the mesh size. With a sigmoidal fit the plateau of the MSD is obtained.

Rotating Disc Rheometer

The torsional motion of the glass disc (Figure 4-5) can be described mathematically by the equation of motion (Mueller et al. 1991):

$$\Theta \frac{\partial^2 \alpha(t)}{\partial t^2} + D_G + MB_x \alpha(t) = D_\eta + MB_y(t) \quad (\text{Eq.A.9})$$

where

$$\Theta \frac{\partial^2 \alpha(t)}{\partial t^2} = \text{acceleration dependent inertia of the disc } (\Theta \text{ moment of inertia),}$$

$$D_G = \text{torsional moment resulting from the elastic behavior,}$$

$$D_\eta = \text{drag torque resulting from the viscous behavior,}$$

$$MB_x = \text{constant torque of the retain coils,}$$

$$MB_y(t) = \text{dynamic torque of the deflection coils, and}$$

$$\alpha(t) = \text{time dependent rotating angle.}$$

D_η is defined mainly by geometrical aspects resulting on one hand from the effects of the disc border and on the other hand from the surface area of the disc. Thus it is important to have a large distance $R_2 - R_1$, thin glass plates, and a very small height of the sample in order to neglect border effects. This is the reason for the used geometry of the cuvette and the disc ($R_1 = 4\text{mm}$; $R_2 = 7.5\text{mm}$; $d_{\text{disc}} = 0.1\text{mm}$; $h_{\text{sample}} = 2\text{mm}$) (Tempel 1996). In order to get a linear, frequency independent decrease of the shear wave into the purely viscous sample it is important to ensure that the penetration depth of the shear wave, $\delta = \sqrt{2\eta / \omega\rho}$ (η : viscosity, ρ : density of the sample), is greater than the sample height h .

In this limit the following equation of the drag torque is applicable (for the exact description see (Tempel 1996)):

$$D_\eta = -\frac{\pi}{2} R_1^4 \dot{\alpha}(t) \frac{\eta}{h} \quad (\text{Eq.A.10})$$

The torsional moment resulting from the elastic properties of the sample D_G is calculated as (Ruddies 1992):

$$D_G = \frac{\pi}{2} R_1^4 \alpha(t) \frac{G}{h} \quad (\text{Eq.A.11})$$

Inserting Eq.A.10 and Eq.A.11 into Eq.A.9 yields an equation of motion:

$$\Theta \frac{\partial^2 \alpha(t)}{\partial t^2} + \frac{\pi R_1^4}{2h} \cdot \left(G \alpha(t) + \eta \frac{\partial \alpha(t)}{\partial t} \right) + MB_x \alpha(t) = MB_y(t). \quad (\text{Eq.A.12})$$

For a sinusoidal excitation $MB_y(t) = MB_{y_0} \exp i(\omega t + \varphi)$ and a sinusoidal oscillation of the shear wave $\alpha(t) = \alpha_0 \exp i\omega t$ one obtains for Eq.A.12

$$-\omega^2 \Theta + \frac{\pi R_1^4}{2h} \cdot (G + i\omega\eta) + MB_x = \frac{MB_{y_0}}{\alpha_0} \exp i\varphi. \quad (\text{Eq.A.13})$$

With the definition of the complex modulus $G^* = G' + iG'' = G + i\eta\omega$ Eq.A.13 can be split into the expressions

$$G_1 \sim \frac{MB_{y_0}}{\alpha_0} \cos \varphi = -\omega^2 \Theta + MB_x + \frac{\pi R_1^4}{2h} G', \quad (\text{Eq.A.14})$$

$$G_2 \sim \frac{MB_{y_0}}{\alpha_0} \sin \varphi = \frac{\pi R_1^4}{2h} G''. \quad (\text{Eq.A.15})$$

It can be easily seen that G_1 and G_2 , which are measured, are dimensionless values proportional to the storage modulus G' and loss modulus G'' of the sample. Thus, knowing the applied torque and measuring the amplitude of the angular deflection and the phase shift between the oscillations it is possible to calculate the viscoelastic moduli G' and G'' . In order to determine the proportional factor for the extraction of (the physical parameters) G' and G'' a calibration of the setup, as explained in the following section, has to be done.

The rheometer is calibrated by a measurement of a purely viscous fluid with a known viscosity η . In this case $G' = 0$, $G'' = \eta\omega$ and Eq.A.14, Eq.A.15 reduce to

$$G_1 \sim \frac{MB_{y_0}}{\alpha_0} \cos \varphi = -\omega^2 \Theta + MB_x, \quad (\text{Eq.A.16})$$

$$G_2 \sim \frac{MB_{y_0}}{\alpha_0} \sin \varphi = \frac{\pi R_1^4}{2h} \eta \omega. \quad (\text{Eq.A.17})$$

Eq.A.16 can be interpreted as a description of a damped (viscous fluid) harmonic oscillator with an elastic element (elastic moment of the retain coils) (see Figure A-8 c)). At the resonance frequency $\cos \varphi = 0$ (Figure A-8 a)) and therefore $\omega_0^2 \Theta = MB_x$. Accordingly the resonance frequency ω_0 is obtained by the x-axis crossing of the quadratic fit $G_1(\omega) = ax^2 + b \sim \omega^2 \Theta + G_1^{MB_x}$. With $\Theta = \frac{1}{2} m_{disc} R_1^2$ the constant torque of the retain coils, MB_x , can be calculated. Thus, if one knows the physical value MB_x that is comparable to the dimensionless value of the fit $G_1^{MB_x}$ (Figure A-8 a)), the scaling of the absolute value G' in Eq.A.14 can be obtained:

$$\frac{MB_x}{G_1^{MB_x}} \cdot G_1 = MB_x + \frac{\pi R_1^4}{2h} G' \quad (\text{Eq.A.18})$$

$$\Rightarrow G' = G_{abs} \frac{G_1 - G_1^{MB_x}}{G_1^{MB_x}} \quad \text{with} \quad G_{abs} = \frac{2h MB_x}{\pi R_1^4} G_0 \quad (\text{Eq.A.19})$$

Another (more precise and more practicable) method for the determination of the scaling factor G_{abs} is the measurements of G_2 (Figure A-8 b)). The absolute value of G'' has to scale like G' . From Eq.A.15 and the obtained result of G_{abs} from Eq.A.19 it follows

$$G'' = \omega \eta = G_{abs} \cdot \frac{G_2}{G_1^{MB_x}} \Rightarrow G_{abs} = \frac{G_1^{MB_x} \eta}{G_2 / \omega}. \quad (\text{Eq.A.20})$$

Experience shows that the calculation of MB_x is much more inaccurate than the measurement of η . Therefore, the second method to calibrate the rheometer is more suitable. For every calibration the values of G_{abs} and $G_1^{MB_x}$ have to be determined. On the

other hand, G_{abs} is also a measure for the maximum resolution of the rheometer, typically around 0.01 Pa, dependent on the mass of the rotating disc and the retain torque.

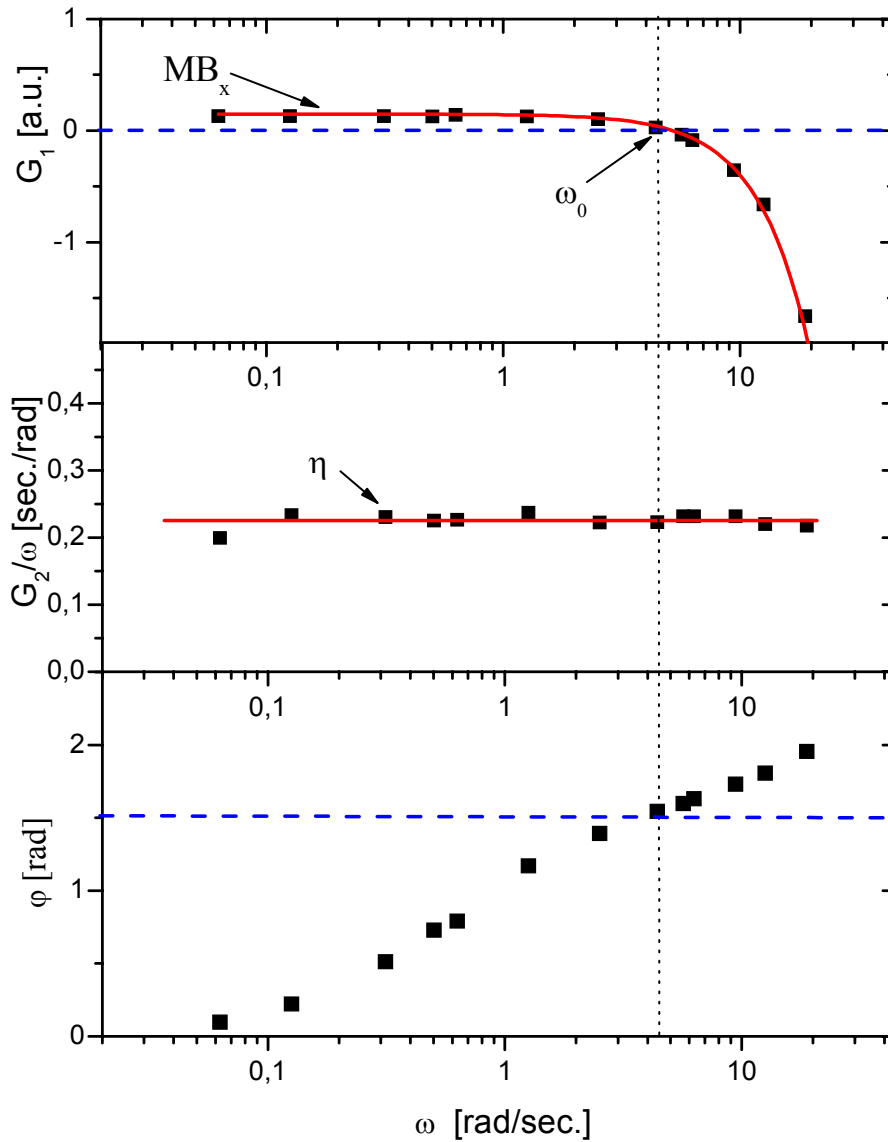


Figure A-8 Example of a calibration measurement. a) The measurement of G_1 provides information of the resonance frequency ω_0 and the torque of the retain coils MB_x . b) The value of G_2 has to be constant over the whole probed frequency range as it is a value for the viscosity of the measured sample. c) The phase shift as a function of ω between excitation and response signal behaves like a damped oscillator with spring element.

B. Rheology of Biofilms

Normally one is not familiar with the term "biofilm," but biofilms are ubiquitous. For example the plaque on teeth that causes tooth decay is a type of bacterial biofilm or the biofilm-coated rocks in a stream or river (Figure B-1).

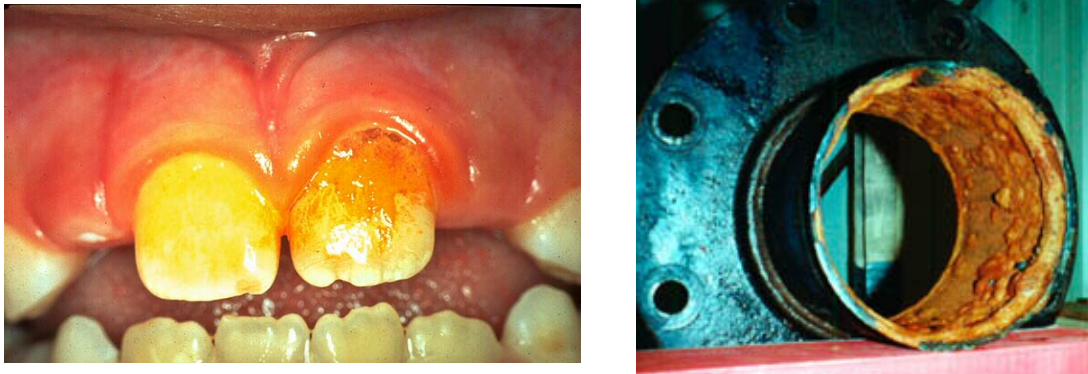


Figure B-1 right handed picture shows hundreds of microbial species colonize the human mouth. Some species are pathogenic, and can cause infection, tooth decay and gum disease. Left picture shows a sprinkler pipe covered with a biofilm.

These microbial biofilms growth preferably on surfaces and produces high cost due to equipment damage, product contamination, energy losses and medical infections. Typical methods to remove biofilms (e.g. in medicine antibiotics, and disinfection) are mostly unsuccessful.

Biofilm grow when bacteria stick onto surfaces in aqueous environments. They start to expel a slimy, sticky substance that works as an anchor on various materials. If they gain ground on a surface, biofilms are able to do a diversity of harmful but as well helpful reactions, depending on the surrounding environmental conditions. A positive application of biofilms can be the biological recycling of hazardous waste, biofiltering industrial water, and protecting soil and groundwater from contamination by the film.

It is a subject of intrinsic interest to those concerned with their removal. But also the scientific approach is of interest, since biofilms are complex structures attached to surfaces and composed of bacteria which surround themselves with a self-generated matrix, the extracellular polymeric substance (EPS). This matrix is composed of

polysaccharides, proteins and other matter such as bacterial fragments, membrane vesicles and external substances incorporated into the biofilm [xx].

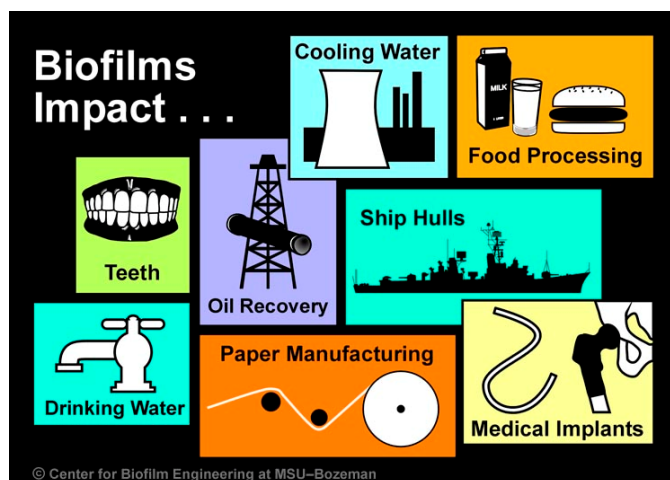


Figure B-2 The picture represents a collection of the various industry which is concerned by biofilms. (source: http://www.erc.montana.edu/Res-Lib99-SW/Image_Library/Structure-Function/Full-image%20pages/CBE96-BfsImpact.htm)

The EPS is a complex and very important component of all biofilms, given that architectural structure and mechanical stability to the growing bacteria. Additionally, a variety of enzymic and regulatory activities go on within the matrix. An understanding of the mechanical properties of biofilms is of highly interest.

Bacterium *Pseudomonas Aeruginosa*

For rheological measurements the bacterium *Pseudomonas aeruginosa* (PAO) (lat. *aerugo verdigris*) was used which is a member of the bacterial genus *Pseudomonas*. PAO is able to form rods or cocci with a dimension of 1.5 -5 μm length and 0.5 – 0.9 μm width (Figure, left image). Usually PAO is nonpathogenic for healthy people. They need special surface conditions to thrive which are only available in humans who are already weakened in their immune system. This bacterium is able to infect the urinary tract, burns, wounds, and also causes blood infections. Cystic fibrosis patients are also predisposed to *aeruginosa* infection of the lungs. If the infection gained ground, PAO produces a high amount of toxic proteins and enzymes which are able to harm the tissue and affect cell membranes and viscera. The bacteria surround themselves with a self-generated matrix, the extracellular polymeric substance. This matrix is composed of polysaccharides, proteins and other matter such as bacterial fragments, membrane

vesicles and external substances incorporated into the biofilm. Both the slimy EPS and the embedded bacteria represent the biofilm that cannot be phagocytosed and therefore is able to protect the bacteria from antibiotics and antibodies by providing a physical barrier (Figure 2-1, right image). To enable transport of materials and wastes through the biofilm it contains numerous channels. Some of the channels are hydrophilic and others are hydrophobic.

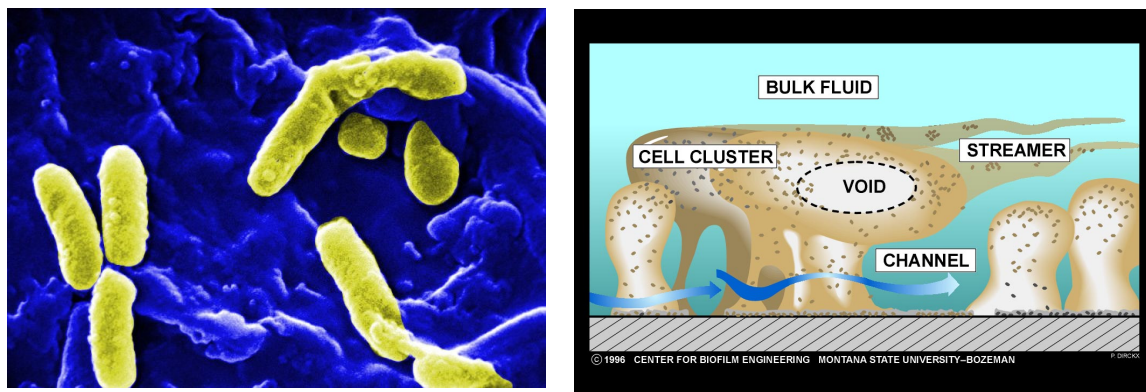


Figure B-3 left picture: Scanning Electron Micrograph of *Pseudomonas aeruginosa*. (Image provided by Janice Carr. Courtesy of the Centers for Disease Control and Prevention) right picture: Conceptual illustration of the heterogeneity of biofilm structure, with labeled bacterial clusters (brown points represent single bacteria), streamers, and waterchannels. (source: http://www.erc.montana.edu/Res-Lib99-SW/Image_Library/Structure-Function/Full-image%20pages/Biofilmwb-jpg.htm).

Bacterial strains, culture conditions, and biofilm growth

Pseudomonas aeruginosa strains PAO1 (non-mucoid, obtained from J. S. Lam, University of Guelph) were used throughout this study and were maintained on Luria-Bertani (LB) agar.

Biofilms were cultivated in (30mm) Petri dishes which were slightly larger in diameter than the rheometer measuring head. Prior to inoculation, the growth chambers were pre-conditioned with dilute LB broth ($1/10^{\text{th}}$ the recommended concentration) for 1 hour. At this point, the Petri plates were inoculated with 100 μL of an overnight culture of a *P. aeruginosa* strain (optical density at 600 nm = 0.6). Samples were then placed on a rotary shaker (30 rpm) at room temperature for 4 days to allow for biofilm growth. Every 12 hours post-inoculation, spent growth media was carefully removed and replaced with sterile LB broth. After 4 days of growth, spent media was replaced immediately prior to the rheometry measurements.

Rheometry

For measurements of the mechanical response of living biofilms the setup of the commercial rheometer MCR301 has been modified. To position a biofilm sample in the rheometer a self-made base plate (Aluminum) was put over the fixed one and pinched (Figure B-4, left handed). The advantage of the self-made base plate is the flexibility to exchange the middle section, a precisely inserted plate on which the Petri dish with the growing biofilm is glued on. To eliminate any movement of the plate in the middle section during measurement, the inset was covered with vacuum grease and after inserting the plate with the biofilm a vacuum was pumped to suck the plate. By providing several middle section plates, it is possible to measure easily different biofilms after 4 days of growth in the Petri dish. To prevent dehydration of the biofilm during measurement growth media was not removed. For measurements with biofilms the rheometer was adjusted to normal force mode which enables to control the normal force. To be sure to have a biofilm grown in the dish, the normal force was recorded during the time the measure head was lowered slowly (Figure B-4, right handed). Figure B-4 (right handed) shows respectively the signal of the normal force for an empty dish, a dish filled up with water and the dish in which the biofilm was grown.

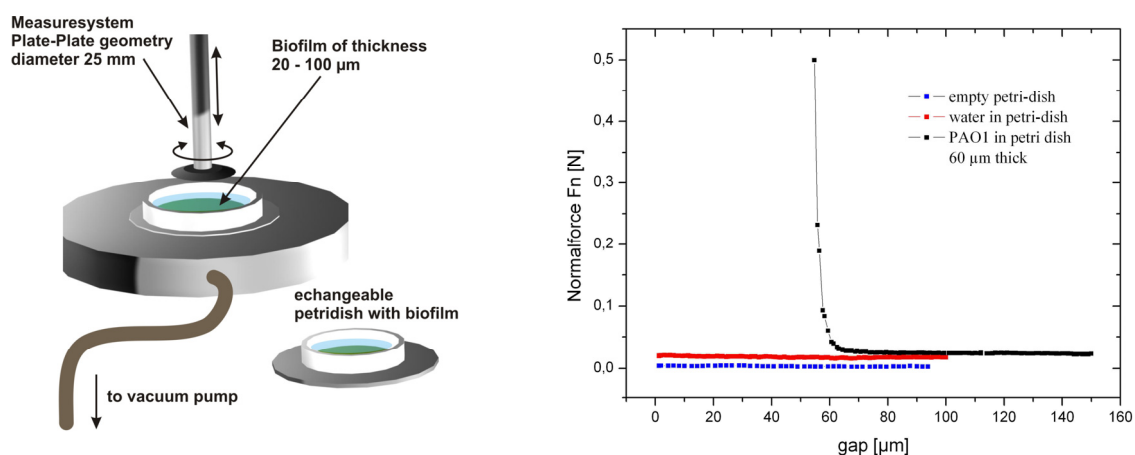


Figure B-4 left picture shows the adapted setup. Right graph shows the recorded normal force during lowering the measure tool.

The distinct increase of the normal force indicates the thickness of the biofilm below. To eliminate slippage due to insufficient contact between biofilm and the measure head, a low constant compressive normal force (between 0,1-2 N) were applied during measurement. The squeezed biofilms were allowed to undergo an adjustment period of

5 min after the normal force was applied. After this the response of the biofilm to harmonic oscillations was studied under a low constant strain of 3% across a frequency range 40 mHz -100 Hz. This was done for different compressive forces successive.

Theoretical Model

The theoretical model which should be adapted to the mechanical response of biofilms is called “Dissipative Particle Dynamics (DPD)”. It is a model which represents all components of a system by points interacting via forces, the ranges of which are determined by the smallest scale. Thus, if the smallest scale is the dimension of a bacterium ($\sim 2 \mu\text{m}$), one represents water by points which interact via forces possessing a range of $\sim 2 \mu\text{m}$. One can think of the basic “unit” of the water model being a spherical mass of water, radius $\sim 2 \mu\text{m}$. The entire system being modeled is represented by such spheres which interact amongst themselves by forces which are, most conveniently, piecewise linear. Note that if an object interacts with its surroundings via two different forces, it can possess two different “sizes”, e.g. an object possessing both a soft core repulsion and longer-range electrostatic interactions (Groot 2003). Time-development is determined by Newton’s equations and molecular dynamics (e.g. the Velocity Verlet algorithm (Pink 2004)).

To create a mesoscale cellular model of a growing biofilm in flowing water with a designed flow profile individual bacteria are represented by pairs of spheres coupled by a spring with spring constant $\gg k_B T$. Model bacteria grow and divide by creating copies of each sphere and the spring, and letting the attached pair separate over some average time. To create an incompressible fluid, water spheres repel each other strongly (Uhde et al. 2005) and the density is ~ 3 (e.g. (Shillcock et al. 2002)). Bacteria attach themselves to sites on the attachment surface by (breakable) springs. The EPS polymer scale is likely $\sim 10^{-2}$ smaller than the bacterial scale and EPS is represented as a continuum uniformly filling a water sphere with a density reflecting the local quantity of EPS. EPS can diffuse between water spheres and can become attached to a bacterium by a breakable spring.

Results & Discussion

The frequency dependent mechanical response of the biofilm PAO1 let assumes that the response is elastic dominated over the whole frequency range probed. With rising compressive force (0.15 N – 2 N) the elastic modulus G' increases over nearly two orders of magnitude. Concomitant with increasing elasticity a distinct minimum in the frequency range 10Hz-40Hz becomes more pronounced and shifted to higher frequencies.

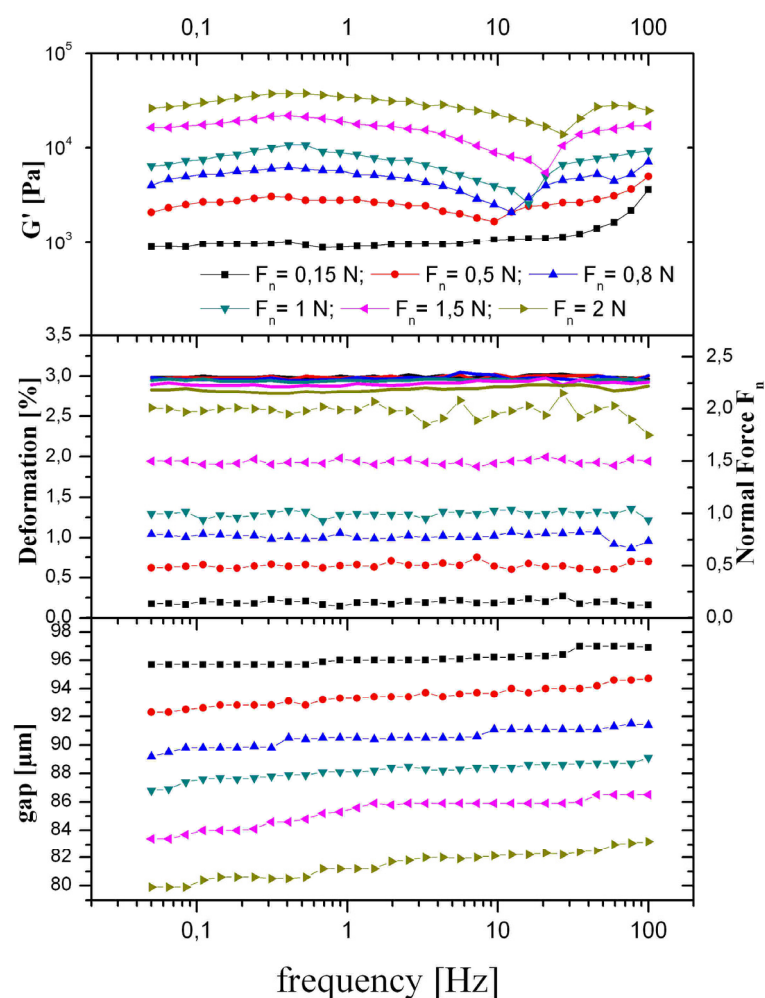


Figure B-5 Figure represents the frequency dependent mechanical response of the biofilm PAO. Upper graph shows the frequency dependency of the viscoelastic modulus G' . Middle graph represents the strain (line) that is adjusted to 3% and the normal force (line-symbol) which was held constant over the whole frequency range probed. Lower graph shows the change in the gap between the measure head and the bottom of the Petri dish during time.

Since the normal force, the strain and the gap stays constant during the frequency range 10Hz-40Hz this minimum is a special feature of the viscoelastic properties of the PAO1 biofilm (Figure B-5). Beside this the biofilm is compressed by around 16 μm over time. The distinct minimum was observed for all measured biofilms; whereas the absolute value of G' differs for different biofilms. This may be attributed to different thicknesses of the measured samples that might influence strongly the elastic properties of the film. As a first suggestion this minimum may be attributed to a harmonic resonance in the biofilm resulting from the coupling of the EPS to the bacteria. Under higher normal force the density of bacteria is changed and the resonance response should be shifted to higher frequencies as it is observed.

Conclusion

These preliminary results are shown here, to convince that macrorheological measurements are a strong tool for the characterization of thin biofilms. A theoretical basis to understand the intriguing mechanical response of these extremely complex heterogeneous structures is coming up by the model of Dissipative Particle Dynamics. Since cooperation's with different Canadian universities are still in process forthcoming work will enlighten this field of research soon. As already mentioned above, there is a strong interest in solving a series of problems caused by biofilms. Therefore this research may be also supported by third-party funds.

C. Buffers

G-buffer pH 8

Substance	Mol mass <i>M</i>	Concentration
TRIS	121.1 g/mol	2 mM
CaCl ₂	147.0 g/mol	0.2 mM
DTT	154.2 g/mol	0.2 mM
ATP	551.2 g/mol	0.2 mM
20%ige Lösung NaN ₃		0.005%

10 x F-buffer pH 7,5 standard

Substance	Mol mass <i>M</i>	Concentration
TRIS	121.1 g/mol	20 mM
MgCl ₂	203.3 g/mol	20 mM
CaCl ₂	147.0 g/mol	2 mM
DTT	154.2 g/mol	2 mM
ATP	551.2 g/mol	5 mM
KCl ₂	74.56 g/mol	1 M

For measurements to determine the sol-gel transition of composite myosin/actin networks, lyophilized actin were dialyzed against G-buffer without ATP. Polymerization was initialized by standard F-buffer without ATP. ATP was added separately before polymerization.

D. Bibliography

Alberts, B., A. Johnson, et al. (2002). *Molecular Biology of the Cell*. New York, Garland Science.

Asakura, S. and F. Oosawa (1954). "On Interaction between 2 Bodies Immersed in a Solution of Macromolecules." *Journal of Chemical Physics* 22(7): 1255-1256.

Bechinger, C., H.-H. v. Grünberg, et al. (1999). "Entropische Kräfte." *Physikalische Blätter* 55(12).

Berger, C. E. M., P. M. Fagnant, et al. (2001). "ADP Binding Induces an Asymmetry between the Heads of Unphosphorylated Myosin." *J. Biol. Chem.* 276(26): 23240-23245.

Borukhov, L., R. F. Bruinsma, et al. (2005). "Structural polymorphism of the cytoskeleton: A model of linker-assisted filament aggregation." *Proceedings of the National Academy of Sciences of the United States of America* 102(10): 3673-3678.

Bullitt, E. S., D. DeRosier, et al. (1988). "Three-dimensional reconstruction of an actin bundle." *Journal of Cell Biology* 107(2): 597-611.

Carrier, M. F. (1987). "Measurement of Pi dissociation from actin filaments following ATP hydrolysis using a linked enzyme assay." *Biochem Biophys Res Commun* 143: 1069-1075.

Claessens, M. M. A. E., M. Bathe, et al. (2005). in preparation.

Claessens, M. M. A. E., R. Tharmann, et al. (2006). "Microstructure and viscoelasticity of confined semiflexible polymer networks." *Nature Physics* in press.

-
- Cooper, J. A., J. Bryan, et al. (1987). "*Microinjection of Gelsolin into Living Cells.*" *Journal of Cell Biology* 104(3): 491-501.
- Crocker, J. C., M. T. Valentine, et al. (2000). "*Two-point microrheology of inhomogeneous soft materials.*" *Physical Review Letters* 85(4): 888-891.
- De La Cruz, E. M., A. L. Wells, et al. (1999). "*The kinetic mechanism of myosin V.*" *PNAS* 96(24): 13726-13731.
- de Vries, R. (2001). "*Flexible Polymer-Induced Condensation and Bundle Formation of DNA and F-Actin Filaments.*" *Biophys. J.* 80(3): 1186-1194.
- Detmers, P., A. Weber, et al. (1981). "*7-chloro-4-nitrobenzeno-2-oxa-1,3-diazole actin as a probe for actin polymerization.*" *Journal of Biological Chemistry* 256(1): 99-105.
- Dubochet, J., M. Adrian, et al. (1988). "*Cryo-electron microscopy of vitrified specimens.*" *Quarterly Reviews in Biophysics* 21: 125-228.
- Dubochet, J., J. Lepault, et al. (1982). "*Electron microscopy of frozen water and aqueous solutions.*" *Journal of Microscopy* 128(3): 219-237.
- Eisenberg, E., L. Dobkin, et al. (1972). "*Binding of actin to heavy meromyosin in the absence of adenosine triphosphate.*" *Biochemistry* 11(25): 4657 - 4660.
- Ellis, R. J. (2001). "*Macromolecular crowding: an important but neglected aspect of the intracellular environment.*" *Current Opinion in Structural Biology* 11(1): 114-119.
- Ellison, P. A., Z. S. DePew, et al. (2003). "*Both Heads of Tissue-derived Smooth Muscle Heavy Meromyosin Bind to Actin in the Presence of ADP.*" *J. Biol. Chem.* 278(7): 4410-4415.

- F. Gittes, B. S., P. D. Olmsted, F. C. MacKintosh, C. F. Schmidt (1997). "*Microscopic Viscoelasticity: Shear Moduli of Soft Materials Determined from Thermal Fluctuations.*" PHYSICAL REVIEW LETTERS 79: 3286-3289.
- Fabry, B., G. N. Maksym, et al. (2003). "*Time scale and other invariants of integrative mechanical behavior in living cells.*" Physical Review E (Statistical, Nonlinear, and Soft Matter Physics) 68(4): 041914.
- Finer, J. T., R. M. Simmons, et al. (1994). "*Single myosin molecule mechanics: piconewton forces and nanometer steps.*" 368(6467): 113-119.
- Frey, E. (2001). Physics in Cell Biology: Actin as a Model System for Polymer Physics. *Advances in Solid State Physics*. B. Kramer. Berlin Heidelberg, Springer-Verlag. 41: 345-356.
- Frey, E., K. Kroy, et al. (1998). Statistical mechanics of semiflexible polymers: theory and experiment. *Dynamical networks in physics and biology*. G. Forgacs and D. Beysens, EDP Sciences Springer Verlag.
- Gardel, M. L. (2004). *Elasticity of F-actin Networks*. PhD, Department of Physics, Harvard University, Cambridge
- Gardel, M. L., J. H. Shin, et al. (2004). "*Elastic Behavior of Cross-Linked and Bundled Actin Networks.*" Science 304(5675): 1301-1305.
- Gardel, M. L., J. H. Shin, et al. (2004). "*Scaling of F-actin network rheology to probe single filament elasticity and dynamics.*" Physical Review Letters 93(18): 188102.
- Gardel, M. L., M. T. Valentine, et al. (2003). "*Microrheology of entangled F-actin solutions.*" Physical Review Letters 91(15).
- Gaub, H. E. and H. M. McConnell (1986). "*Shear Viscosity of Monolayers at the Air-Water Interface.*" Journal of Physical Chemistry 90: 6830-6832.

-
- Gennes, P. G. D. (1979). *Scaling Concepts in Polymer Physics*. Ithaca and London, Cornell Univ. Pr.
- Gibson, L. J. and M. F. Ashby (1999). *Cellular Solids: Structure and Properties*. Cambridge, Cambridge University Press.
- Greene, L. and E. Eisenberg (1980). "The binding of heavy meromyosin to F-actin." *J. Biol. Chem.* 255(2): 549-554.
- Groot, R. D. (2003). "Electrostatic interactions in dissipative particle dynamics--- simulation of polyelectrolytes and anionic surfactants." *The Journal of Chemical Physics* 118(24): 11265-11277.
- Hanson, J. and J. Lowy (1963). "The structure of F-actin and of actin filaments isolated from muscle." *Journal of Molecular Biology* 6: 46-60.
- Harrington, W. F. and S. Himmelfarb (1972). "Effect of adenosine di- and triphosphates on the stability of synthetic myosin filaments." *Biochemistry* 11(16): 2945.
- Hartwig, J. H. and D. J. Kwiatkowski (1991). "Actin-binding proteins." *Curr. Opin. Cell Biol.* 3: 87-97.
- Head, D. A., A. J. Levine, et al. (2003). "Distinct regimes of elastic response and deformation modes of cross-linked cytoskeletal and semiflexible polymer networks." *Physical Review E* 68(6): 061907.
- Henle, M. L. and P. A. Pincus (2005). "Equilibrium bundle size of rodlike polyelectrolytes with counterion-induced attractive interactions." *Phys. Rev. E* 71: 060801.
- Heussinger, C. and E. Frey (2006). "The Role of Architecture in the Elastic Response of Stiff Polymer Networks." [oai:arXiv.org:cond-mat/0512557](https://arxiv.org/abs/2006.01057) (2006-01-05).
- Heussinger, C. and E. Frey (2006). "Stiff Polymers, Foams and Fiber Networks." *Physical Review Letters* 96(1): 017802.

- Hinner, B., M. Tempel, et al. (1998). "*Entanglement, elasticity, and viscous relaxation of actin solutions.*" *Physical Review Letters* 81(12): 2614-2617.
- Hodge, T. and C. M.J.T.V. (2000). "*A Myosin Family Tree.*" *Journal of Cell Science* 113: 3353-3354.
- Holmes, K. C., I. Angert, et al. (2003). "*Electron cryo-microscopy shows how strong binding of myosin to actin releases nucleotide.*" 425(6956): 423-427.
- Holmes, K. C., D. Popp, et al. (1990). "*Atomic model of the actin filament.*" *Nature* 347: 44 - 49.
- Hosek, M. and J. X. Tang (2004). "*Polymer-induced bundling of F actin and the depletion force.*" *Physical Review E* 69(5).
- Howard, J. (1996). "*The Movement of Kinesin Along Microtubules.*" *Annual Review of Physiology* 58(1): 703-729.
- Howard, J. (1997). "*Molecular motors: structural adaptations to cellular functions.*" *Nature* 389(6651): 561-567.
- Howard, J. (2001). *Mechanics of Motor Proteins and the Cytoskeleton*. Sunderland, Sinauer Associates, Inc.
- Humphrey, D., C. Duggan, et al. (2002). "*Active fluidization of polymer networks through molecular motors.*" *Nature* 416(6879): 413-416.
- Huxley, H. E. (1958). "*The Contraction of Muscle.*" *Scientific American* 199(5): 67-&.
- Huxley, H. E. (1963). "*Electron microscopy studies of the structure of natural and synthetic protein filaments from striated muscles.*" *Journal of Molecular Biology* 7: 281-308.

-
- Isambert, H. and A. C. Maggs (1996). "*Dynamics and Rheology of Actin Solutions.*" *Macromolecules* 29(3): 1036-1040.
- Ishikawa, H., R. Bischoff, et al. (1969). "*Formation of Arrowhead Complexes with Heavy Meromyosin in a variety of Cell Types.*" *J. Cell Biol.* 43(2): 312-328.
- Janmey, P. A., J. Peetermans, et al. (1986). "*Structure and Mobility of Actin-Filaments as Measured by Quasi-Elastic Light-Scattering, Viscometry, and Electron-Microscopy.*" *Journal of Biological Chemistry* 261(18): 8357-8362.
- Johnson, K. A. (1985). "*Pathway of the microtubule-dynein ATPase and the structure of dynein: a comparison with actomyosin.*" *Annual Review of Biophysics and Biophysical Chemistry* 14: 161-188.
- Karp, G. (2005). *Cell and Molecular Biology - Concepts and Experiments*. New York, John Wiley & Sons, Inc.
- Käs, J., Strey, H., Sackmann, E. (1994). "*Direct imaging of reptation for semiflexible actin filaments.*" *Nature* 1994: 226-229.
- Keller, M. (2003). *Aktive und passive Aktin-Myosin-Netzwerke*. PhD, Physics Department E22, Technical University Munich, Garching
- Keller, M., J. Schilling, et al. (2001). "*Oscillatory magnetic bead rheometer for complex fluid microrheometry.*" *Review of Scientific Instruments* 72(9): 3626-3634.
- Keller, M., R. Tharmann, et al. (2003). "*Slow filament dynamics and viscoelasticity in entangled and active actin networks.*" *Philosophical Transactions of the Royal Society of London Series a-Mathematical Physical and Engineering Sciences* 361(1805): 699-711.
- Kovac, J. and C. C. Crabb (1986). "*Modified Gaussian Model for Rubber Elasticity .3. Hard-Tube Model.*" *Macromolecules* 19(6): 1744-1747.

- Kroy, K. and E. Frey (1996). "*Force-extension relation and plateau modulus for wormlike chains.*" *Physical Review Letters* 77(2): 306-309.
- Kulp, D. T. and J. Herzfeld (1995). "*Crowding-induced organization of cytoskeletal elements. III. Spontaneous bundling and sorting of self-assembled filaments with different flexibilities.*" *Biophysical Chemistry* 57(1): 93-102.
- Landau, L. D. and E. M. Lifshitz (1986). *Theory of Elasticity*. Pergamon, New York.
- Levine, A. J. and T. C. Lubensky (2000). "*One- and two-particle microrheology.*" *Physical Review Letters* 85(8): 1774-1777.
- Lindner, R. A. and G. B. Ralston (1997). "*Macromolecular crowding: Effects on actin polymerisation.*" *Biophysical Chemistry* 66(1): 57-66.
- Liverpool, T. B., A. C. Maggs, et al. (2001). "*Viscoelasticity of Solutions of Motile Polymers.*" *Physical Review Letters* 86(18): 4171.
- Loïc Le Goff, F. A., and Eric M. Furst (2002). "*Motor-Driven Dynamics in Actin-Myosin Networks.*" *Phys.Rev.Lett.* 88(1): 4.
- Mackintosh, F. C., J. Kas, et al. (1995). "*Elasticity of Semiflexible Biopolymer Networks.*" *Physical Review Letters* 75(24): 4425-4428.
- Mackintosh, F. C., J. Käs, et al. (1995). "*Elasticity of Semiflexible Biopolymer Networks.*" *Physical Review Letters* 75(24): 4425-4428.
- Madden, T. and J. Herzfeld (1993). "*Crowding-induced organization of cytoskeletal elements: I. Spontaneous demixing of cytosolic proteins and model filaments to form filament bundles.*" *Biophys. J.* 65(3): 1147-1154.
- Madden, T. L. and J. Herzfeld (1993). "*Crowding-Induced Organization of Cytoskeletal Elements .1. Spontaneous Demixing of Cytosolic Proteins and Model Filaments to Form Filament Bundles.*" *Biophysical Journal* 65(3): 1147-1154.

- Madden, T. L. and J. Herzfeld (1994). "*Crowding-Induced Organization of Cytoskeletal Elements .2. Dissolution of Spontaneously Formed Filament Bundles by Capping Proteins.*" *Journal of Cell Biology* 126(1): 169-174.
- Margossian, S. S. and S. Lowey (1978). "*Interaction of myosin subfragments with F-actin.*" *Biochemistry* 17(25): 5431 - 5439.
- Marko, J. F. and E. D. Siggia (1995). "*Stretching DNA.*" *Macromolecules* 28(26): 8759-8770.
- Medalia, O., I. Weber, et al. (2002). "*Macromolecular Architecture in Eukaryotic Cells Visualized by Cryoelectron Tomography.*" *Science* 298(5596): 1209-1213.
- Mehta, A. D., J. T. Finer, et al. (1997). "*Detection of single-molecule interactions using correlated thermal diffusion.*" *PNAS* 94(15): 7927-7931.
- Moore, P. B., H. E. Huxley, et al. (1970). "*Three-dimensional reconstruction of F-actin, thin filaments and decorated thin filaments.*" *Journal of Molecular Biology* 50(2): 279-288.
- Morse, D. C. (1998). "*Viscoelasticity of concentrated isotropic solutions of semiflexible polymers. 2. Linear response.*" *Macromolecules* 31(20): 7044-7067.
- Mueller, O., H. E. Gaub, et al. (1991). "*Viscoelastic moduli of sterically and chemically cross-linked actin networks in the dilute to semidilute regime: measurements by oscillating disk rheometer.*" *Macromolecules* 24: 3111-3120.
- Odijk, T. (1993). "*Physics of Tightly Curved Semiflexible Polymer-Chains.*" *Macromolecules* 26(25): 6897-6902.
- Offer, G. and A. Elliott (1978). "*Can a myosin molecule bind to two actin filaments?*" *Nature* 271: 325-329.

- Onck, P. R., T. Koeman, et al. (2005). "*The origin of stiffening in cross-linked semiflexible networks.*" arXiv.org:cond-mat/0502397.
- Pelletier, O., E. Pokidysheva, et al. (2003). "*Structure of actin cross-linked with alpha-actinin: A network of bundles.*" Physical Review Letters 91(14).
- Pink, D. A. (2004). Computer Simulation of Soft Mesoscopic Systems using Dissipative Particle Dynamics in Soft Materials. *Soft Materials: Structure and Dynamics.* A.Marangoni and J.Dutcher, CRC Press: 265.
- Plitzko, J. M. (2005). "*Dreidimensionale Einblicke in die Zellfabriken - Elektronentomographie biologischer Materialien.*" Physik Journal 4(2): 29-35.
- Pollard, T. D., L. Blanchoin, et al. (2000). "*Molecular mechanisms controlling actin filament dynamics in nonmuscle cells.*" Annual Review of Biophysics and Biomolecular Structure 29: 545-576.
- Pollard, T. D. and G. G. Borisy (2003). "*Cellular Motility Driven by Assembly and Disassembly of Actin Filaments.*" Cell 112(4): 453-465.
- Pollard, T. D. and A. G. Weeds (1984). "*The rate constant for ATP hydrolysis by polymerized actin.*" FEBS Lett 170: 94-98.
- Pope, B., M. Way, et al. (1991). "*Two of the three actin-binding domains of gelsolin bind to the same subdomain of actin. Implications of capping and severing mechanisms.*" FEBS Lett 280: 70-74.
- Roth, A. (2004). *Nano-mechanics of biomimetic models of the actin based cytoskeleton - From single molecules to complex composite structures.* Physics Department E22, Technical University Munich, Garching
- Rubinstein, M. and R. H. Colby (2003). *Polymer Physics.* New York, Oxford University Press.

- Ruddies, R. (1992). *Untersuchung der viskoelastischen Eigenschaften von sterisch und chemisch gekoppelten Aktinnetzwerken mittels Elektronenmikroskopie und Mikrorheologie mit extrem kleinen Scherraten*. Diploma thesis, Physics Department E22, Technical University Munich, Garching
- Rudhardt, D., C. Bechinger, et al. (1998). "Direct Measurement of Depletion Potentials in Mixtures of Colloids and Nonionic Polymers." *Physical Review Letters* 81(6): 1330-1333.
- Saitô, N., K. Takahashi, et al. (1967). "The Statistical Mechanical Theory of Stiff Chains." *Journal of the Physical Society of Japan* 22: 219-226.
- Schilling, J. (1999). *Entwicklung einer Echtzeit-Bildverarbeitungssoftware und digitaler Videoaufnahmetechnik zur quantitativen Mikrorheometrie von Aktin-Netzwerken*. Diploma thesis, Physics Department E22, Technical University Munich, Garching
- Schmidt, C. F., M. Barmann, et al. (1989). "Chain Dynamics, Mesh Size, and Diffusive Transport in Networks of Polymerized Actin - a Quasielastic Light-Scattering and Microfluorescence Study." *Macromolecules* 22(9): 3638-3649.
- Sellers, J. R. (1999). *Myosins*. New York, Oxford University Press, Inc.
- Semmrich, C. (2005). *Untersuchung des nichtlinearen Verhaltens von verschlauften und quervernetzten Aktinnetzwerken*. Diploma Thesis, Physics Department E22, Technical University Munich, Garching
- Shillcock, J. C. and R. Lipowsky (2002). "Equilibrium structure and lateral stress distribution of amphiphilic bilayers from dissipative particle dynamics simulations." *The Journal of Chemical Physics* 117(10): 5048-5061.
- Shin, J. H., M. L. Gardel, et al. (2004). "Relating microstructure to rheology of a bundled and cross-linked F-actin network in vitro." *PNAS* 101(26): 9636-9641.

- Spudich, J. A. and S. Watt (1971). "*Regulation of Rabbit Skeletal Muscle Contraction .1. Biochemical Studies of Interaction of Tropomyosin-Troponin Complex with Actin and Proteolytic Fragments of Myosin.*" *Journal of Biological Chemistry* 246(15): 4866-&.
- Steinmetz, M. O., D. Stoffler, et al. (1998). "*Evaluating atomic models of F-actin with an undecagold-tagged phalloidin derivative.*" *Journal of Molecular Biology* 276(1): 1-6.
- Storm, C., J. J. Pastore, et al. (2005). "*Nonlinear elasticity in biological gels.*" *Nature* 435(7039): 191-194.
- Stryer, L. (1991). *Biochemie*. Heidelberg, Spektrum Akademischer Verlag GmbH.
- Suzuki, A., M. Yamazaki, et al. (1989). "*Osmoelastic Coupling in Biological Structures - Formation of Parallel Bundles of Actin-Filaments in a Crystalline-Like Structure Caused by Osmotic-Stress.*" *Biochemistry* 28(15): 6513-6518.
- Suzuki, A., M. Yamazaki, et al. (1996). "*Polymorphism of F-actin assembly .1. A quantitative phase diagram of F-actin.*" *Biochemistry* 35(16): 5238-5244.
- Svitkina, T. M., E. A. Bulanova, et al. (2003). "*Mechanism of filopodia initiation by reorganization of a dendritic network.*" *J. Cell Biol.* 160(3): 409-421.
- Svitkina, T. M., A. B. Verkhovsky, et al. (1997). "*Analysis of the Actin-Myosin II System in Fish Epidermal Keratocytes: Mechanism of Cell Body Translocation.*" *J. Cell Biol.* 139(2): 397-415.
- Taylor, K. A. and R. M. Glaeser (1974). "*Electron diffraction of frozen, hydrated protein crystals.*" *Science* 186: 1036-1037.
- Tempel, M. (1996). *Aktinbindende Proteine als Membran/Zytoskelett-Koppler und als Modulatoren der Viskoelastizität von Aktinnetzwerken*. PhD, Physics Department E22, Technical University Munich, Garching

-
- Tempel, M., G. Isenberg, et al. (1996). "*Temperature-induced sol-gel transition and microgel formation in alpha-actinin cross-linked actin networks: A rheological study.*" *Physical Review E* 54(2): 1802-1810.
- Tharmann, R., M. M. A. E. Claessens, et al. (2006). "*Micro- and Macrorheological Properties of actin networks effectively crosslinked by depletion forces.*" *Biophys. J.*: in print.
- Tyska, M. J., D. E. Dupuis, et al. (1999). "*Two heads of myosin are better than one for generating force and motion.*" *PNAS* 96(8): 4402-4407.
- Uhde, J. (2004). *Mikrorheometrie passiver und aktiver Aktinnetzwerke*. PhD, Physics Department E22, Technische Universität München, Garching
- Uhde, J., M. Keller, et al. (2004). "*Internal motility in stiffening actin-myosin networks.*" *Physical Review Letters* 93(26).
- Uhde, J., N. Ter-Oganessian, et al. (2005). "*Viscoelasticity of entangled actin networks studied by long-pulse magnetic bead microrheometry.*" *Physical Review E (Statistical, Nonlinear, and Soft Matter Physics)* 72(6): 061916.
- Vale, R. D. and R. A. Milligan (2000). "*The Way Things Move: Looking Under the Hood of Molecular Motor Proteins.*" *Science* 288(5463): 88-95.
- Valentine, M. T., Z. E. Perlman, et al. (2004). "*Colloid surface chemistry critically affects multiple particle tracking measurements of biomaterials.*" *Biophysical Journal* 86(6): 4004-4014.
- Voet, D. and J. G. Voet (1995). *Biochemistry*. New York, John Wiley & Sons.
- Wagner, B. (2003). *Rheologische Charakterisierung der Struktur-Funktions-Beziehung von Aktinvernetzerproteinen*. Diploma thesis, Physics Department E22, Technical University Munich, Garching

Wagner, B., R. Tharmann, et al. (2005). "*Cytoskeletal polymer networks: molecular structure of crosslinkers determine macroscopic properties.*" Pro.Natl.Acad.Sci. USA submitted.

Wegner, A. (1976). "*Head to tail polymerization of actin.*" Journal of Molecular Biology 108(1): 139-150.

Wells, A. L., A. W. Lin, et al. (1999). "*Myosin VI is an actin-based motor that moves backwards.*" Nature 401(6752): 505-508.

Wendt, T., D. Taylor, et al. (1999). "*Visualization of Head-Head Interactions in the Inhibited State of Smooth Muscle Myosin.*" J. Cell Biol. 147(7): 1385-1390.

Wendt, T., D. Taylor, et al. (2001). "*Three-dimensional image reconstruction of dephosphorylated smooth muscle heavy meromyosin reveals asymmetry in the interaction between myosin heads and placement of subfragment 2.*" PNAS 98(8): 4361-4366.

Wilhelm, J. and E. Frey (2003). "*Elasticity of stiff polymer networks.*" Physical Review Letters 91(10).

Wong, I. Y., M. L. Gardel, et al. (2004). "*Anomalous diffusion probes microstructure dynamics of entangled F-actin networks.*" Physical Review Letters 92(17).

Xu, J., Y. Tseng, et al. (2000). "*Strain Hardening of Actin Filament Networks. Regulation by the dynamic cross-linking protein alpha -actinin.*" J. Biol. Chem. 275(46): 35886-35892.

Ziemann, F. (1997). *Untersuchung der lokalen viskoelastischen Eigenschaften von Zellen und Zellmodellen mit einem Magnetkugel-Mikrorheometer.* PhD, Physics Department E22, Technical University Munich, Garching

Zilman, A. G. and S. A. Safran (2003). "*Role of cross-links in bundle formation, phase separation and gelation of long filaments.*" Europhysics Letters 63(1): 139-145.

E. Acknowledgments

Gracie moltissime,

an alle E22-er, die mich in meiner Zeit am Lehrstuhl begleitet haben.

Mein ganz spezieller Dank gilt ...

... **Prof. Andreas Bausch**, dafür dass er mir die Möglichkeit gegeben hat unter seiner Betreuung am Lehrstuhl E22 diese Promotion zu schreiben und zu beenden. Die letzten vier Jahre waren für mich ein sehr großer Entwicklungs-Prozess bei dem ich viel von ihm lernen konnte und auch immer die nötige Unterstützung bekam. Danke!

... **Prof. Sackmann**, dafür dass er mir die Möglichkeit gegeben hat an seinem Lehrstuhl diese Promotion zu starten. Seine Loyalität, sein Wissen und seine Kreativität werden mir immer als Vorbild dienen.

... **Mireille**, ihr Beitritt zur wachsenden Gruppe von Prof. Bausch war entscheidend. Hier möchte ich mich herzlich bedanken für den unermüdlichen Einsatz im Korrekturlesen meiner Arbeit. Ohne ihre Hilfe wäre es einerseits nicht möglich gewesen die Arbeit auf Englisch zu schreiben und andererseits wären viele Fragen offen geblieben, von denen wir letzten Endes durch lange fruchtbare Diskussionen die meisten lösen konnten. Danke!

... **Bernd**, als einen Freund, einen kompetenten Diskussionspartner und nicht zuletzt auch für das Korrekturlesen meiner Arbeit. Es hat mir viel Spaß gemacht mit dir zu arbeiten und auch am Wochenende einen „Jamaican Bunny“ zu leeren.

... **Frau Kirpal**, die immer an mich geglaubt hat und mir eine große Hilfe war in allen bio-chemischen Fragen. Ihre Präzision in der Arbeit werde ich immer versuchen nachzuahmen.

...meinen beiden Freunde **Simon** und **Stephan**, mit denen mich eine enge Freundschaft verbindet. Wir haben gemeinsam auf das Hauptdiplom gelernt, gemeinsam sind wir durch das Jahr der Diplomarbeit gegangen und gemeinsam beenden wir auch unsere Promotion. Zwar jeder in einer anderen Fachrichtung und an einer anderen Universität, doch wir halten stetig den Kontakt.

... **Flo, Stephan und Thomas**, für die konstruktive Kritik und das Korrektur lesen meiner Arbeit. Es hat mir sehr weitergeholfen. Danke!

... meinen Werkstudenten **Sebastian, Moritz, Andrea und Christoph** für die Zusammenarbeit, die mir immer Spaß gemacht hat und für die Ergebnisse die wir zusammen erreicht haben. Danke!

... **Monika, Karin und Claudia**, dafür dass sie mir immer mit Rat und Tat zur Seite standen. Monika möchte ich besonders danken für die exzellenten Aktin Präparationen. Monika, du machst das beste Aktin!

... **Rudi**, für alle Maanfertigungen und die Hilfe bei Konstruktionen.

... **Claudine** und **Katerina**, für die Hilfe in bürokratischen Angelegenheiten.

... **Jörg Uhde**, **Manfred** und **Jörg Schilling** für die Hilfe bei Fragen im Kontext mit OpenBox, Mikroskopie, Magnetic Tweezer und vieles Andere.

... **Felix**, **Jörg Schilling**, **Johann** und **Michael** für die Zusammenarbeit als Netzwerkadministratoren im Kampf gegen Viren, Drucker Probleme und manchmal auch gegen unerklärliche Phänomene.

... **Nök**, **Oli**, **Flo** und **Murat (alias Uwe)** als meine engsten Freunde im Lehrstuhl mit denen ich viele unvergessliche Momente erleben durfte. PPP

...meinem außeruniversitären Rückrad:

...meinen Freunden **Julian**, **Thomas** und **Peter**, dafür dass sie immer für mich da sind auch in schwierigen Situationen und dafür, dass sie das Verständnis aufbringen wenn sich Wege ändern.

...meiner **Frau Katrin**, die mir während meiner Promotion zwei gesunde Kinder schenkte mich ehelichte und mit mir zusammen die Zukunft aufbaut. Danke dafür, dass du mir in so vielen Situationen immer Verständnis entgegengebracht hast. Danke!

...meinen **Eltern**, ohne deren Hilfe ich es nicht bis hierher geschafft hätte. Danke für eure beispiellose Art für mich da zu sein.

F. Publications

R. Tharmann, M.M.A.E. Claessens, A.R. Bausch: “Myosin and heavy meromyosin act as active and passive cross-linkers: A rheology study” in preparation.

David Pink, **Rainer Tharmann**, Ryan Hunter, Gillian Ryan, Bonnie Quinn, Laura Filion, Andreas Bausch and Terry Beveridge: „Rheology of Biofilms of Pseudomonas Aeruginosa PAO1. Experiment and Theory” in preparation.

B. Wagner, **R. Tharmann**, I. Haase, M. Fischer, and A.R. Bausch: “Cytoskeletal polymer networks: molecular structure of crosslinkers determine macroscopic properties”, Proceedings of the National Academy of Sciences (2005), under review

R. Tharmann, M.M.A.E. Claessens, A.R. Bausch: “Micro- and Macrorheological Properties of actin networks effectively crosslinked by depletion forces”, Biophysical Journal (2006); 90: 2622-2627.

M.M.A.E. Claessens, **R. Tharmann**, K. Kroy, A.R. Bausch: “Microstructure and viscoelasticity of confined semiflexible polymer networks“, Nature Physics (2006) Vol. 2, 186-189

S. Keller, **R. Tharmann**, A.R. Bausch, J.O. Rädler: “Velocity profiles of Non-Newtonian Liquids measured by Dual-Focus Fluorescence Correlation Spectroscopy“, submitted to European Physical Journal (2005)

M. Keller, **R. Tharmann**, M. A. Dichtl, et al.: “Slow filament dynamics and Viscoelasticity in entangled and active actin networks“, Philosophical Transactions of the Royal Society of London Series a-Mathematical Physical and Engineering Sciences 361, 699 (2003).

G. Curriculum Vitae

Rainer Tharmann, Hirtgrasstr.11, 85737 Ismaning

Personal Data

Date of birth: 24.04.1974 in Munich

Marital status: married

Kids: 2

Professional activity

03/2002 – today PhD thesis at the Lehrstuhl für Biophysik E22, Technische Universität München, Germany Topic: Polymers
Title: “Mechanical Properties of complex Cytoskeleton Networks“
Senior team responsibility of 2 diploma students, 3 working students and supervision of interns; network management of the chair

University education

10/1995 – 02/2002 Study of physics at the Technischen Universität München, Germany
Diploma thesis at the Lehrstuhl für Physik E10, Technische Universität München, Germany
Title: “Entwicklung eines kontinuierlichen, kontaktlosen Verfahrens zur Charakterisierung langer HTSL-Bandleiter durch Hall-Sondenmessung“
Degree: Dipl.-Phys. Univ.
Specialty: Low-Temperature-Physics and Superconductivity, Surface Physics
Specialized courses: Cryogenics, laser technique, semiconductor sensors

School Education

1.07.1994 Secondary school “Städtisches Luise Gymnasium”, Germany, Degree: general matriculation standard “Allgemeine Hochschulreife“